Heat Pipes for the Thermal Management of High Frequency Transformers in the Navy integrated Power Electronics Building Block

by

David Hernandez

B.S. Mechanical Engineering, MIT, 2023

Submitted to the Department of Mechanical Engineering
in partial fulfillment of the requirements for the degree of

MASTER OF SCIENCE IN MECHANICAL ENGINEERING

at the

MASSACHUSETTS INSTITUTE OF TECHNOLOGY

September 2024

Authored by:	David Hernandez Department of Mechanical Engineering August 9, 2024
Certified by:	Julie Chalfant Research Scientist, Thesis Supervisor
Certified by:	Michael Triantafyllou Professor in Ocean Science and Engineering, Thesis Supervisor
Accepted by:	Nicolas Hadjiconstantinou Professor of Mechanical Engineering Graduate Officer, Department of Mechanical Engineering

Heat Pipes for the Thermal Management of High Frequency Transformers in the Navy integrated Power Electronics Building Block

by

David Hernandez

Submitted to the Department of Mechanical Engineering
on August 9, 2024 in partial fulfillment of the requirements for the degree of

MASTER OF SCIENCE IN MECHANICAL ENGINEERING

ABSTRACT

The development of the integrated Power Electronics Building Block (iPEBB) is key to the full electrification of future United States Navy ships. The creation of this modular, universal power converter takes full advantage of modern electronics; however, the high heat generation of these components, 9.6 kW from the MOSFET switches and 624 W from the transformer, makes thermal management crucial to their successful implementation. As a result of additional requirements, indirect liquid cooling using a detached cold plate is being studied; however, preliminary analysis revealed concerns regarding the hot spot temperatures of the transformer using this approach. This thesis explored the feasibility of using heat pipes to supplement the cooling provided by the cold plate to maintain iPEBB transformer core and coil temperatures below 100°C and 155°C respectively. First, experiments and analytical solutions were used to provide accurate estimates for the thermal conductivity values of the 3F36 ferrite and litz wire in the transformer. Then, a standalone thermal model of the transformer was built in StarCCM+ and used to test various cooling solutions, including forced airflow and heat pipe configurations. The proposed design utilized 16 copper-water heat pipes configured to provide alternative paths of heat flow for the regions of the transformer furthest from the cold plate. Shapal HiM Soft Machinable AlN ceramic was utilized to provide high voltage insulation, and electromagnetic simulations were used to estimate the induced losses in the heat pipes as a result of high frequency coil operations. Using a half-iPEBB thermal model, the final configuration, coupled with the cold plate cooled by 22°C deionized water at a flow rate of 0.37 kg/s, achieved a core maximum temperature of 99.7°C, coil maximum of 93.2°C, and MOSFET maximum of 144.6°C, all within their respective limits, while only adding a net weight of 0.29 kg to the iPEBB. The thermal results of this study showcase the effectiveness of heat pipes in the iPEBB and invite further analysis and experimentation to validate the electromagnetic implications of the concept. These results also contribute to the general ongoing study of heat pipe usage near high-frequency electronics.

Thesis supervisor: Julie Chalfant
Title: Research Scientist

Thesis supervisor: Michael Triantafyllou
Title: Professor in Ocean Science and Engineering

Acknowledgments

I would like to express my deepest gratitude to my thesis advisors, Dr. Julie Chalfant and Professor Michael Triantafyllou. Their feedback throughout this project was pivotal to its progress, and their guidance helped me in moments when the path forward seemed uncertain. I would like to thank Dr. Chalfant in particular for the opportunities she has provided me, from overseeing my first UROP with Sea Grant during my undergraduate sophomore year to my bachelor's and now master's theses.

I would also like to thank Dr. Chathan Cooke for his generosity in lending his technical expertise for the electromagnetic analysis within this project.

To my parents, grandparents, sister and loved ones, I would like to thank you all for your sustained love and support over the past 5 years. I know that many sacrifices have been made for me to be in this position, and for that I am forever grateful. Como dice mi abuela, ¡he llegado al último escalon!

Lastly, I would like to thank the financial sponsors of this project. This material is based upon research supported by the U.S. Office of Naval Research (ONR) under award number ONR N00014-21-1-2124 Electric Ship Research and Development Consortium; and by the National Oceanic and Atmospheric Administration (NOAA) under Grant Number NA22OAR4170126-MIT Sea Grant College Program.

Contents

List of Figures

List of Tables

Chapter 1

Introduction

The demand for improved performance and enhanced capabilities onboard naval vessels has increased the complexity of the electrical systems required to meet these goals. As a result, areas such as power conversion and distribution are being redesigned in order to modernize operations and prepare for the demands of future technology. With funding from the United States Office of Naval Research (ONR), the Electric Ship Research and Development Consortium (ESRDC) works on developing the technical concepts that will enable the next generation of electrified naval ships.

A current focus of the ESRDC's work is in the development of the Power Electronic Power Distribution System (PEPDS) which is the framework for a new electrical system capable of simultaneously delivering both AC and DC power signals to every connected component throughout a ship [1]. The embodiment of this concept is the Navy integrated Power and Energy Corridor (NiPEC), which aims to meet this delivery goal while also grouping the primary electrical distribution and conversion equipment into a compact and modular physical footprint [1].

The modularity of the NiPEC is provided through the usage of a base component known as the integrated Power Electronics Building Block (iPEBB), which is designed to be a self-contained and replaceable power conversion unit [2]. The concept of the NiPEC involves the utilization of multiple iPEBBs in any given subsection, utilizing the units either in series or parallel to deliver the required voltage and current levels to connected components. Such flexibility allows for the NiPEC corridor to easily scale with the power demands of different ship classes, as well as streamline the manufacturing and integration processes. On the operational level, the interconnectedness of the NiPEC corridor through the iPEBB units provides redundancy as any section of iPEBBs is capable of serving as a backup to any other in the event of a unit failure. In addition, the iPEBB is also designed to be lightweight and operate on a "plug-and-play" approach, allowing for quick replacement for repairs and maintenance.

In order to meet the power conversion and density requirements, the iPEBB must be adequately cooled to ensure the full performance of its internal components. The final 250 kW iPEBB is in the process of being developed; however, currently available is the design of a 100 kW version which sees dominant heat generation through 96 MOSFET switches and a 400kHz transformer, which, under worst case conditions, can generate roughly 9.6 kW and 624 W of waste heat respectively [2] [3]. The task of thermal management is made more

difficult when considering the design limitations specific to the iPEBB. The requirement of being easy to carry limits the weight of a unit to 35 lbs and similarly affects its total volume [4]. Furthermore, the desire for quick attachment and detachment process prohibits the presence of fluid within the iPEBB due to the complexities associated with drainage, eliminating the possibility of directly liquid-cooling the internal components.

With this design challenge in mind, a concept that is currently being investigated is that of indirect liquid cooling through a rack-mounted cold plate. The approach would rely on forced convection via the passing fluid to create a chilled heat sink that would be in contact with both the top and bottom outer surfaces of the iPEBB. By having the primary cooling hardware detached from the iPEBB unit itself, this addresses both the size and ease of removal limitations. Preliminary thermal analysis of this solution on an iPEBB model found that the cold plate was effective at lowering component temperatures; however, also concluded that the transformer, although lower in total heat output, experiences hot spots exceeding specification in regions furthest from the cold plate [5]. For indirect liquid cooling to become a feasible solution, additional hardware must be incorporated to maintain temperatures in these harder to reach regions of the transformer.

The scope of this thesis is to explore the usage of copper-walled heat pipes in conjunction with indirect liquid cooling to provide an acceptable thermal management solution for the iPEBB transformer. The development of both the thermal model as well as a preliminary electromagnetic model will be completed in Siemens StarCCM+. Proposed solutions will be analyzed based on their ability to regulate transformer temperatures, with additional consideration towards potential electromagnetic impacts associated with the high-frequency, medium-voltage operations of the transformer. Experimental work to validate material properties will also be completed in parallel in order to improve the accuracy of the simulation models. The goal is to provide a detailed overview of the heat pipe configuration required to pull heat from the transformer core and coil to the common substrate, which will be cooled via indirect liquid cooling. The findings will serve as a baseline for future design iterations and provide a working cooling solution for usage in planned experimental testing of the iPEBB.

This thesis consists of seven chapters with a mixture of framing, analysis, and experimentation. Chapter 2 provides an overview of the current iPEBB design and a review of transformer modeling and cooling methods commonly seen in literature. The following two chapters discuss experiments conducted to determine thermal properties for input in the simulation models. Chapter 3 outlines the experimental measuring of the thermal conductivity of the ferrite core, while Chapter 4 discusses the derivation of the radial thermal conductivity of the litz wire coils through both analytical and experimental approaches. Chapter 5 contains the bulk of the design work as a heat-pipe based solution is developed through component-level thermal and electromagnetic simulations. Lastly, Chapter 6 will integrate the proposed solution in a half-iPEBB thermal simulation.

Chapter 2

Background

2.1 iPEBB

Years of development have resulted in the current iteration of the iPEBB v3 as shown in Figure 2.1. This version is designed to occupy an external footprint of 550 mm x 300 mm x 100 mm, and as stated earlier must also have a total carried weight of under 35 lbs [6]. These two requirements are derived from a primary design goal of making the iPEBB easy to handle for a single person, and a result cannot be loosened. Current estimates for the iPEBB v3 have a unit weight of 33 lbs; however, it is key to note that this weight does not include any in-unit cooling hardware, leaving a maximum of 2 lbs for any required additional components [4].

Within the iPEBB are two identical halves consisting of electronic components mounted onto a multi-layer common substrate. The components driving the heat losses of the unit are the MOSFET switches, also referred to as SiC Bridges, and the high frequency transformer, with a combined worst-case heat load of approximately 11 kW for the entire unit. Figure 2.2 shows the internals of the iPEBB with these heat-generating sections highlighted.

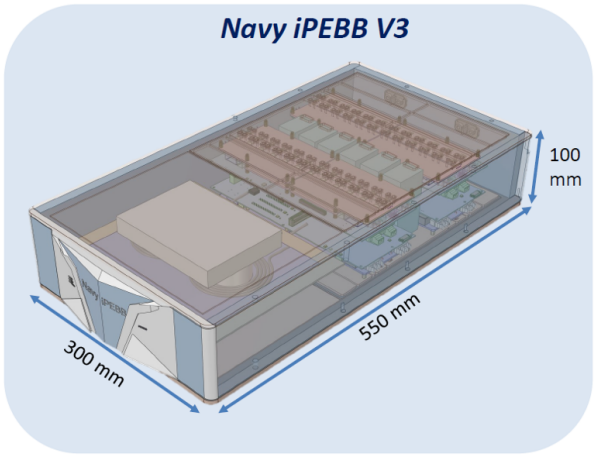

Figure 2.1: Outside isometric view of the iPEBB v3 from the Virginia Tech Center for Power Electronics Systems (CPES) [6].

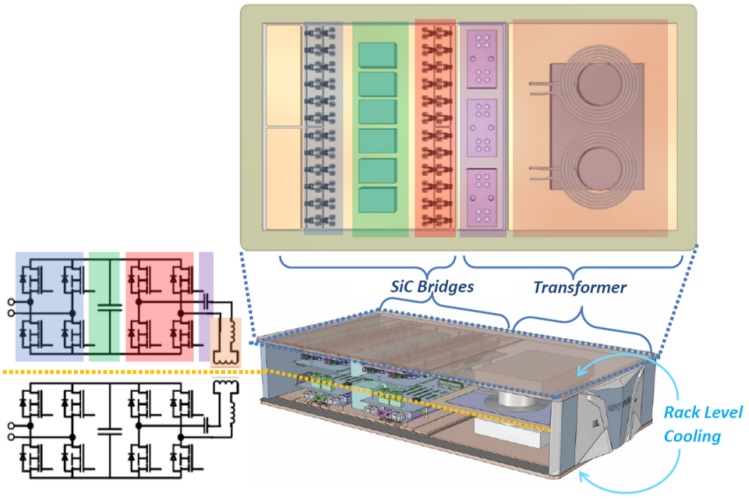

Figure 2.2: iPEBB half-substrate with heat-generating components labeled [6].

2.1.1 MOSFETs

Contributing the highest percentage of heat generation within the iPEBB are the 96 SiC MOSFET switches located on the inner-most surface of the common substrate. The MOSFETs are split between the two half-substrates and are arranged in rows with 0.25 in of spacing between each switch. The MOSFETs used can be modeled as rectangular bodies with a substrate-touching profile of 4.36 mm x 7.26 mm and thickness of 0.18 mm. The location and organization of the SiC MOSFET switches can be seen in Figure 2.2.

Each MOSFET switch is estimated to produce 100 W of waste heat under worst-case conditions, which, when applied to all 96 switches simultaneously, generates up to 9.6 kW of heat that must be conducted through the common substrate [6]. The cooling solution must maintain these switches below their manufacturer-specified temperature limit of 180°C. Due to the importance of this component, however, a margin of 30°C will be applied, giving a target maximum temperature limit of 150 °C.

The large amount of heat generated and relatively small surface area of each MOSFET create the thermal issue of having high heat fluxes at the points of attachment. In addition, the close proximity of neighboring switches can lead to heat overlap and further increase hot spot temperatures. One goal of this thesis will be to validate the heat spreading provided by the current common substrate and cold plate solution.

2.1.2 Transformer

The other critical source of heat generation within the iPEBB is the high frequency transformer. The current iteration of transformer is a 100 kW variant, and uses a 3F36 ferrite core with a half footprint of 110 mm x 55 mm x 65mm. The two core halves are separated by a 3 mm thick mica sheet. For the coils, an overall 8 AWG litz wire with 5x5x3/56/44 strand configuration and an outer polyurethane nylon jacket to 0.211" OD is used. A visual representation of the transformer geometry and assembly is shown in Figure 2.3 [3].

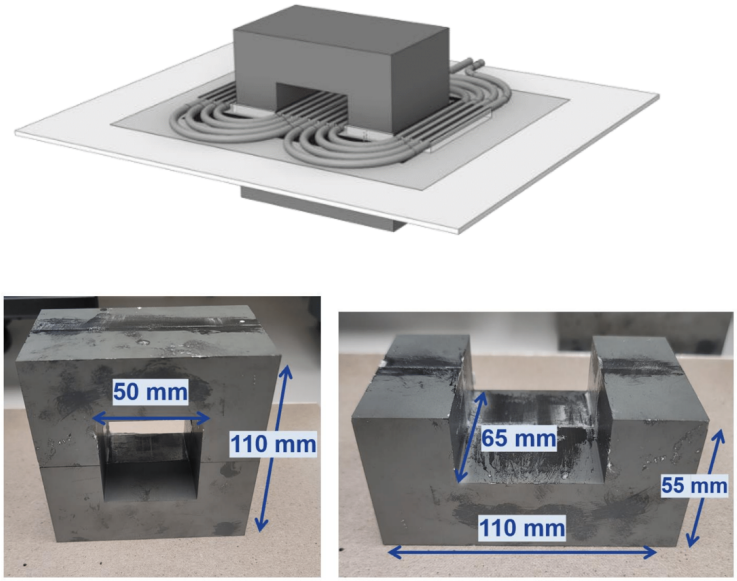

Figure 2.3: Current iPEBB transformer as designed by the Virginia Tech Center for Power Electronics Systems (CPES) [3] [4].

Experimental testing through open-circuit and short-circuit tests of this design resulted in an observed 400 W - 480 W of core heat losses and 144 W of coil heat losses respectively [4]. For the core, the maximum temperature limit going forward will be 100°C based on the exponentially decreasing efficiency of the ferrite material over this value [7]. The coils are bound by the melting temperature of the outer polyurethane nylon jacket, resulting in an upper temperature limit of 155°C [8].

As identified in a previous thermal analysis of the iPEBB, the transformer poses a significant challenge due to the previously mentioned limitations in cooling approaches and the geometry of the current design [5]. The transformer currently lacks sufficient access to the heat sink located on both the top and bottom faces of the iPEBB unit. As a result, this thesis will primarily focus on developing a supplementary cooling solution for the transformer and validating all proposed thermal management hardware through iPEBB-scale simulations.

2.1.3 Common Substrate

The common substrate forms the base of the iPEBB both functionally and structurally, acting as the mounting interface for all components while providing mechanical integrity for the unit. The multi-layer build consists of alternating sheets of copper and an organic bonded copper substrate (OBDC), a design which balances both voltage insulation and heat spreading from the MOSFETs and transformer [4]. A breakdown of the common substrate's design and construction can be seen in Figure 2.4. With the cold plate in contact with the outer-most layer of copper, all heat generated during iPEBB usage will flow through the multi-layer substrate to the rack-mounted cold plates.

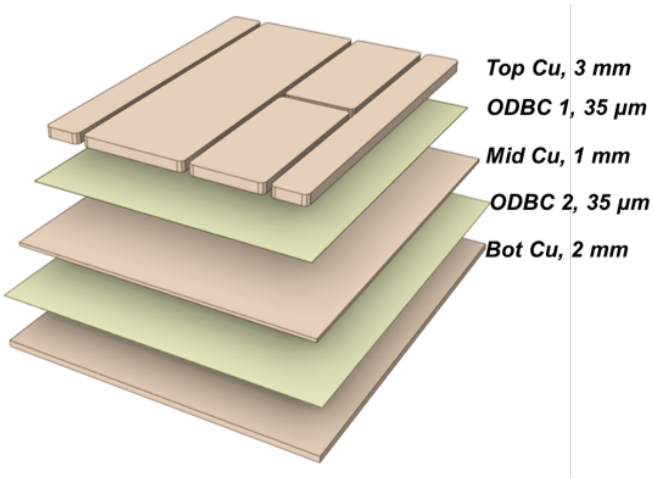

Figure 2.4: Layer composition of the iPEBB common substrate [4].

2.1.4 Cold Plate

A previously designed aluminum cold plate will be used to provide the iPEBB's heat sink for this study's investigation of indirect liquid cooling. The cold plate, shown in Figure 2.5, utilizes a flow of deionized water in a cross-flow configuration to maintain the heat sink at a cool temperature [9]. A cooling loop to an external heat exchanger is dedicated to delivering this cooled water to the iPEBBs, with an expected cold plate inlet water temperature of 22°C and flow rate of 0.370 kg/s at maximum load [10]. In order to minimize the contact thermal resistance between the iPEBB and this cold plate, a thermal interface material known as PGS is placed and compressed to fill any surface imperfections [11].

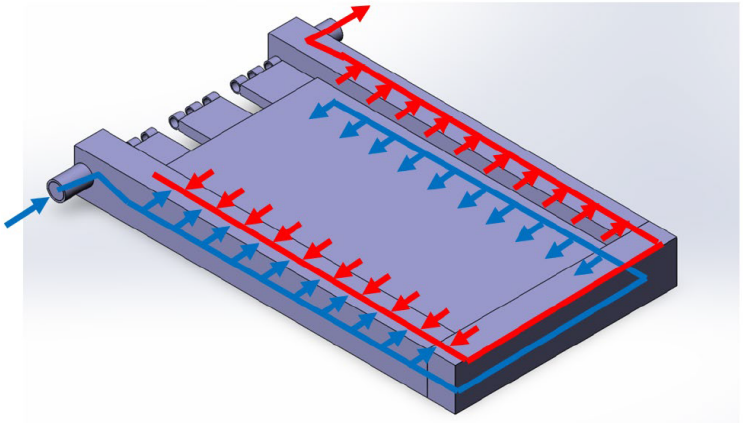

Figure 2.5: Cold plate with cross-flow configuration designed for the iPEBB. [9].

Having the cold plate separate from the iPEBB unit provides various benefits. By having the cooling solution rack-mounted, this allows for the superior cooling performance of circulating water while ensuring that the iPEBB unit itself remains sealed and free of fluid. Additionally, the weight and volume associated with the cold plate is not fixed to the iPEBB, aiding with the mobility and handling requirements.

2.2 Transformer Cooling Literature Review

The cooling of a transformer is crucial to its operation as overheating components can lead to drops in performance and cause damage. Over the decades, cooling methods of varying effectiveness and effort have been developed to meet the rising capabilities of newer builds. Transformers fall into one of two categories based on their cooling methods: the "dry" type and the "wet" type.

The term "dry" refers to transformers that are not directly cooled by a liquid medium, and typically involves air cooling both the core and coils. Some low voltage transformers are capable of being cooled through pure natural convection, and rely on the buoyancy-driven circulation around the components to maintain acceptable temperatures [12]. For higher voltages and frequencies, however, greater heat transfer coefficients are needed to pull the larger waste heat generated. A common solution is to use forced-air cooling via fans to increase the heat transfer to the air, as shown by Chen et al. in the design of a 200 kHz, medium voltage transformer [13]. An key feature to note in this design, which can be seen in Figure 2.6, is the "potting" of the coils in epoxy, which is a consequence of the electrical insulation requirements of transformers at these higher voltage levels. The authors note that epoxy is typically selected for this purpose due to its compromise between electrical insulation and thermal conductivity, as the material becomes a source of thermal resistance between the heat generating coils and air-cooled surface.

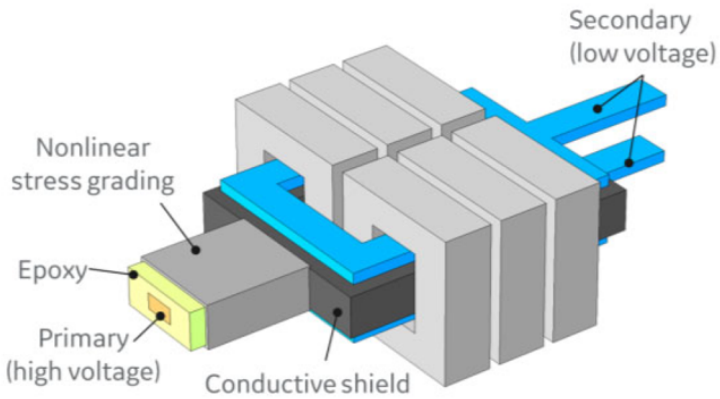

Figure 2.6: Overview of a 200 kHz, medium voltage air-cooled transformer with potted coils, as designed by Chen et al. [13].

Another example of a dry-type transformer can be seen in the design of a high frequency, medium voltage transformer by Wang et al. [14]. In this design, the authors explored potting the entire transformer in epoxy and directly attaching to an air-cooled heat sink on one surface, as shown in Figure 2.7. Rather than cool the transformer directly, air is passed through a finned heat sink with all heat having to pass through the epoxy medium. The smaller size of this transformer made potting the entire assembly feasible, compared to only potting the coils as is done in other designs. Through both simulation and experimental results, this study was able to demonstrate the feasibility of cooling a transformer core and coils through an indirect heat sink.

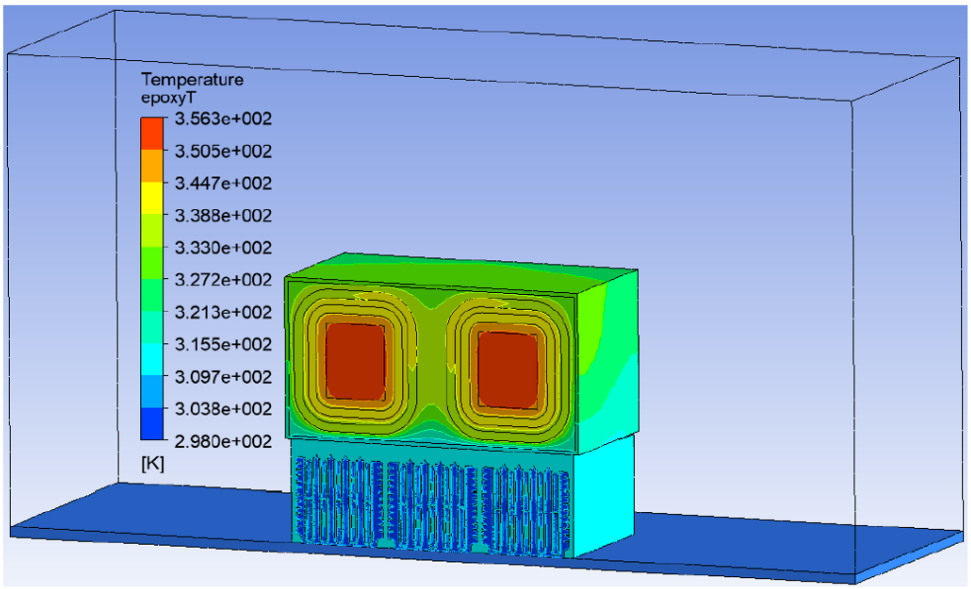

Figure 2.7: Temperature predictions for a high frequency, medium voltage potted transformer with an air-cooled heat sink, as modeled by Wang et al. [14].

In a recent development of a dry-type transformer, Sharfeldden et al. showcase the direct air-cooling of a medium voltage transformer with exposed coils [15]. This design saw the foregoing of potted coils and instead relied on direct forced-air cooling over the exposed winding surfaces. According to the authors, the weight savings granted by omitting the layer of epoxy was necessary to meet the low mass requirement of the system. Focusing on the cooling of the coils, the paper was able to confirm through experiment that a 50 CFM fan was capable of maintaining coil temperatures under 63°C during 175 A, 286 kHz operations.

In a wet-type transformer, the coils and core are submerged in an oil solution which transfers heat from the components to adjacent heat sinks. Similar to the dry-type variants, oil-cooled transformers can utilize both the natural convection of the coolant fluid as well as forced flow over the components to draw heat away from the core and coils [12]. The use of oil, although effective at cooling, results in a significantly higher overall system mass compared to air-cooled solutions. As a result, larger transformers with weight constraints tend to favor dry cooling approaches.

2.3 Litz Wire Thermal Modeling Literature Review

Litz wire has been a crucial element in the development of high-frequency and high-efficiency power electronics since its introduction in the early 20th century [16]. The bundling and interweaving of individual strands has proven effective at reducing the resistance associated with skin and proximity effects at high frequency operations. From a thermal modeling perspective, however, this weaving multi-member construction can be difficult to model as the numerous contact points between individual strands results in a large, complex network with countless possible paths for heat to flow across the wire. In addition, this leads to the

periodic formation of air gaps that, even if filled with a material such as epoxy, reduces the overall thermal conductivity of the wire.

Several approaches have aimed at developing an analytical expression for the effective thermal conductivity of litz wire with the goal of improving confidence in its modeling in future applications. In one example, Liu et al. used the Gasar porous metal materials model to simplify the cross section of a circular litz wire in order to develop an effective thermal resistance across an arbitrary section [17]. As shown in Figure 2.8, the authors converted the circular profile to rectangular dimensions of equivalent area, allowing for the derivation of a thermal resistance network that captures the heat flux across the copper, enamel, and gaps present in litz wire. The result of this approach was the derivation of an effective thermal conductivity that, when substituted into a solid body with the same outer geometry, could replicate the thermal resistance and temperature profile of litz wire.

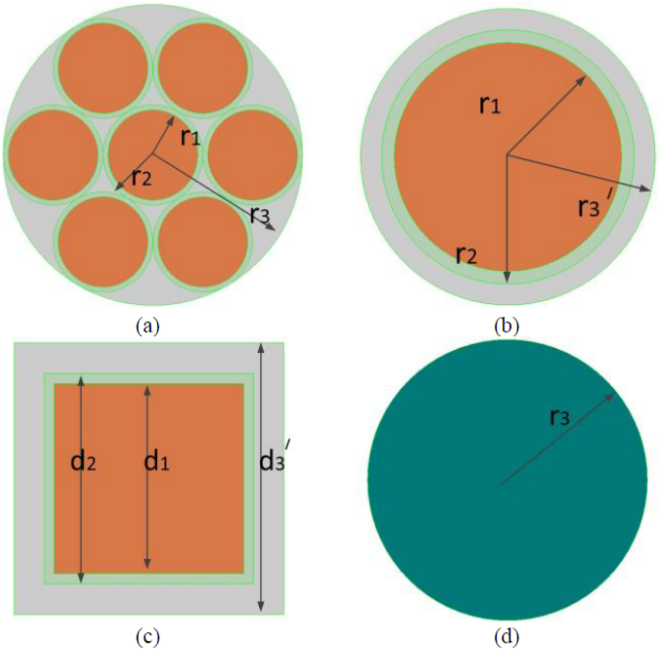

Figure 2.8: Breakdown of a typical litz cross section to an equivalent cell model based on the Gasar porous metal materials model as developed by Liu et al. [17].

Approaching the challenge from a different perspective, Yi et al. focused on creating an analytical model by capturing the transposition effect between litz wire bundles [18]. This paper developed a thermal resistance network for a rectangular sample by considering both axial and radial interactions on individual strands. Using the known strand orientation and contact angles, the model proved capable of predicting the temperature profile along a sample of litz to agreement with experimental and simulation values. As mentioned, however, this modeling approach relies on knowledge of the winding construction that may not be widely known or available depending on the manufacturer.

In a different study also considering the thermal modeling of litz wire through the transposition effect, Dong and Fu explored the impact of varying strand fill rate, which is the ratio of cross-sectional area occupied by litz strand [19]. The authors found that increasing the fill rate, and thus reducing the amount of gaps in the wire, resulted in a major change

in effective thermal conductivity across the sample, with the value for one litz sample scaling by 3 times across the possible filling rates. A graph showing this trend can be seen in Figure 2.9. For applications with large heat dissipation through the coils, this difference in radial thermal conductivity can have significant impacts on the temperatures seen by the litz wire.

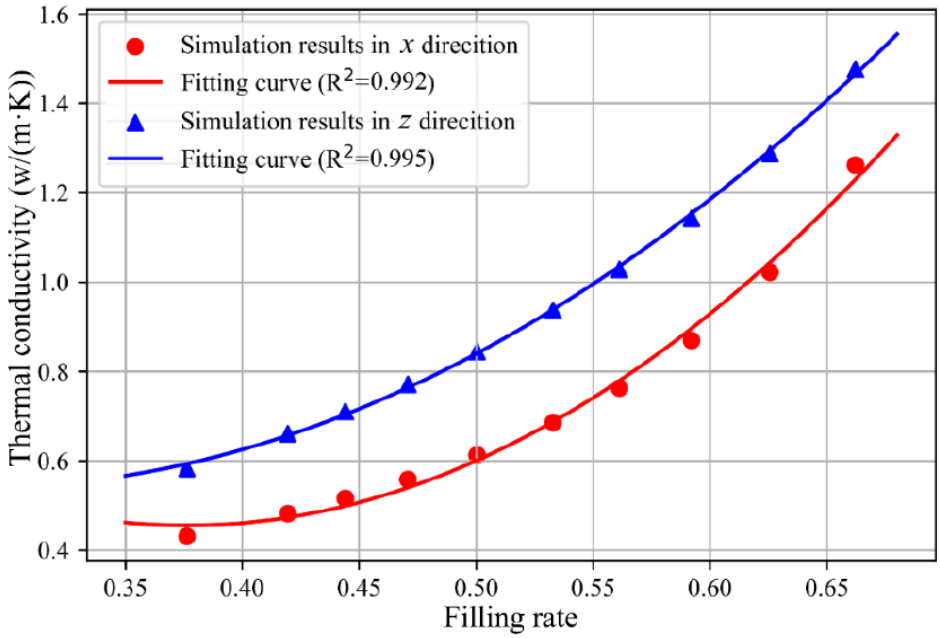

Figure 2.9: Impact of litz filling rate on its effective thermal conductivity for a rectangular cross-section sample of wire as found by Dong and Fu. [19].

The large variations in construction between different litz types can stretch the application of pre-established modeling techniques. A common solution that has been observed in literature, including in the previously mentioned studies, is to experimentally measure this value across a litz sample of interest. Liu et al. and Yi et al., for example, used similar test setups that involved applying a known heat flux across a sample of litz wire in order to calculate the effective thermal conductivity based on the measured temperature gradient [17] [18]. An example setup from Liu et al. can be seen in Figure 2.10.

Due to the simplifications that must be made in analytical modeling and the uncertainty associated with any experiment, there is always an inherent error with the effective thermal conductivity of litz wire. One approach to reduce the risk associated with this uncertainty has been to include a sensitivity study on the used thermal conductivity value. In one example, Woodworth et al. utilized CFD software to perform a sweep on their measured litz thermal properties, testing the robustness of their proposed cooling solution to manage coil temperatures [20]. By doing this, the authors were able to provide confidence to their solution even in edge cases that exceeded the expected error of their initial measurement.

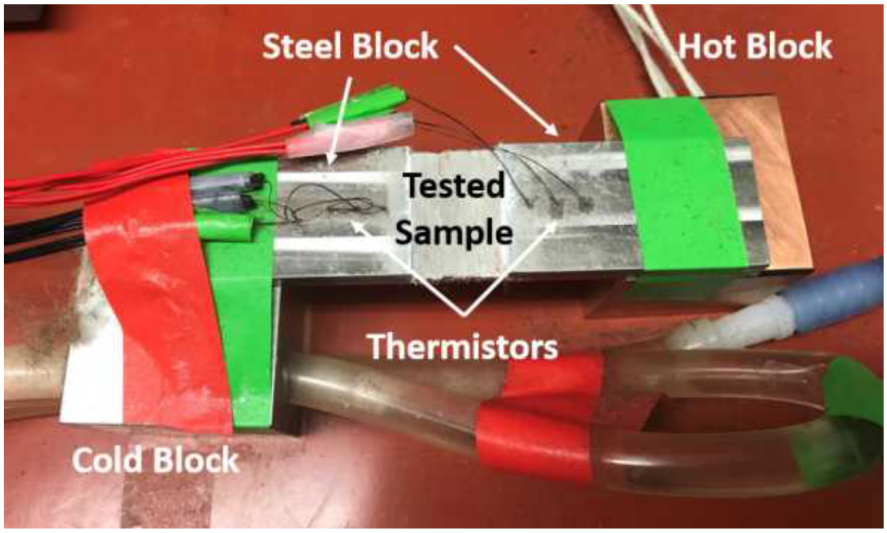

Figure 2.10: Example setup of a litz wire thermal conductivity experiment as performed by Yi et al. [18].

2.4 Heat Pipe Background

Heat pipes are devices which offer strong heat transfer capabilities through the phase-change of its internal working fluid. As shown in the representative diagram in Figure 2.11, these components consist of sealed tubes which circulate the fluid between the liquid and vapor phases. With the heat source applied to one end, the local fluid vaporizes and travels through the pipe to the cooler end of the body, where it then condenses back into fluid and releases the carried latent heat into the heat sink [21]. The design of the wall-lining wick material enables the capillary action that circulates this cooled liquid back to the heat source, finishing the closed-loop process.

The usage of natural circulation in both the liquid and vapor regimes makes heat pipes a fully passive component. This gives them the advantage of being reliable and ensures long lifespans, as they do not use any moving parts and require zero maintenance. The effective heat moving capabilities coupled with this reliability is a main factor behind their extensive usage in aerospace applications, where systems are expected to endure extreme conditions for years and decades without fault [22]. In addition, heat pipes typically are low in weight and can be bent and reshaped to fit into a system. This robustness is extremely useful in weight and space constrained systems which require a low-profile method of removing heat.

The idea of integrating heat pipes into the thermal management of high frequency transformers has yet to be developed at the commercial level; however, studies exist that explore the implications of such a configuration. In an early study by Hansen and Chester, which is depicted in Figure 2.12, the direct integration of heat pipes into a 20 kHz, 1.52 kV transformer was tested and found to decrease the observed maximum temperature by 20°C [23]. While this demonstrates the intuitive expectation that heat pipes would enhance the movement of heat away from the transformer, a major barrier to their mass implementation is the impact on the electromagnetic performance of the system. For example, magnetic fields

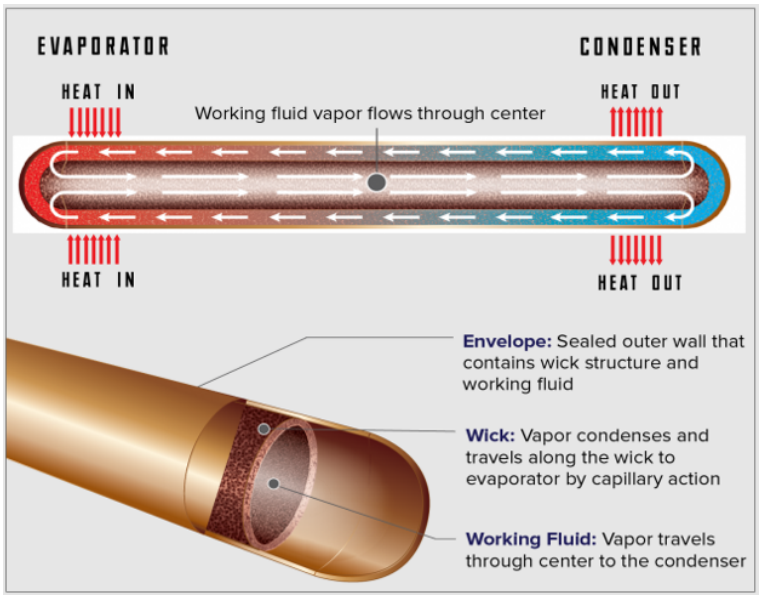

Figure 2.11: Illustration of heat pipe geometry and operation. [21].

generated by the transformer's operations can induce electrical currents on nearby magnetic surfaces, leading to additional heat generation. The impacts of these induced losses in any copper-walled heat pipes placed near a high frequency transformer could result in a system with higher temperatures than designed for if these effects are not properly mitigated. In the same study, Hansen and Chester noted the increase in heat losses in the heat pipe-embedded system, however, point out that it did not impede the setup from achieving the previously reported temperature drop. A study by Wrobel tabulated the induced losses on heat pipes when used to cool a high frequency transformer, with different wick structures as well as envelope materials being evaluated [24]. A plot showing the results for different tested heat pipes is shown in Figure 2.13, and confirms the increase in expected induced losses with larger operational frequencies. A notable finding from this study was the increasing growth rate of induced losses at higher transformer frequencies. Also of note was the impact of switching to titanium-walled heat pipes, which resulted in an order of magnitude lower losses compared to the standard copper-walled variants.

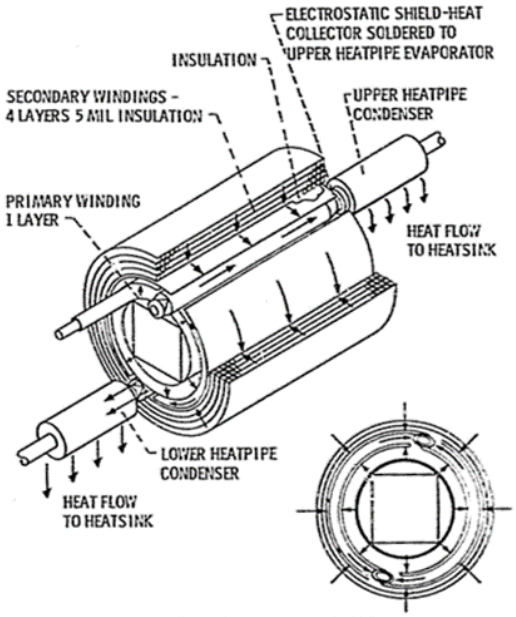

Figure 2.12: Heat-pipe integrated 20 kHz, 1.52 kV transformer, designed by Hansen and Chester. [23].

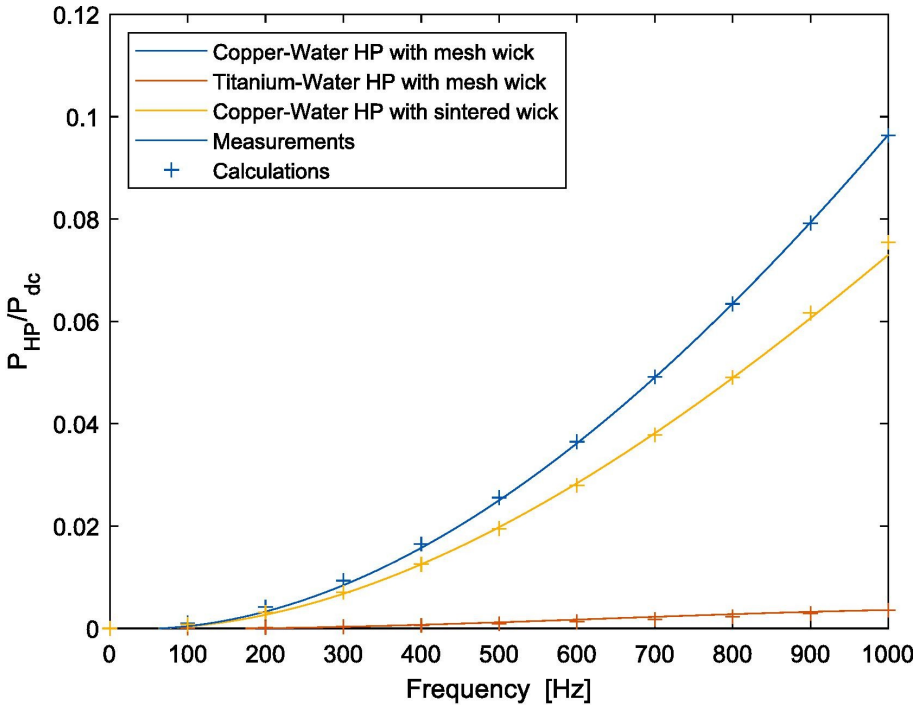

Figure 2.13: Measured heat pipe induced losses as a fraction of total transformer losses for different operational frequencies, as found by Wrobel. [24].

Chapter 3

Ferrite Thermal Conductivity Material Testing

Capturing the thermal properties of the transformer core is crucial to providing accurate temperature predictions for the heat-generating component. From a cooling perspective, the low expected thermal conductivity of the 3F36 ferrite material (3.5 - 5 W/m-K) [7] presents a challenge in removing heat from areas of the core furthest from the cold plate. The design of supplementary cooling solutions is further complicated by the 143% difference between the minimum and maximum values in the expected range. From a past analysis on an iPEBB core with similar geometry, losses, and thermal properties, a 50°C difference in maximum core temperatures was seen for a 175% difference in thermal conductivity values (4 - 7 W/m-K) under worst case model conditions [5]. In efforts to address this uncertainty, an experimental setup was created to measure the thermal conductivity of ferrite samples with the goal of providing confidence in either using the conservative end of the range or a higher value in modeling.

3.1 Experimental Design

The design of the thermal conductivity test assembly was based on the setup outlined by the September 1, 2020 revision of ASTM standard E1225-20 [25]. Details of the requirements of the standard and analysis of the test conducted within those requirements are presented below. All requirements of this method have been met with the exception of the temperature gradient of the guard cylinder and the precision of the temperature measurement sensors. Due to the limits of available instrumentation, the constructed setup does not fully meet the ASTM E1225-20 standard.

A graphic detailing the experimental setup can be found in Figure 3.1. The test uses two samples of 304 stainless steel, which will be referred to as the "meter bars", and one sample of Ferroxcube 3F36 ferrite, which is defined as the "specimen". All three pieces are cylindrical with a radius of $r_a = 1.9$ cm. The meter bars and specimen have heights of $l_m = 15.24$ cm and $l_s = 3.50$ cm respectively. When using the room-temperature thermal conductivity value of $k_m = 16.2$ W/m-K for stainless steel [26] and expected mean value of $k_s = 4.25$ W/m-K for ferrite, this sizing provides similar k_m/l_m and k_s/l_s ratios. The

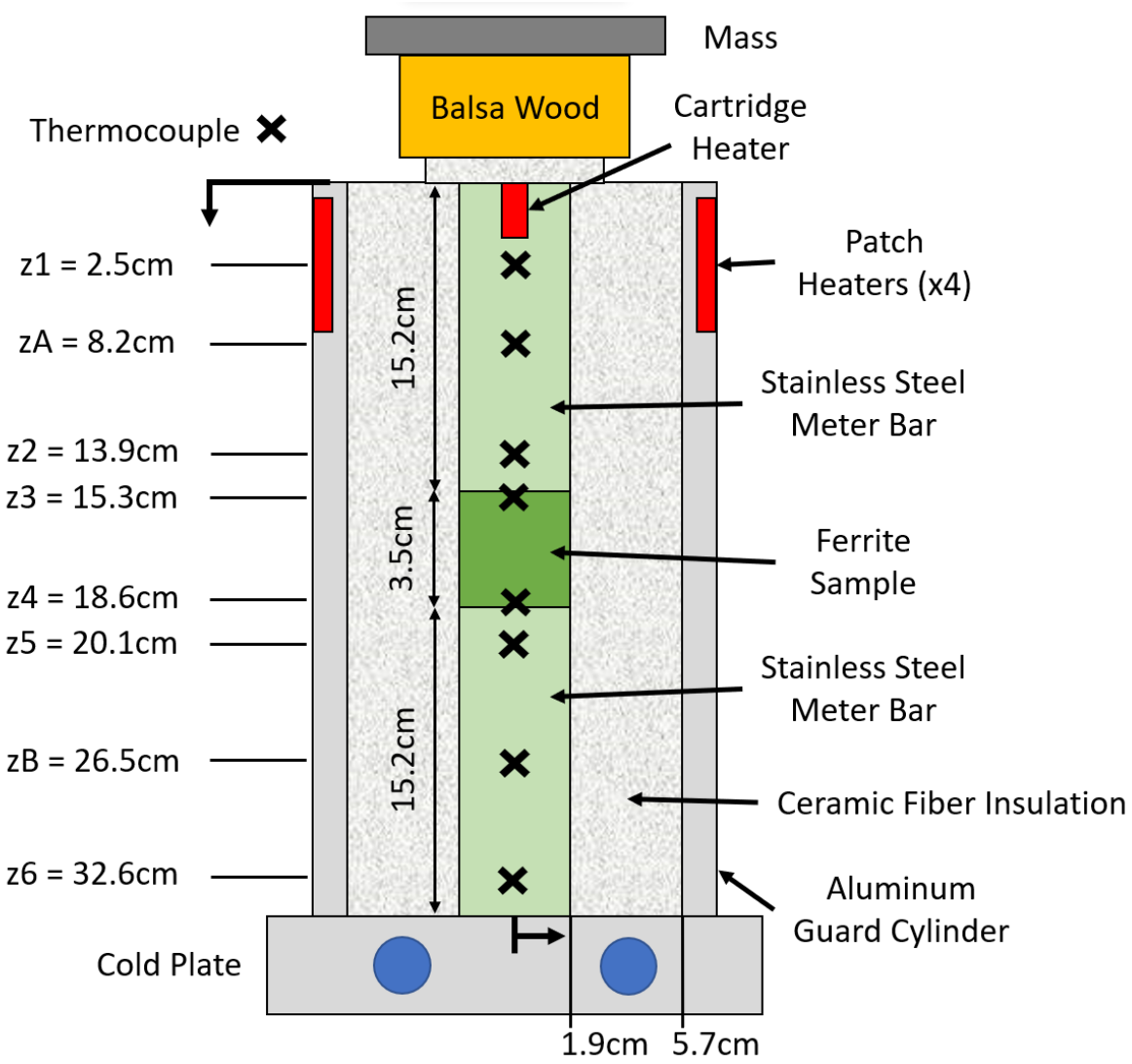

Figure 3.1: Cross-section diagram of the ferrite thermal conductivity test setup based on the ASTM E1225-20 standard.

pieces are stacked in a column with the specimen in between the two meter bars. In order to ensure constant contact pressure, a mass of 1.896 kg was placed on the top of the stack, which applied to the area of radius r_a adds a pressure of 16.4 kPa in addition to the dead weight of the stack. 8329TCS thermal epoxy was also applied at the ends of the specimen to reduce thermal resistance at these interfaces.

A cartridge heater placed into the upper meter bar acts as the heat source for the column, and is configured to provide 6.94 W of heat at 10 V. A cold plate with an inlet water temperature of 10°C is located at the bottom of the stack and serves as the heat sink. An IKA RC2 chiller is used to cool and circulate this water. The placement of source and sink are used to direct heat flow axially through the column. In order to limit radial heat losses to the environment, the central stack is surrounded by a 3.81 cm thick layer of UniTherm ceramic fiber insulation with a manufacturer-reported thermal conductivity of 0.03 W/m-

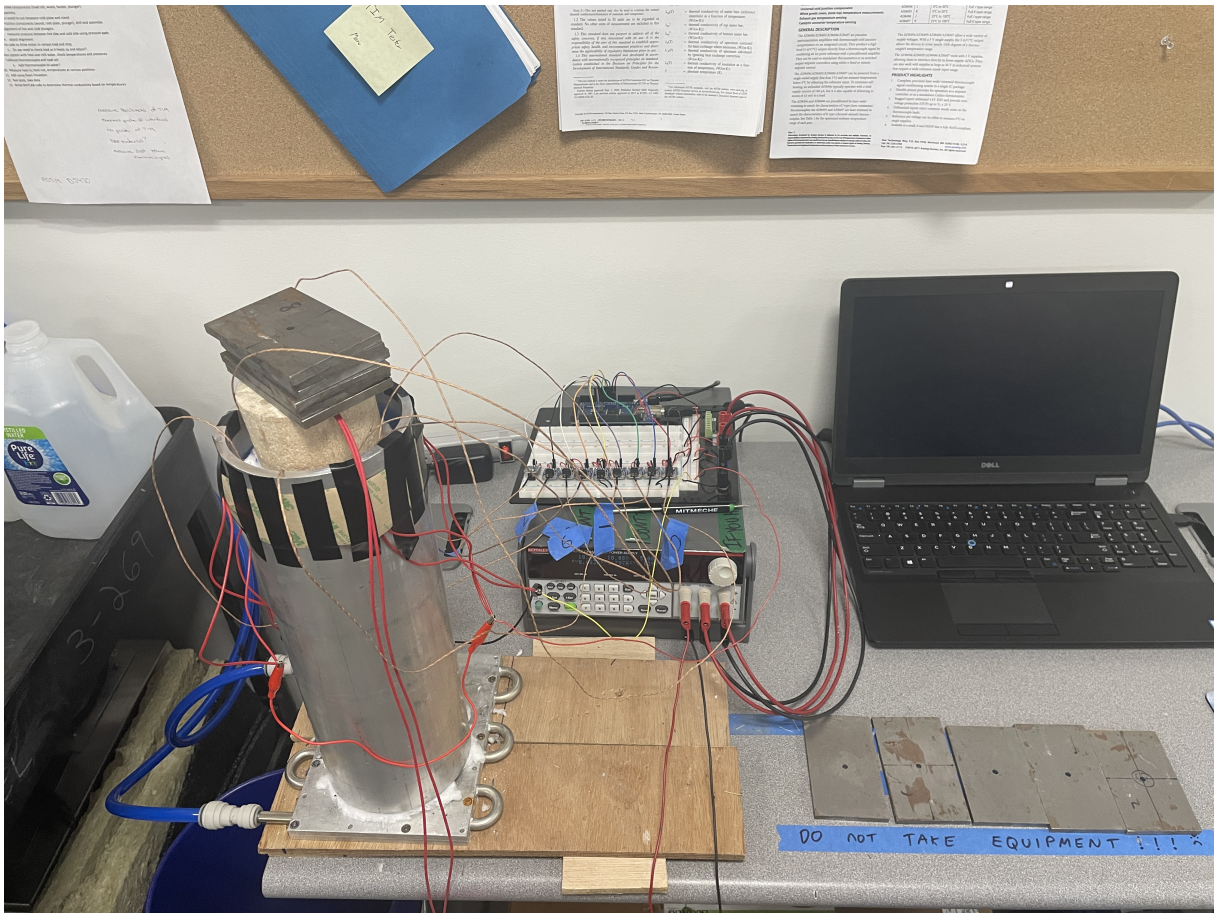

Figure 3.2: Photo of the ferrite experiment setup with all hardware wiring connected. The water chiller supplying the cold plate is out of frame, however, its tubing can be seen.

K [27]. Enclosing this layer of insulation is an aluminum cylindrical guard with inner radius $r_b = 5.7$ cm, providing a ratio of $r_b/r_a = 3$. Four patch heaters with a combined heat generation of 20.8 W are mounted to this surface to raise the radial boundary temperature. To reduce heat loss from the top of the column, a piece of balsa wood lined with insulation fiber is used to cover the otherwise exposed heat generating surface.

The temperature sensors used were the Adafruit K-type thermocouples which were connected to AD8495 analog thermocouple amplifiers. A Keithley 2231A-30-3 DC power supply provided 5 V to each thermocouple circuit, as well as powered the heat-generating components used in the setup. This temperature measurement setup had a combined accuracy of ± 2°C. For each of the meter bars, three thermocouples were attached using a small radial hole drilled half-way into the samples. Thermocouples A and B were not used in calculations and instead served to validate the recorded temperature gradients. For the specimen, two thermocouples were placed into radial slots on the top and bottom surfaces of the sample. All thermocouple attachment points used 8329TCS thermal epoxy to improve contact. The vertical distance of each thermocouple location relative to the top surface of the upper meter bar is shown in Figure 3.1 with a measurement uncertainty of 0.05 cm. An Arduino MEGA 2560 Rev2 was used to convert the thermocouple voltage outputs V_i to temperatures T_i in

°C using

$$T_i = \big(V_i - 1.25\big)/0.005 \tag{3.1}$$

where i is any thermocouple. A photo of the final test setup is shown in Figure 3.2.

With the heat loads and cold plate both active, the setup was monitored until fluctuations in temperature were less than 1°C/hr, which did not meet the ASTM E1225-20 requirement of 0.05°C/hr. Using temperatures at this state and the known locations of thermocouples along the stack z_i for i = 1-6, average heat fluxes q_{top} and q_{bot} through the top and bottom meter bars can be calculated.

$$q_{top} = k_m \frac{T_2 - T_1}{z_2 - z_1} \tag{3.2}$$

$$q_{bot} = k_m \frac{T_6 - T_5}{z_6 - z_5} \tag{3.3}$$

An estimate of the axial heat flow through the test specimen can be found by averaging the calculated heat flows. This mitigates the effects of radial heat losses along the stack.

$$q_s = \frac{q_{top} + q_{bot}}{2} \tag{3.4}$$

Finally, the thermal conductivity of the specimen can be calculated.

$$k_s = q_s \frac{z_4 - z_3}{T_4 - T_3} = \frac{k_m}{2}\Big(\frac{T_2 - T_1}{z_2 - z_1} + \frac{T_6 - T_5}{z_6 - z_5}\Big)\frac{z_4 - z_3}{T_4 - T_3} \tag{3.5}$$

The calculations for the uncertainty of each measured thermal conductivity, as well as for the averaging of results across samples can be found in Appendix A.

3.2 Results and Discussion

Prior to running experiments, an ice-water sample was used to confirm the manufacturer offset of the thermocouples. Calibration of the setup was then performed using a known sample of stainless steel in place of the ferrite sample. Thermal conductivity results on stainless steel 304 using identical stainless steel 304 meter bars were within ±12.8% of the accepted values for stainless steel over the temperature range 315 K to 343 K. The largest contribution to this error was the inaccuracy of the thermocouples used.

The experiment was conducted on three identical samples of 3F36 ferrite with five runs per sample, giving a total of 15 measurements for the thermal conductivity of the ferrite. Raw temperatures and calculated thermal conductivities with their corresponding uncertainties for each run $u_{s,onerun}$ can be found in Table 3.1. Sample-averaged results and uncertainties are also included in Table 3.2.

Based on recorded temperatures, all three samples are estimated to have thermal conductivity values well within the manufacturer provided range. The three calculated values sit above the median estimate of k_s = 4.25 W/m-K, which is favorable as higher thermal conductivity values improve the flow of heat within the ferrite core. The manufacturer guarantees that each sample will fall within the overall range of 3.5 - 5 W/m-K; however, due to

the non-homogeneous properties of the material, the manufacturer cannot ensure that the measured average of 4.25 W/m-K is representative of every manufactured sample. The results from this experiment provide reasonable confidence that, in practice, sections of ferrite will lean towards the higher end of the range.

Ultimately, it was decided to continue modeling ferrite in simulations as having a low thermal conductivity value of 3.5 W/m-K in order to account for any fluctuations that might occur in core manufacturing. This approach is conservative, however, it minimizes risk in the design of thermal solutions in response to the inhomogeneous properties of ferrite. The thermal conductivity of the ferrite model can be updated in the future once experimental results of the actual transformer with the proposed solution are available.

Table 3.1: Recorded Thermocouple (TC) Temperatures and Thermal Conductivities for Ferrite Samples

		Temperature (°C)						(W/m-K)	
		TC 1	TC 2	TC 3	TC 4	TC 5	TC 6	$k_{s,onerun}$	$u_{s,onerun}$
Sample 1	Run 1	115.23	84.96	77.15	44.92	41.99	10.74	4.28	0.48
	Run 2	110.35	80.08	71.29	41.99	39.06	10.74	4.49	0.54
	Run 3	112.30	80.08	73.24	42.97	40.04	10.74	4.57	0.53
	Run 4	110.35	82.03	75.20	45.90	39.06	11.72	4.26	0.52
	Run 5	109.38	82.03	74.22	45.90	39.06	11.72	4.33	0.54
Sample 2	Run 6	112.30	79.10	73.24	44.92	41.02	11.72	4.96	0.60
	Run 7	108.40	77.15	71.29	43.95	40.04	11.72	4.90	0.61
	Run 8	107.42	76.17	70.31	43.95	40.04	11.72	5.08	0.65
	Run 9	112.30	81.05	75.20	46.88	37.11	11.72	4.50	0.56
	Run 10	112.30	81.05	75.20	46.88	37.11	11.72	4.50	0.56
Sample 3	Run 11	108.40	77.15	71.29	41.99	39.06	11.72	4.50	0.54
	Run 12	110.35	78.13	72.27	42.97	39.06	11.72	4.57	0.55
	Run 13	111.33	80.08	73.24	43.95	40.04	11.72	4.57	0.55
	Run 14	110.35	78.13	71.29	42.97	39.06	11.72	4.73	0.58
	Run 15	109.38	78.13	71.29	41.99	39.06	11.72	4.50	0.54

Table 3.2: Averaged Ferrite Sample Thermal Conductivities

	(W/m-K)		
	$k_{s,mean}$	$u_{s,tot}$	Standard Deviation
Sample 1	4.38	0.29	0.14
Sample 2	4.79	0.43	0.27
Sample 3	4.57	0.27	0.09

Chapter 4

Litz Wire Radial Thermal Conductivity

The 144 W of heat generation expected from the transformer coils [3] combined with the current positioning of the coils and their lack of a direct connection to a heat sink risks the presence of hot spots that can affect electrical performance and lead to potential damage. In order to develop a conduction-based method of extracting heat from the coils, the thermal properties of the litz wire used must be known to ensure accurate modeling of heat flow through them to the proposed cooling solution. Understanding the radial thermal conductivity of the coils is crucial as any solution will require heat to flow across the wire's cross section. In order to accurately capture this behavior, two approaches of determining the radial thermal conductivity of our litz wire were pursued: an analytical approach using an existing mathematical model and an experiment to validate the calculated value. The goal of this work is to provide an input to the thermal simulation models and provide confidence in the expected temperature of the coils under worst case conditions.

4.1 Analytical Model

Before starting, it is important to get an understanding of the litz wire we are modeling and use available information to determine the best modeling approach. As determined by Sharfeldden, the iPEBB transformer uses an overall 8 AWG litz wire with 5x5x3/56/44 strand configuration and an outer FEP jacket to 0.211" OD [3]. This is essentially 4200 strands of 44 AWG wires bundled together to form the complete sample. Additional information such as strand orientation and contact angles were not readily available from the manufacturer; however, having a rough idea of the cross-section allows for modeling using the Gasar porous metal materials model presented by Liu et al. [17]. This section will walk through those calculations applied to our litz wire.

The chosen approach models each unit cell of wire as being enveloped by uniform layers of insulation and air. It is key to note that this assumption is conservative as it forces heat to pass through the high thermal resistances of the insulation and air in all directions, when in reality there exist paths of contact between the copper strands. For a visual representation of the litz model being used, refer to Figure 2.8.

First, we identify our unit cell as consisting of one 44 AWG strand along with a uniform layer of insulation and air. The total wire of 8 AWG size has an inside area of $A_3 = 1.66*10^{-5}$

m^2. Dividing this area across our 4200 strands gives a unit cell area of $A_{3'} = 3.95 * 10^{-9}$ m^2. Within our unit cell, we now have to determine the dimensions of the copper, air, and insulation sections. The 44 AWG copper strand has a known area of $A_1 = 2.03 * 10^{-9}$ m^2. The thicknesses of insulation and air per unit cell are not directly known; however, an approximation can be made by subtracting the known area of copper from the total usable area. This estimation gives us the total non-copper area of the litz wire, however, to split this between air and insulation requires a further assumption regarding the ratio of the two. The median case assuming 50% of non-copper area is insulation will be used as a baseline for the following calculations. Using this value, we find that the area of copper plus insulation for each unit cell is $A_2 = 2.99 * 10^{-9}$ m^2. In order to account for this approximation, thermal simulations for the final solution design iteration will also undergo a sensitivity study using the litz radial thermal conductivity values seen in Figure 4.1.

Next, we must define the materials modeled in each cell layer along with their respective thermal conductivities. The strands will use the value of copper, $k_c = 398$ W/m-K [28]. The gaps will be modeled as air since this specific wire is not potted in an epoxy material, giving a value of $k_a = 0.025$ W/m-K [29]. The insulation coating on each of the individual strands is unknown; however, varying its thermal conductivity value was found to have a small impact on the overall calculation relative to varying the ratio of insulation and air areas. As a result, an arbitrary value of $k_i = 1.6$ W/m-K was chosen based as an average of commonly used wire enamel materials such as glass and porcelain. The planned sensitivity study using the ratio of insulation and air areas will cover a wide range of possible thermal conductivities which should address the errors associated with both the modeling process and assumed values.

After converting our previously mentioned areas into radii, we can then size a rectangular cell of equivalent area using the equation $d_i = r_i\sqrt{\pi}$ for i = 1-3. The relevant dimensions can be seen in Table 4.1.

Table 4.1: Relevant dimensions for the radial litz model outlined by Liu et al. [17]

Parameter	Dimension (10^{-5} m)
r_1	2.54
r_2	3.08
r_3'	3.55
d_1	4.50
d_2	5.47
d_3	6.29

Using these cell dimensions and thermal conductivity values, we can then plug into the equation for effective radial thermal conductivity developed by Liu et al. [17].

$$k_{litz,r} = k_a(1-\sqrt{n}) + k_i(1-\sqrt{m}) + \frac{k_a k_i k_c \sqrt{mn}}{k_c k_a(\sqrt{n}-\sqrt{mn}) + k_i k_c \sqrt{m}(1-\sqrt{n}) + k_a k_i \sqrt{mn}} \quad (4.1)$$

where $m = d_1^2/d_2^2$ and $n = d_2^2/d_3^2$ are used to simplify the algebra. The result is a radial thermal conductivity $k_{litz,r} = 0.45$ W/m-K. This value is low compared to the calculated

value $k_{ref,r} = 1.76$ W/m-K of the litz wire used by Liu et al.; however, the difference can be mostly attributed to their sample using epoxy to improve heat transfer across internal gaps [17]. When repeating the calculation for our litz sample but substituting epoxy-filled gaps instead of air-gaps, we see a calculated value of $k_{litz,epoxy,r} = 1.67$ W/m-K.

Repeating the calculation in 4.1 across the possible insulation area ratios results in a range of expected thermal conductivity values shown in Figure 4.1. These will be used as the basis of a sensitivity study in thermal simulation in order to ensure that the designed solution is capable of satisfying coil temperature requirements in the most conservative conditions.

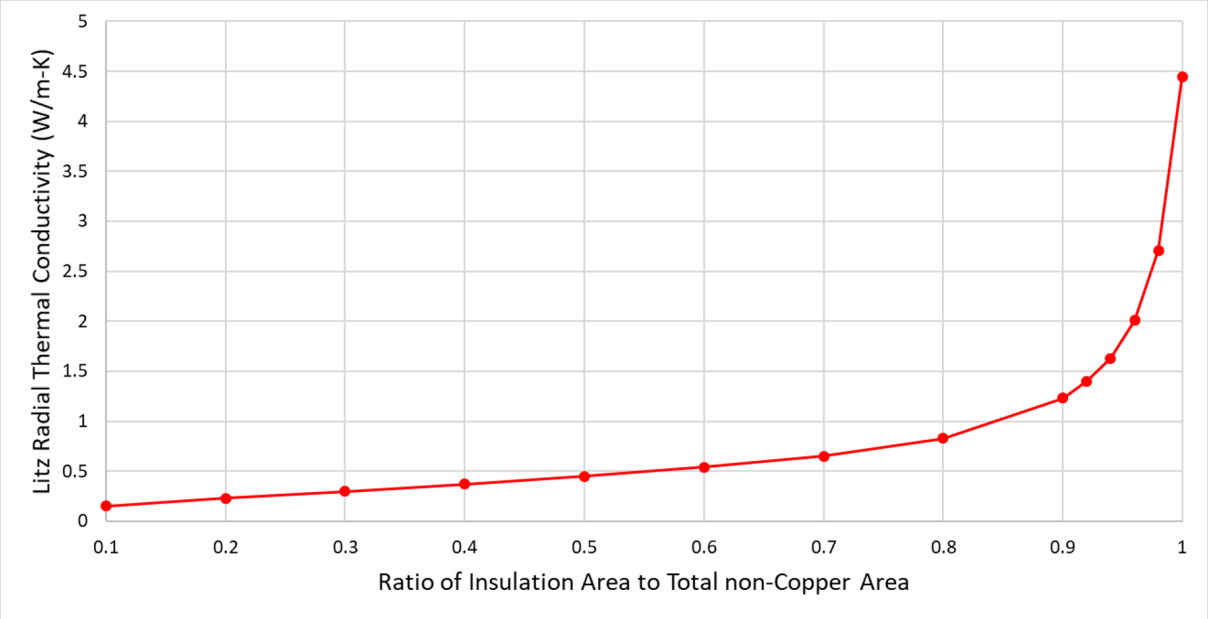

Figure 4.1: Litz radial thermal conductivity for different inside insulation area ratios.

One last thing to note is that this calculation for the effective radial thermal conductivity is only considering the effects of copper, insulation, and air-gaps within the wire. In order to account for the effect of the outer layer of polyurethane nylon insulation on radial heat flow, an area-independent thermal resistance is applied to the outer wire surface interface. Using the known sleeve thickness $L_{sleeve} = 3.81 * 10^{-4}$ m (0.015 in.) and approximate thermal conductivity $k_{sleeve} = 0.25$ W/m-K [30], we can calculate the resistance value to be added to our model.

$$R_{sleeve}A = \frac{L_{sleeve}}{k_{sleeve}} = \frac{(3.81 * 10^{-4})\ m}{0.25\ W/mK} = 1.52 * 10^{-3}\ Km^2/W \tag{4.2}$$

4.2 Experimental Design

The design of the litz wire thermal conductivity experiment was based on a similar setup presented by Liu et al., from which the effective radial thermal conductivity was measured for a sample of litz wire [17]. This setup was in turn a variation of the November 1, 2017 revision of ASTM standard D5470-17, which measures the apparent thermal conductivity

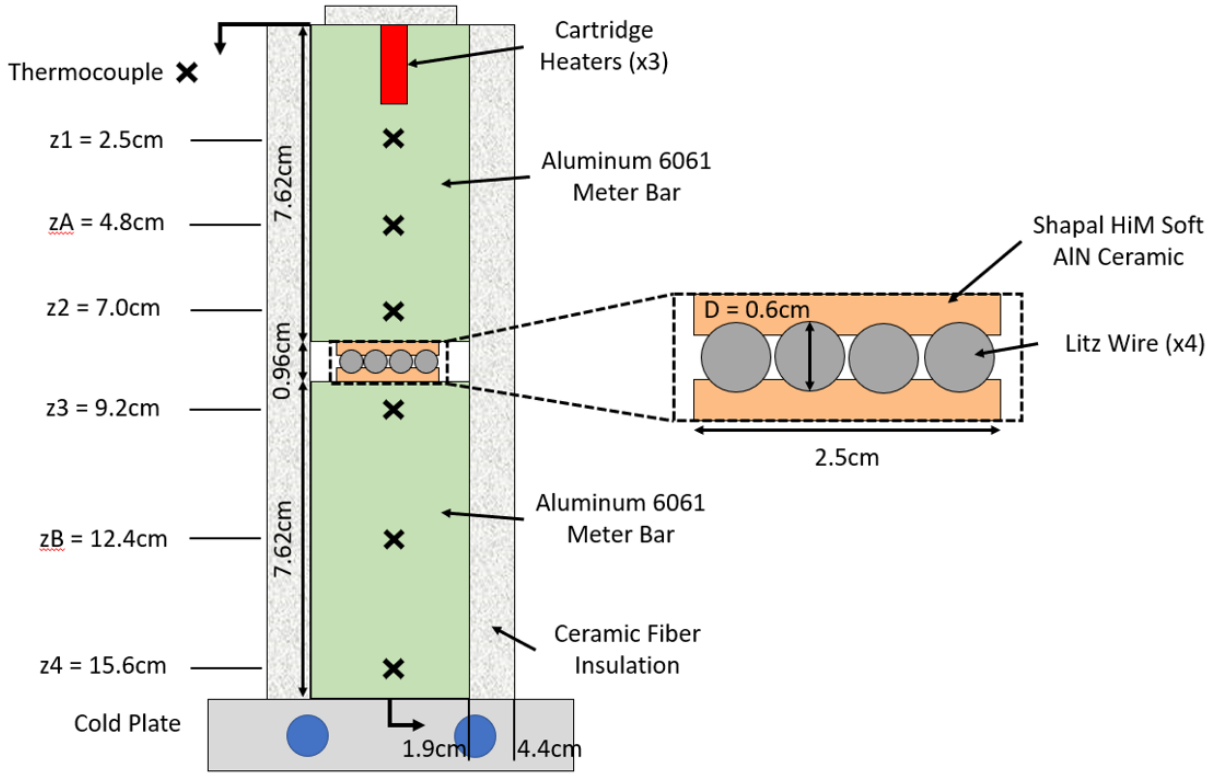

Figure 4.2: Cross-section diagram of the litz thermal conductivity test setup based on the ASTM D5470-17 standard.

of a uniform-thickness test specimen [31]. Variations to the standard were made to account for the non-uniform specimen thickness resulting from the tubular-shaped litz samples, with details of the final setup being presented below.

A graphic detailing the experimental setup can be found in Figure 4.2. The test uses two samples of 6061 aluminum as the meter bars, both of a rectangular cross section with width $w_m = 3.81$ cm, length $l_m = 7.62$ cm, and height $h_m = 7.62$ cm. The test specimen consists of four 7.10 cm long samples of the litz wire described in Section 2.1.2. Shapal HiM Soft AlN ceramic spacers separate the specimen from both meter bars to maintain the profile of the litz samples against possible compression. These ceramic spacers were also designed without direct contact between the two spacers, ensuring that the flow of heat along the stack directly passes through the litz samples and does not bypass the wires via the spacers. Corsair XTM50 thermal paste was applied at the interfaces between the ceramic spacers and aluminum meter bars as well as between litz samples and the ceramic spacers. The relevant thermal conductivities of the aluminum meter bars, ceramic spacers, and thermal paste are $k_m = 167$ W/m-K [32], $k_c = 92$ W/m-K [33], and $k_p = 5$ W/m-K [34] respectively.

Three cartridge heaters were placed into the upper meter bar to act as the heat source for the column, providing a combined 44.86 W of heat with the two flanking heaters set at 15 V and the center heater set at 14 V. A cold plate with an inlet water temperature of 10°C was located at the bottom of the stack and serves as the heat sink. Just as in the ferrite experiment outlined in Section 3, an IKA RC2 chiller was used to cool and

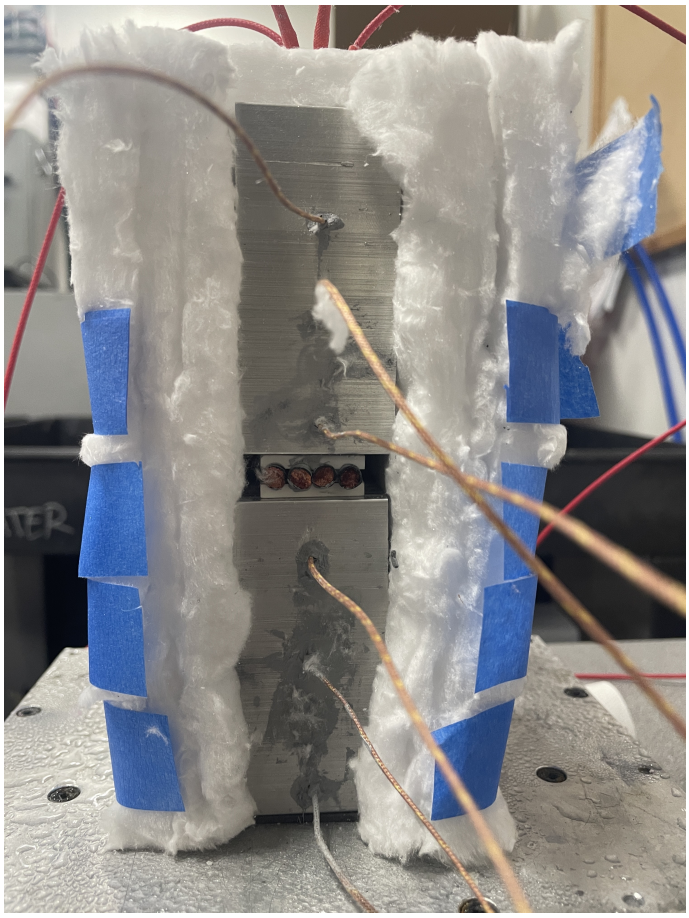

Figure 4.3: Photo of the litz experiment setup with the near side insulation removed for view of the internal stack.

circulate this water. In order to limit radial heat losses to the environment, the central stack was surrounded by a 2.54 cm thick layer of UniTherm ceramic fiber insulation with a manufacturer-reported thermal conductivity of 0.03 W/m-K [27]. An image of the final setup can be seen in Figure 4.3.

The temperature measurement hardware used was identical to that of Section 3, and importantly provided readings with a combined accuracy of ±2°C. For each of the meter bars, three thermocouples were attached using a small radial hole drilled half-way into the samples. Thermocouples A and B as named in Figure 4.2 were not used in calculations and instead served to validate the recorded temperature gradients. All thermocouple attachment points used Corsair XTM50 thermal paste to improve contact. The vertical distance of each thermocouple location relative to the top surface of the upper meter bar is shown in Figure 4.2 with a measurement uncertainty of 0.05 cm. As in the ferrite experiment, Equation 3.1 was used to convert the directly measured voltage readings to temperatures. With the heat loads and cold plate both active, the setup was monitored until fluctuations in temperature were less than 1°C/hr.

No thermocouples were able to be placed within the specimen, and instead this test method relied on the meter bar readings to extrapolate the temperatures at the top and bot-

tom faces of the ceramic holders. Using recorded temperatures and thermocouple positions along the stack z_i for i = 1-6, heat fluxes through the top and bottom meter bars q_{top} and q_{bot} can first be calculated.

$$q_{top} = k_m \frac{T_2 - T_1}{z_2 - z_1} \tag{4.3}$$

$$q_{bot} = k_m \frac{T_4 - T_3}{z_4 - z_3} \tag{4.4}$$

Averaging these values provides an estimate for the heat flux through the specimen located between the meter bars while accounting for possible radial heat losses along the stack.

$$q_s = \frac{q_{top} + q_{bot}}{2} \tag{4.5}$$

Next, extending the recorded temperature profiles in each meter bar allows for a calculation of the surface temperature at the top and bottom ceramic holder faces.

$$T_{topface} = T_2 - (q_{top} A_m) \frac{h_m - z_2}{k_m A_m} \tag{4.6}$$

$$T_{botface} = T_3 + (q_{bot} A_m) \frac{z_3 - h_m - h_g}{k_m A_m} \tag{4.7}$$

where A_m is the cross sectional area of the meter bars and h_g is the height of the gap created by the specimen and ceramic spacers.

The effective thermal resistance across the gap can be approximated using the known properties of the ceramic holder and known geometry of the litz wire. Heat flow through the gap is represented through a thermal resistance network in Figure 4.4, where the approximate thermal resistances of the ceramic holders and thermal paste layers are given by the equations below. For simplification, the ceramic holders were modeled as slabs of uniform thickness L_c = 2 mm. Similarly, the curvature of the contact area between the ceramic and litz samples was neglected and the layer of thermal paste at the interface was modeled as a slab of thickness L_p = 0.11 mm.

$$R_c = \frac{L_c}{k_c A_c} \tag{4.8}$$

$$R_p = \frac{L_p}{k_p A_p} \tag{4.9}$$

where A_c is the cross sectional area of the ceramic holder and A_p is the contact area between each litz sample and the ceramic.

Simplifying this thermal network results in the effective resistance across the gap R_{gap}.

$$R_{gap} = 2R_c + \frac{1}{4}(2R_p + R_{litz}) \tag{4.10}$$

Plugging this value into Fourier's law for conduction across the gap provides us with an expression that can be rewritten for the effective cross-sectional thermal resistance of the litz sample.

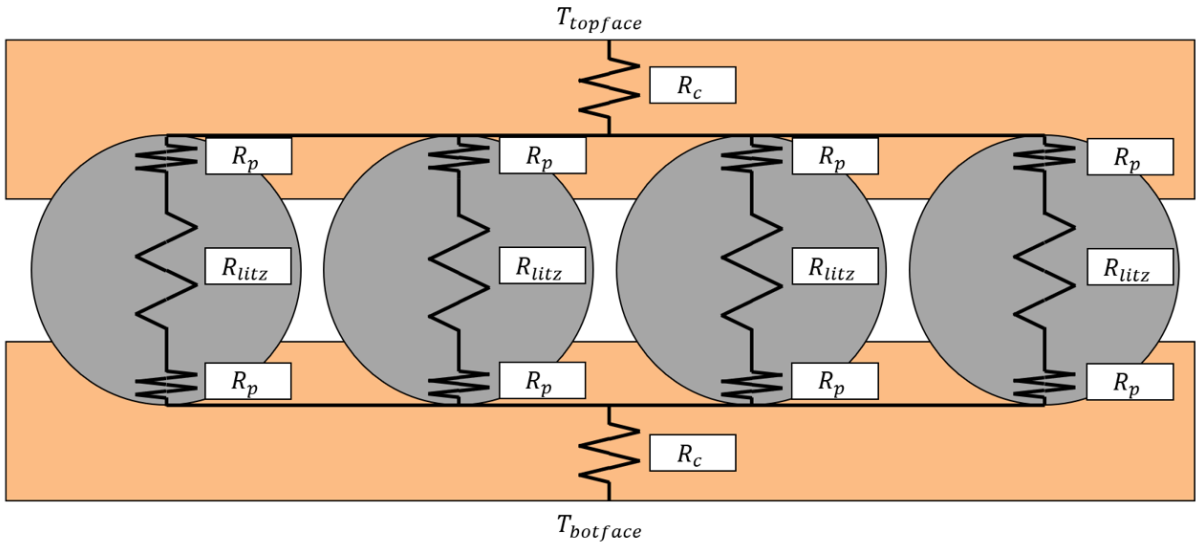

Figure 4.4: Thermal resistor network for the gap consisting of the ceramic spacer, litz specimen, and thermal paste interfaces.

$$(T_{topface} - T_{botface}) = q_s A_m R_{gap} \tag{4.11}$$

$$R_{litz} = 4\Big(\frac{(T_{topface} - T_{botface})}{q_s A_m} - 2R_c\Big) - 2R_p \tag{4.12}$$

The litz wire can be modeled as a slab with a height equal to its diameter D_{litz} and an area given by the wire's average vertical cross-sectional profile $A_{avg,litz}$. This approximation retains the same total volume as the litz wire sample. The final expression for the effective radial thermal conductivity of the litz sample k_{litz} is then given by the following.

$$k_{litz} = \frac{D_{litz}}{R_{litz} A_{avg,litz}} \tag{4.13}$$

A MATLAB script distributed on the MATLAB Central File Exchange was used to calculate the propagation of uncertainty for each individual experimental run [35]. The final MATLAB code which utilizes the online script is included in Appendix B. Equations A.2, A.3, and A.4 were used to determine the total uncertainty of the final averaged result.

4.3 Results and Discussion

The experiment was conducted for a total of five runs on a sample of 8 AWG litz wire with with 5x5x3/56/44 strand configuration and an outer polyurethane nylon jacket to 0.211" OD. Raw temperatures and calculated thermal conductivities with their corresponding uncertainties for each run $u_{litz,onerun}$ can be found in Table 4.2. The run-averaged results are included in Table 4.3.

Estimates from the analytical model in Section 4.1 using the Gasar porous metal materials model provided an expected radial thermal conductivity range between 0.15 W/m-K and 4.45 W/m-K for our litz sample. The variance in values was primarily due to the unknown packing ratio within the wire. Based on the temperatures seen over the five experimental runs, the recorded radial thermal conductivity of the litz sample aligns with this established range with a mean value of $k_{litz,mean}$ = 1.31 W/m-K. This agreement in results through analytical and experimental methods provides confidence in our estimate.

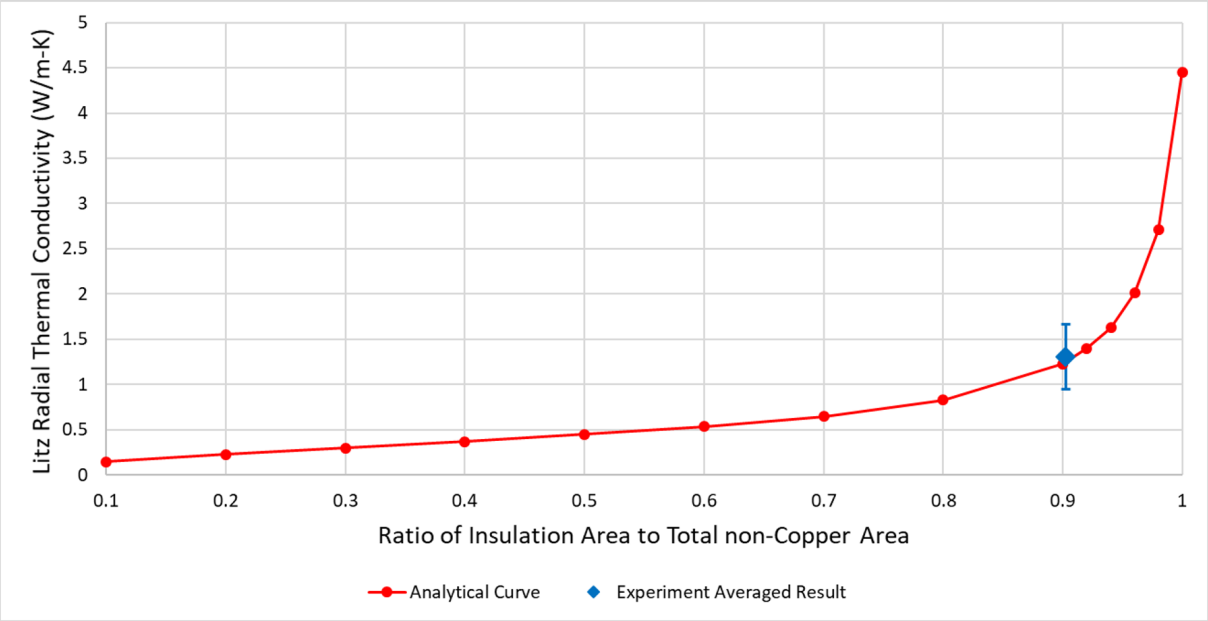

Figure 4.5: Litz radial thermal conductivity for different inside insulation area ratios (red) with the experiment averaged reading added (blue).

Each individual run had a high relative uncertainty associated with its measured thermal conductivity; however, this concern was reduced by repeating the experiment. The low standard deviation of 0.09 W/m-K seen across the five runs provided confidence in the precision and replicability of the setup. The run-averaged reading of $k_{litz,mean} = 1.31 \pm 0.36$ W/m-K still covers a wide range of possible thermal conductivity values; however, it does narrow the range derived from the analytical calculations of 0.15 W/m-K - 4.45 W/m-K.

Going forward, this mean recorded value of $k_{litz,mean}$ = 1.31 W/m-K will be utilized in the thermal models as the cross-sectional effective thermal conductivity of the litz wire. In addition, an area-independent thermal resistance value of $R_{sleeve} * A = 1.52{*}10^{-3}$ K*m^2/W will be applied to the outer coil interface in order to account for the outer-most layer of polyurethane nylon insulation. Thermal solutions will be designed with these properties in mind; however, for the final proposed configuration, a simulation sweep using the range of radial litz thermal conductivity values from Figure 4.1 will also be performed to test the robustness of the final design and cover for the still high-relative uncertainty from experimental results.

Table 4.2: Recorded Thermocouple (TC) Temperatures and Thermal Conductivities for Litz Sample

	Temperature (°C)				(W)			(W/m-K)	
	TC 1	TC 2	TC 3	TC 4	Q_{topbar}	Q_{botbar}	Q_{avg}	$k_{litz,onerun}$	$u_{litz,onerun}$
Run 1	139.65	135.74	17.58	13.67	42.65	28.85	36.25	1.41	0.78
Run 2	139.65	135.74	16.60	13.67	42.65	22.37	32.51	1.25	0.76
Run 3	137.70	133.79	16.60	13.67	42.65	22.37	32.51	1.27	0.78
Run 4	136.72	132.81	16.60	13.67	42.65	22.37	32.51	1.28	0.78
Run 5	135.74	131.84	16.60	13.67	42.54	22.37	32.46	1.29	0.79

Table 4.3: Averaged Litz Sample Thermal Conductivity

(W/m-K)		
$k_{litz,mean}$	$u_{litz,tot}$	Standard Deviation
1.31	0.36	0.09

Chapter 5

Transformer Cooling Solution Design

With the relevant input parameters determined, transformer cooling concepts can be explored in StarCCM+. First, the concept of supplementing a cold plate heat sink with forced air cooling was modeled based on a known experimental setup. This serves as both a validation of the transformer's modeling approach as well as a reference for later proposed cooling solutions. This thesis then focuses on the development of a heat pipe based cooling solution through an iterative design process.

5.1 Baseline Assumptions

The construction of the transformer model is based off the geometry and features provided by Sharfeldden [3] and outlined in Section 2.1.2. The thermal conductivity values of relevant materials are included in Table 5.1, which also includes additional materials that will be introduced in later heat pipe design sections. The rationale behind the values for ferrite and the radial coil orientation are based on both manufacturer-provided information and the findings of Sections 3 and 4 respectively.

Table 5.1: Thermal Conductivities for the iPEBB Transformer Thermal Model

Part	Material	Thermal Conductivity k (W/m-K)
Core	Ferrite 3F36	3.5
Coil (Along Winding, Axial)	Copper	398 [28]
Coil (Radial)	Composite	1.31
Mica Sheet	Mica	0.3 [36]
Plastic Wireholder	PLA Plastic	0.183 [37]
Ceramic Heat Spreaders	Shapal HiM Soft AlN Ceramic	86 [33]
Aluminum Heat Spreaders	Aluminum 6061	167 [32]
Heat Pipes	n/a	10,000 - 15,000
Potting Insulation	Epoxy Composite	0.85 [13]

The core was modeled with a constant, uniform distribution of its heat generation. Its conservative thermal conductivity estimate was applied as an isotropic value across the entire

volume. The litz coils were also modeled as a uniform volumetric heat source; however, its thermal conductivity was split into radial and axial components to account for the construction of the wire. Heat transfer along the coil is dominated by the copper strands, and thus the thermal model approximates its axial orientation as having the thermal conductivity of copper. For the radial direction, an effective thermal conductivity is used based on analytical estimates and experimental results.

The outer surface of the coils has an area-independent thermal resistance applied to the interface in order to account for the effects of the outer polyurethane nylon sleeve. The relevant calculation is given by Equation 4.2. The impact of interface contact resistance for other component interactions is also considered using this approach. It is assumed that a variant of thermal epoxy will be used at all surfaces of contact between the core, mica sheet, and plastic wireholders, as well as any additional components that are added in later design configurations. The area-independent thermal resistance of the thermal epoxy is estimated using an example manufacturer reported thermal conductivity and bondline thickness value, $k_{epoxy} = 2.1$ W/m-K and $L_{epoxy} = 1.50 * 10^{-5}$ m [38].

$$R_{epoxy}A = \frac{L_{epoxy}}{k_{epoxy}} = \frac{(1.50 * 10^{-5})\ m}{2.1\ W/mK} = 7.14 * 10^{-6}\ Km^2/W \tag{5.1}$$

The primary heat sink for all cases that were modeled is a cold plate, including both the current iPEBB variant shown in Section 2.1.4 [9] as well as an off-the-shelf model; however, to increase the speed of simulations, fluid flow through the heat sinks was not modeled. Instead, a standalone transformer model with temperature boundary conditions at the surfaces of contact with the cold plate was used, with the boundary temperatures being pulled from a separate cold plate-only simulation. This approach allows for a smaller cell count and eliminates the usage of fluid flow solvers, greatly reducing the required computation time and improving the efficiency of model iteration development. A final iPEBB-level simulation with full cold plate fluid flow was later completed to validate the assumptions made in the transformer standalone model, and can be found in Chapter 6.

For the heat losses, it was stated in Section 2.1.2 that the worst case conditions of the core and coils are 480 W and 144 W respectively. The actual losses can vary depending on the load and usage pattern; however, these maximum values will be applied as a constant heat source for a conservative thermal analysis. Three typical test cases will be used, and will be referred to as the open circuit, short circuit, and combined losses cases. With the exception of the airflow correlation study in Section 5.2.2, all simulation runs will use these cases as shown in Table 5.2.

Table 5.2: Transformer Operations Loss Scenarios

Scenario Name	Total Core Losses (W)	Total Coil Losses (W)
Open Circuit	480	0
Short Circuit	0	144
Combined Losses	480	144

5.2 Airflow Cooling Models

5.2.1 Thermal Model

The configuration for the airflow cooling reference is based on experiments performed by the Virginia Tech Center for Power Electronics Systems (CPES) on the iPEBB transformer [4]. In this study, which is shown in Figure 5.1, the transformer was placed within a closed box with a 7-fan air cooling system consisting of three front facing intakes and 4 side facing outputs. In addition, an off-the-shelf cold plate was used on the upper and lower faces of both core halves to replicate the planned iPEBB rack-mounted configuration. An open circuit test was ran for 35 minutes with temperature monitoring of the core performed by four surface-mounted thermocouples whose approximate locations are indicated in Figure 5.1b.

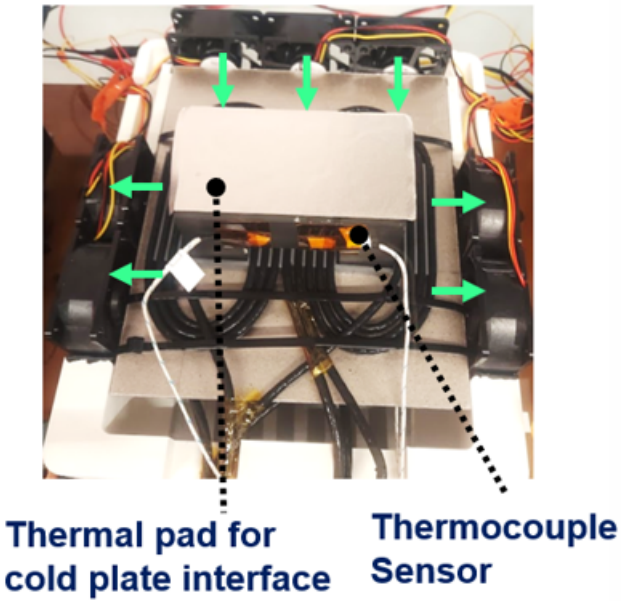

(a) Cooling fan configuration and view of setup.

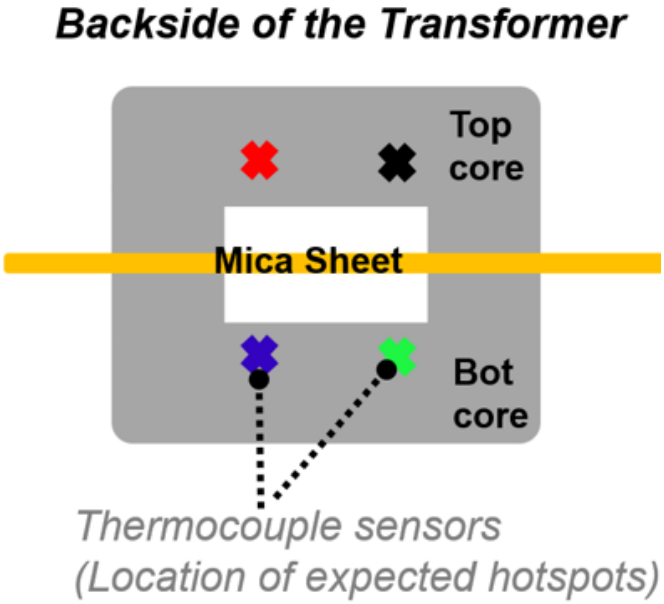

(b) Approximate thermocouple locations on transformer core.

Figure 5.1: Setup of the iPEBB transformer open circuit experiment performed by Virginia Tech. [4]

Airflow circulation was accounted for in StarCCM+ through the usage of face boundaries, with the front facing inlet and side facing outlets moving 38.8 cfm of air per fan at the presumed ambient temperature of 20°C. Air was modeled as an incompressible fluid with gravity also being enabled throughout the region. Constant temperature boundaries set to 16°C were defined at the upper and lower core faces to represent the cold plate heat sink. A summary of the relevant boundary conditions can be seen in Figure 5.2.

These airflow simulations were each run as a steady steady analysis for a total of 2000 timesteps, which was verified to ensure the convergence of all relevant parameters.

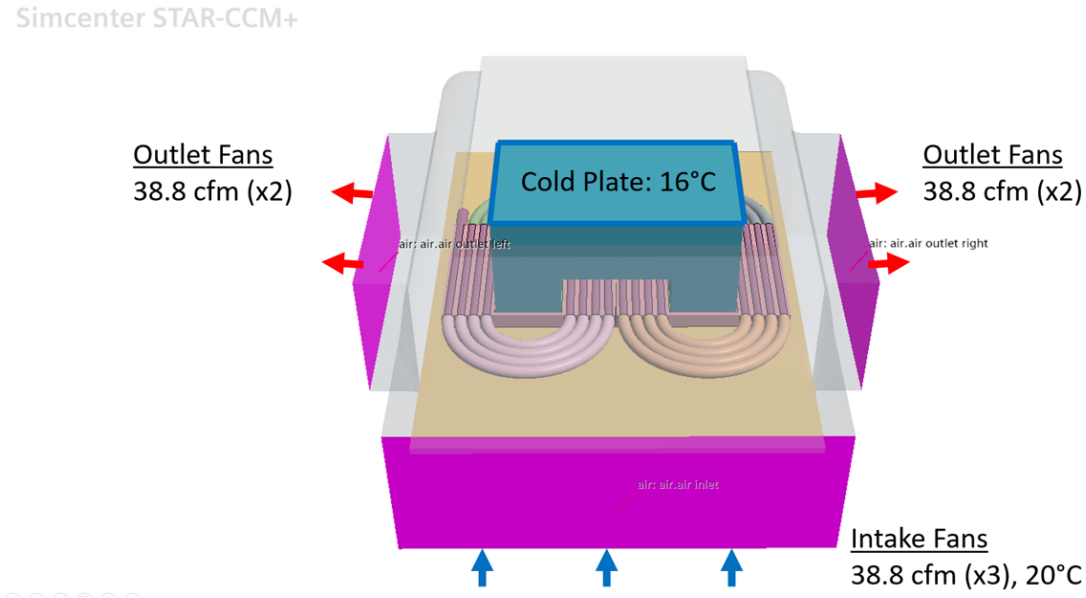

Figure 5.2: StarCCM+ thermal model of the airflow configuration with boundaries highlighted. The cold plate boundary on the lower core half is not visible. Temperatures shown are for the experiment correlation run.

5.2.2 Experiment Correlation

The goal of the initial airflow simulation runs was to reproduce the results seen in the experiments conducted by Virginia Tech; however, uncertainty regarding the core losses actually seen and the core's thermal conductivity value meant that a design sweep across these two parameters was required. For these correlation runs, core losses were tested between 400 W and 480 W, and ferrite's thermal conductivity between 3.5 W/m-K and 5 W/m-K.

Core thermocouple temperatures are compared between simulation runs and the recorded experiments in Table 5.3. Coil temperatures are not included as this was an open circuit test with no coil heating. The results show a disconnect between simulation predicted thermocouple temperatures and those seen in the experiment; however, this can be partly attributed to measurement error in the physical setup. Steel-tipped thermocouples were taped to the core surface without any thermally conductive paste, rather than being embedded into the material, and as a result the expectation was that recorded values would be underestimates of the true core surface temperature due to the majority of the sensor's surface being exposed to air. Using air temperatures from the simulation run, the thermal boundary layer was able to be visualized and used to estimate the temperature profile of the thermocouple tip surface. This approximation for one case can be seen in Figure 5.3. Although not exact, this approach confirmed the general trend seen between simulation and experimental runs and showed similar results when corrected.

The agreement seen between results provided confidence in the airflow model; however, now the takeaway was the core hot spot temperatures predicted by the simulations. Although experimental results indicate that airflow was sufficient for cooling the transformer coils, simulation results show core internal temperatures far exceeding the 100°C limit of ferrite.

Table 5.3: Airflow Correlation Thermocouple Values for Simulation Runs. Bottom Row Shows Experiment Measurements for Reference

Core Losses (W)	Ferrite Thermal Conductivity (W/m-K)	Thermocouple Locations (°C) Black	Blue	Green	Red	Core Maximum (°C)
400	3.5	90.0	89.4	91.9	90.6	154.2
	4.2	82.3	80.5	83.6	83.0	140.5
	5	74.0	73.4	75.3	74.5	126.4
440	3.5	98.2	94.8	99.6	98.8	170.0
	4.2	87.1	85.8	88.4	87.6	147.0
	5	79.6	80.0	80.5	82.4	138.9
480	3.5	105.3	102.0	107.2	105.9	181.6
	4.2	95.0	93.5	96.8	95.9	163.0
	5	85.4	83.8	86.7	85.9	147.3
Experiment Measurements		48.0	55.0	62.0	55.0	unknown

In addition, the legs of the core furthest from the cold plate were confirmed to be the region experiencing the highest temperatures due to the thermal resistance of the ferrite as well as the overlap in heat spreading from the close proximity of the two cores.

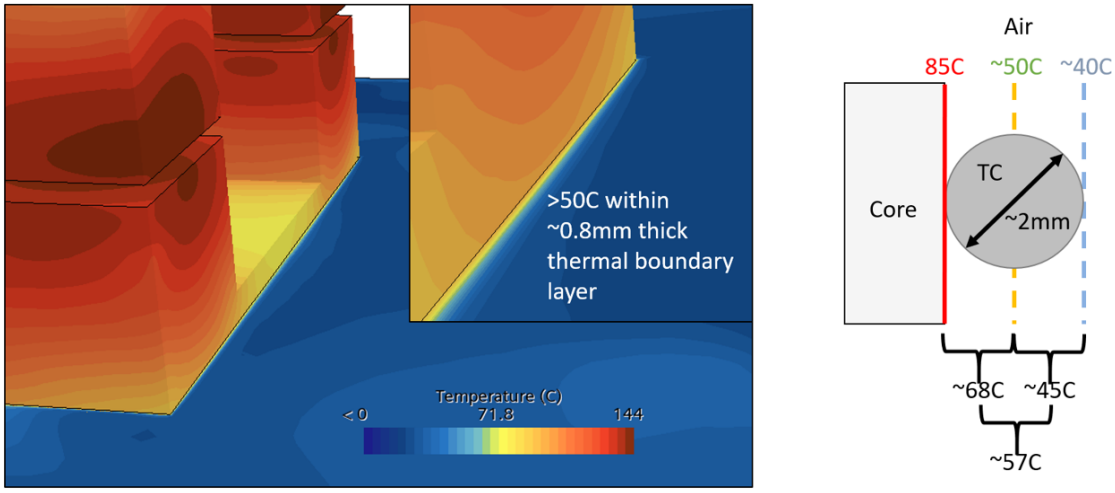

Figure 5.3: Correlation between experimental and simulation surface temperatures for median case (Ferrite k = 4.2 W/m-K, Core losses = 440 W).

5.2.3 iPEBB Airflow Reference Scenario

The established air-cooling model was then updated to better reflect the environment of the final iPEBB enclosure. Notably, the cold plate temperature was raised from 16°C to 30°C, the reference temperature pulled from past thermal modeling of the current iPEBB cold plate [5]. The previously used fan configuration and inlet air temperature were reused. In order to fully test the thermal limitations of air cooling, the established conservative

thermal conductivity of ferrite $k_{ferrite}$ = 3.5 W/m-K was once again applied to the core. The three loss scenarios outlined in Table 5.2 were simulated, with a summary of maximum temperature results shown in Table 5.4. A 2D cross-section view of temperatures in the driving design case can be seen in Figure 5.4.

Table 5.4: Airflow Reference Scenario Maximum Temperatures

Scenario	Temperature (°C)	
	Core Maximum	Coil Maximum
Open Circuit	190.1	76.8
Short Circuit	47.3	100.0
Combined Loads	193.3	119.9

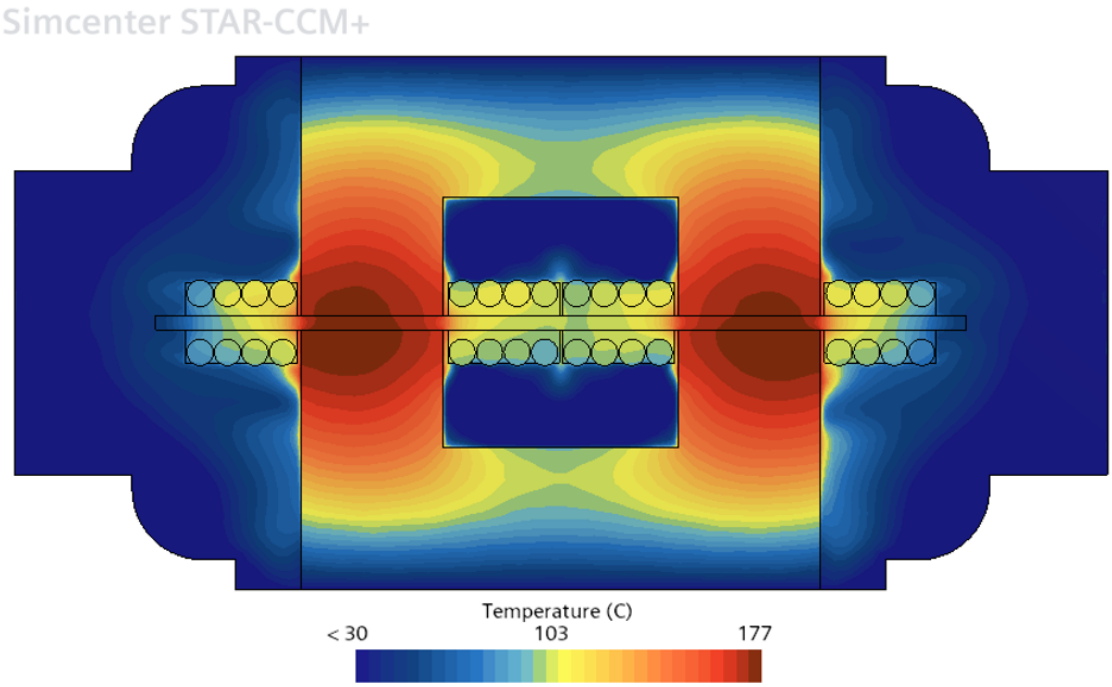

Figure 5.4: Cross-section temperatures for the Airflow Reference, combined loads scenario.

These results show that airflow cooling based on the experiment fan configuration is capable of cooling the coils under worst case operating conditions, however, fail to cool large regions of the core even with the presence of cold plates on either core outer surface. Sustained transformer operations at core temperatures exceeding 190°C as predicted by the model will increase the losses experienced by the system, reducing the capabilities of the iPEBB unit and possibly leading to a thermal runaway scenario. In addition, the airflow setup modeled would require the design and implementation of an entirely separate air distribution system, taking additional space within the iPEBB rack and introducing a potential vulnerability in the event of a fan failure. Based on the results of air cooling, a solution must be designed which simultaneously targets cooling at the upper regions of the core as well as manages the temperatures of the coils.

5.3 Heat Pipe Iteration 1

5.3.1 Design Solution

With the common substrate already serving as a heat sink thanks to the indirect liquid cooling provided by the cold plate, the idea emerged to utilize more of this cooled surface. By creating alternative paths for heat to travel from the core hot spots to the common substrate, maximum temperatures in the region could be decreased without the need for any additional heat sinks.

Heat pipes were explored for this use case due to their strong ability to move heat and proven reliability under extreme operating conditions. The initial concept utilizes 16 heat pipes embedded into aluminum heat spreaders, with each assembly mounted to move heat from the inner regions of the core to the common substrate. Of note is the addition of curved edges on the aluminum heat spreaders in an effort to reduce the intensity of peak electric fields that may occur at sharp metallic corners [39]. In order to extend this new heat sink to the coils, a ceramic heat spreader was designed to bridge the remaining distance while optimizing heat spreading and providing electrical insulation. An image of this concept can be seen in Figure 5.5.

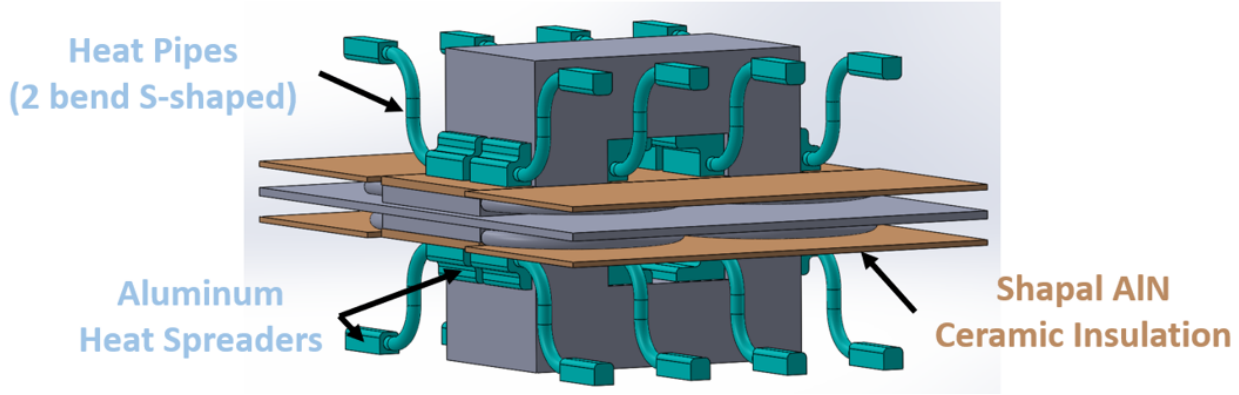

(a) Isometric view with key additions indicated.

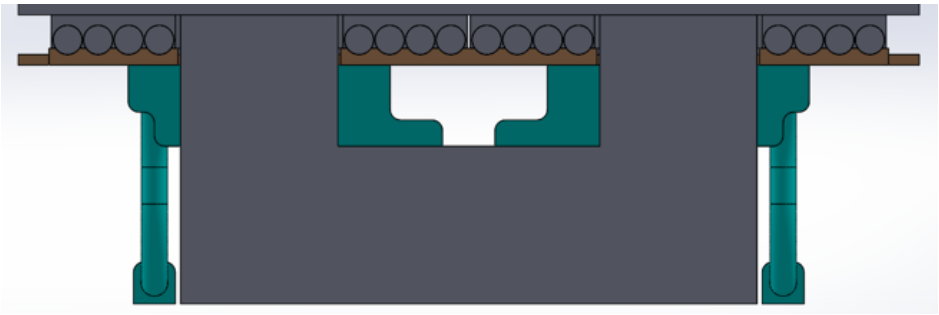

(b) Cross-section view of the transformer cooling setup.

Figure 5.5: iPEBB transformer with Heat Pipe cooling Iteration 1.

Initial heat pipe sizing was completed following an analytical method outlined by a well-known distributor, Advanced Cooling Technologies (ACT) [40]. The calculations are outlined

in Appendix C, which estimate the need for 16, 100 mm long, 5 mm diameter copper-water heat pipes. Visible in Figure 5.5, these heat pipes feature two 90° bends with a 15 mm bend radius. At both ends of the heat pipe, 20 mm of length are embedded into aluminum heat spreaders which are designed to maximize the contact area with both the heat sink and heat sources. For this initial design iteration, a basic rectangular prism shape was chosen with the intention of later optimizing for heat spreading and weight reduction. In addition to the embedded heat spreaders, two aluminum spreaders were also placed across the central gaps between core legs.

Serving as both the electrical insulation and heat spreading medium for the high frequency coils is the ceramic material Shapal HiM Soft Machinable Aluminum Nitride (AlN) [33]. In addition to possessing the strong electrical insulating properties characteristic of ceramic materials, this variant also has a relatively high thermal conductivity of $k_{ceramic} = 86$ W/m-K (interpolated at 100°C), enabling effective heat spreading from the heated coils. This material was chosen due to its ability to be machined, contrary to the brittle nature of typical ceramics and allowing for the design of custom profiles for better integration with the coils and heat pipes. The material's dielectric strength of 65 kV/mm means that only 2 mm of thickness provides insulation against up to 130 kV, meeting and exceeding the BIL test voltage for this transformer [3].

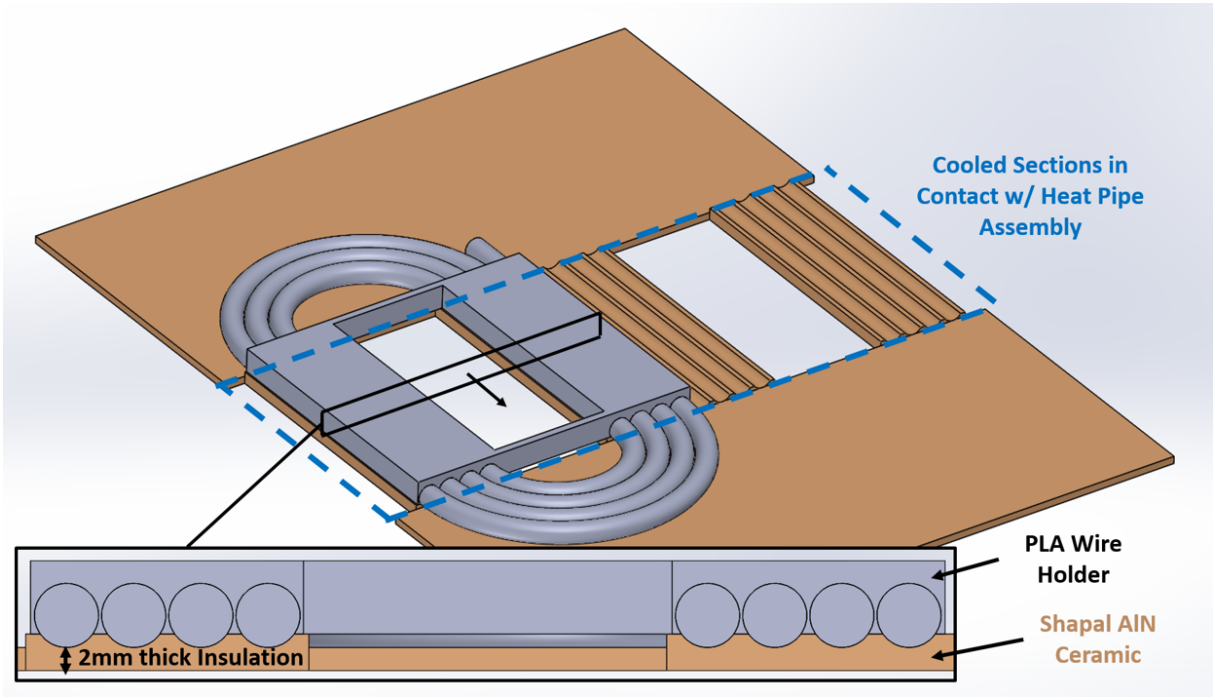

Figure 5.6: Transformer coil setup with ceramic insulation. Second set of coils are hidden to show the distinctions between ceramic sections.

A close-up of the ceramic design can be seen in Figure 5.6. The coil-facing surface has a curved profile to increase the area of contact with the coils, improving heat transfer between the two. Although effective, this feature also increases the cost to manufacture the component. In an attempt to balance performance with cost, only the sections of ceramic

aligned with the straightened sections of coil feature this profile, with the remaining ceramic pieces being planar sheets and serving only as electrical insulation. This trade off is feasible due to the alignment of the copper windings in the axial direction, which provides strong heat transfer along the length of the coils to what will be the cooled sections. Coil hot spots are therefore expected to appear in the curved sections furthest from the ceramic interfaces. Lastly, a 3D printed PLA plastic wire holder is used to secure the coils to the mica sheet due to its low weight, ease of manufacturing, and current usage in prototype iPEBB transformer setups.

5.3.2 Thermal Model

The heat pipe design iterations were simulated in StarCCM+ using similar modeling techniques as in the previous cases; however, all airflow was removed from the simulation domain. The resulting models eliminated convection cooling for the core and coils, requiring all heat to be transferred by conduction to the cold plate heat sink. Radiation was also neglected in these simulations. These assumption placed additional stress on the heat pipe solutions while removing the need for a fluid flow solver, greatly speeding up simulation times. Thermal epoxy were also assumed to be at the interfaces between the heat pipes, aluminum heat spreaders, and ceramic insulators. The only heat sink modeled was the cold plate surface, which is assumed to be at 30°C.

5.3.3 Thermal Results and Analysis

A summary of the maximum core and coil temperatures seen with this configuration can be found in Table 5.5. Highest temperatures in all three loss scenarios are well within design limits and showcase the successful extension of the cold plate heat sink. The use of aluminum heat spreaders effectively pulled heat from the upper regions of the core, as shown in Figure 5.7. Simultaneously, Figure 5.8 shows the successful managing of coil hot spot temperatures below their design limit of 155°C despite only the straightened sections of coil being in contact with the extended heat sink. These acceptable thermal results required the addition of only 0.75 kg of additional mass when accounting for the heat pipes, aluminum heat spreaders, and ceramic insulation pieces.

Table 5.5: Heat Pipe Iteration 1 Thermal Performance Summary. Note temperatures are well below limits of 100°C for the core and 155°C for the coils.

	Temperature (°C)	
Scenario	Core Maximum	Coil Maximum
Open Circuit	84.2	40.3
Short Circuit	36.6	79.0
Combined Loads	88.4	86.2
Total Added Weight		0.75 kg (1.66 lb)

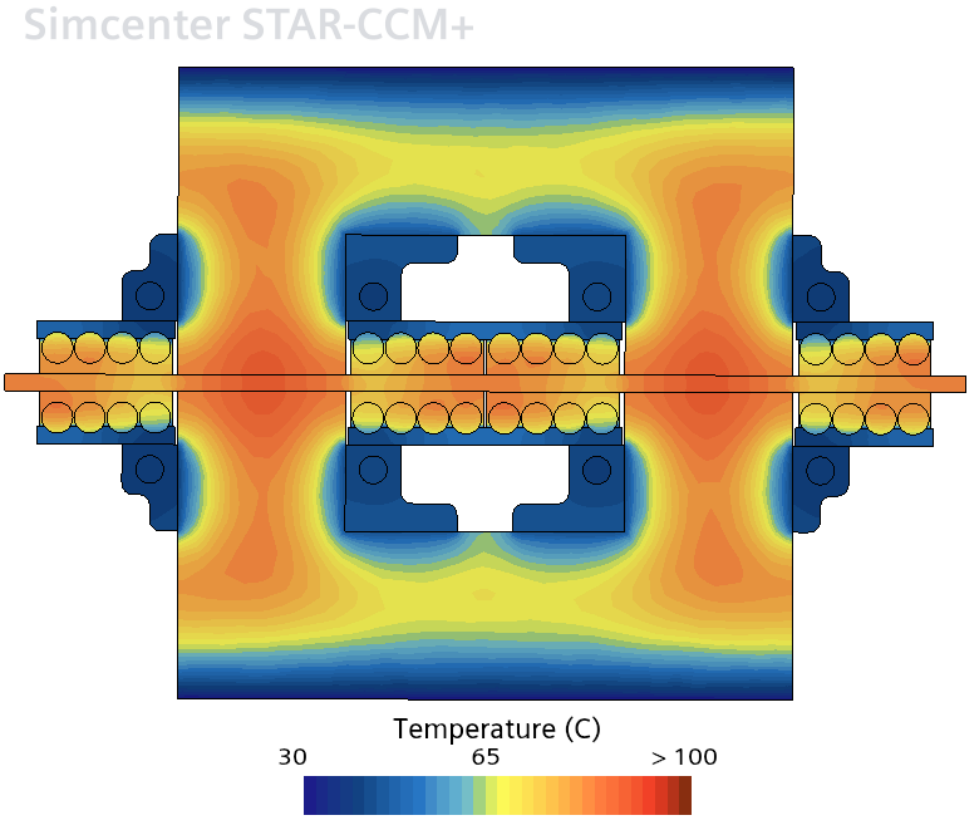

Figure 5.7: Cross-section temperatures for Heat Pipe iteration 1, combined loads scenario.

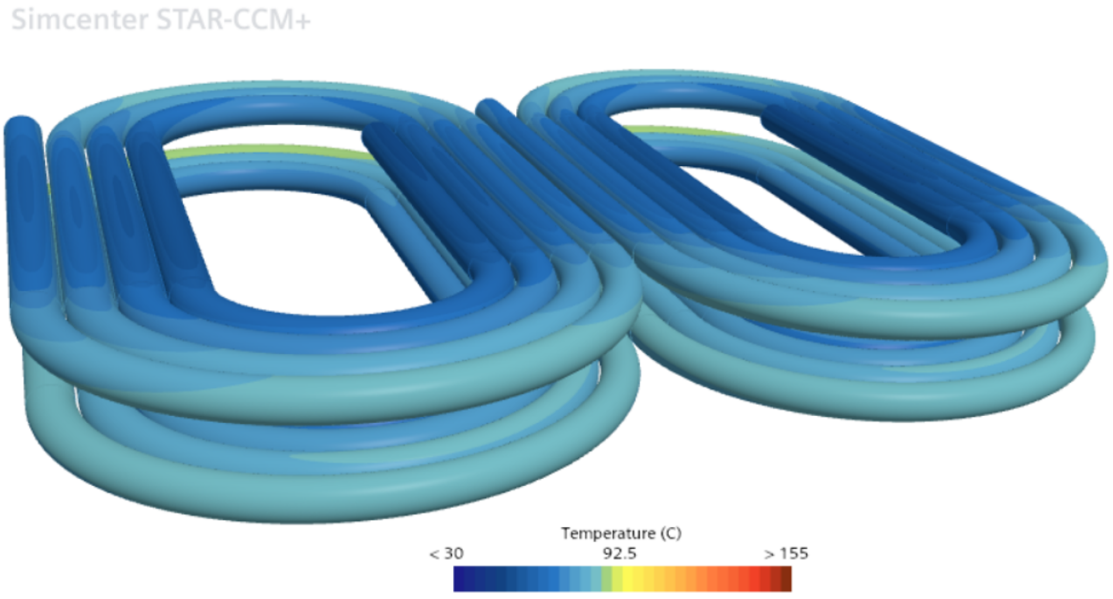

Figure 5.8: Coil surface temperatures for Heat Pipe Iteration 1, combined loads scenario.

5.4 Heat Pipe Iteration 2

5.4.1 Design Changes

With the first design providing the proof of concept, the next iteration was aimed at maintaining acceptable temperatures while also introducing the electromagnetic analysis. The geometry of this second iteration can be seen in Figure 5.9. The changes made are focused on the transformer-side heat spreaders, which were changed from aluminum blocks to AlN ceramic variants of similar geometry. With the transformer operating at high frequencies (430 kHz), the induced losses in any aluminum near the coils likely lead to significant heat generation, requiring a change in material. AlN ceramic acts as an electrical insulator in addition to its high voltage tolerance, and in a study by Wrobel et al. were experimentally proven to have negligible induced heat generation when near high frequency electronics [41]. Due to near-zero magnetic flux leakage at their current positions, the common substrate-side heat spreaders were left as aluminum.

The slightly higher density of this specific AlN compared to aluminum (2.88 g/cm^3 vs 2.7 g/cm^3) was compensated for by making slight reductions to the overall footprint of the new ceramic heat spreaders. Overall, this second iteration reduced the weight of the added hardware by 12 g, giving a new total mass estimate of 0.74 kg.

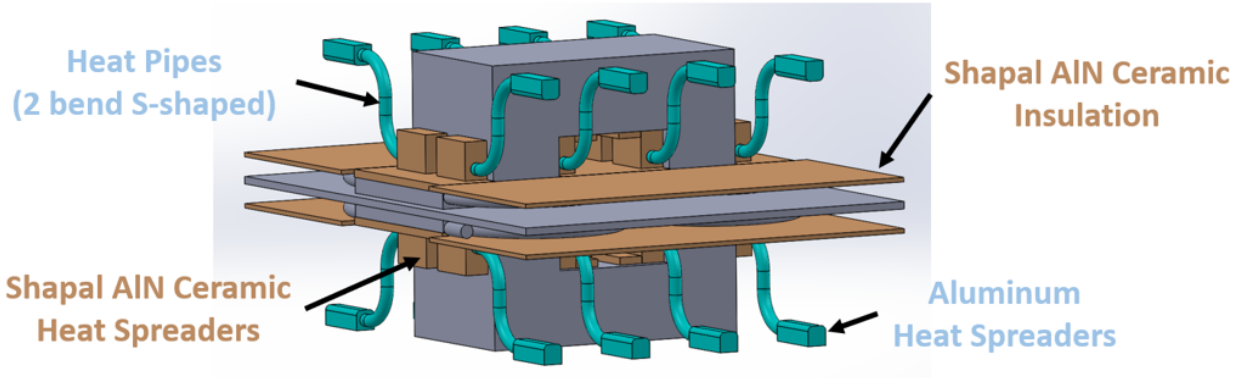

(a) Isometric view with key additions indicated.

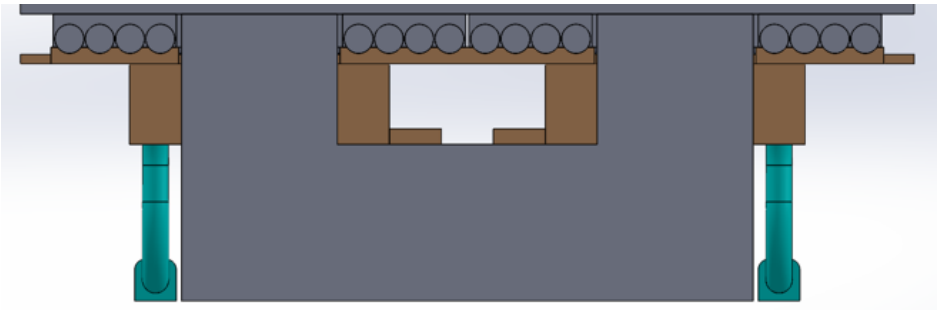

(b) Cross-section view of the transformer cooling setup.

Figure 5.9: iPEBB transformer with Heat Pipe cooling Iteration 2.

5.4.2 Thermal Simulation, Results and Analysis

Thermal simulations for the second design iteration were run using the same properties and conditions outlined for Heat Pipe Iteration 1 in Chapter 5.3. A summary of the maximum core and coil temperatures seen with this second configuration can be found in Table 5.6. Changing the heat spreaders from aluminum to ceramic AlN was found to not have a major effect on the thermal management of the core and coils, with hot spot temperatures still below maximum limits despite a 5°C increase in the case of the core. Figure 5.10 shows the resulting cross-sectional temperature distribution.

Table 5.6: Heat Pipe Iteration 2 Thermal Performance Summary

Scenario	Temperature (°C)	
	Core Maximum	Coil Maximum
Open Circuit	89.3	40.3
Short Circuit	36.8	80.2
Combined Loads	93.7	87.1
Total Added Weight		0.74 kg (1.63 lb)

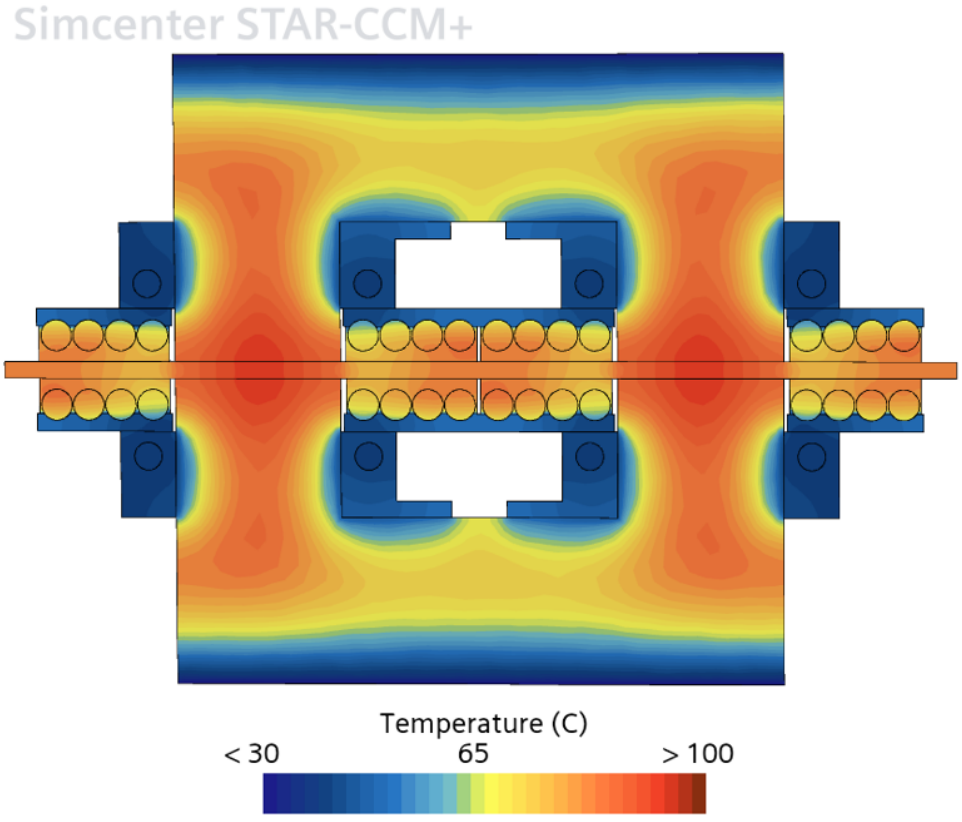

Figure 5.10: Cross-section temperatures for the Heat Pipe iteration 2, combined loads scenario.

5.4.3 Electromagnetic Analysis

Electrical analysis was focused on modeling the effects of high frequency coil operations on the copper-walled heat pipes. A quarter model of the iPEBB transformer with the proposed heat pipe configuration was built in StarCCM+ using the material properties in Table 5.7. With the exception of ferrite, the properties were based on the StarCCM+ local material database. Since the AlN ceramic is expected to have negligible heat losses, only the heat pipes were modeled.

Table 5.7: Electromagnetic Properties for the iPEBB Transformer/Heat Pipe Magnetic Analysis

Material	Electrical Conductivity (S/m)	Magnetic Permeability (H/m)
Air	$8.00*10^{-15}$	$1.26*10^{-6}$
Copper	$5.96*10^{7}$	$1.26*10^{-6}$
Ferrite 3F36	1.23 [7]	$2.01*10^{-3}$ [7]

An image of the model is shown in Figure 5.11. The coil winding was modeled as 4 separate concentric loops, with a total combined electrical resistance of $R_{coil} = 4.53*10^{-3}$ Ω. AC current through these coils was simulated at a magnitude of 45 A and at the current transformer design frequency of 430 kHz. The heat pipes were modeled as hollow due to the negligible heat generation through the internal working fluid. Since electrical currents are only generated in a thin layer at the surface, the heat pipe model and mesh were built to be one skin depth thick at 430 kHz, reducing the cross-sectional area and capturing the higher electrical resistance that will be present.

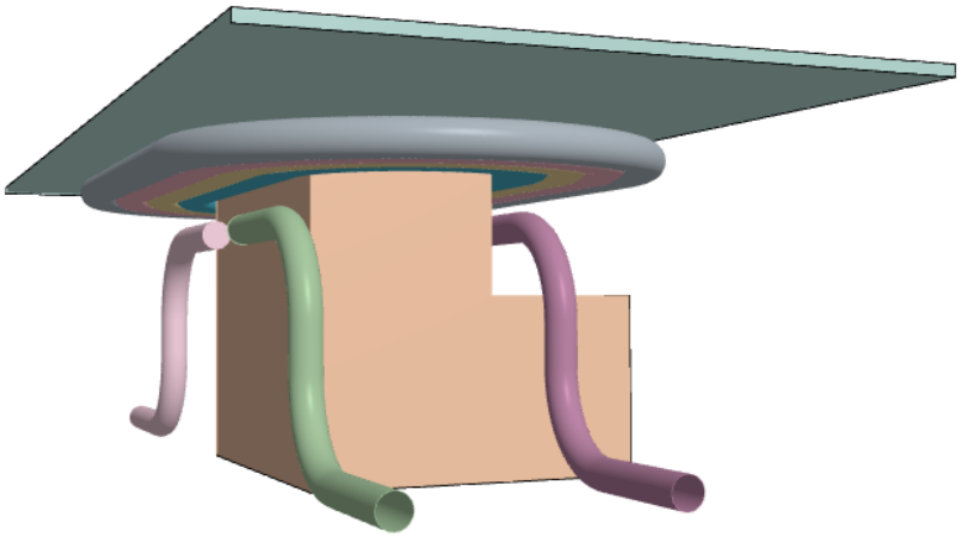

Figure 5.11: Quarter model of transformer Heat Pipe iteration 2 high frequency analysis.

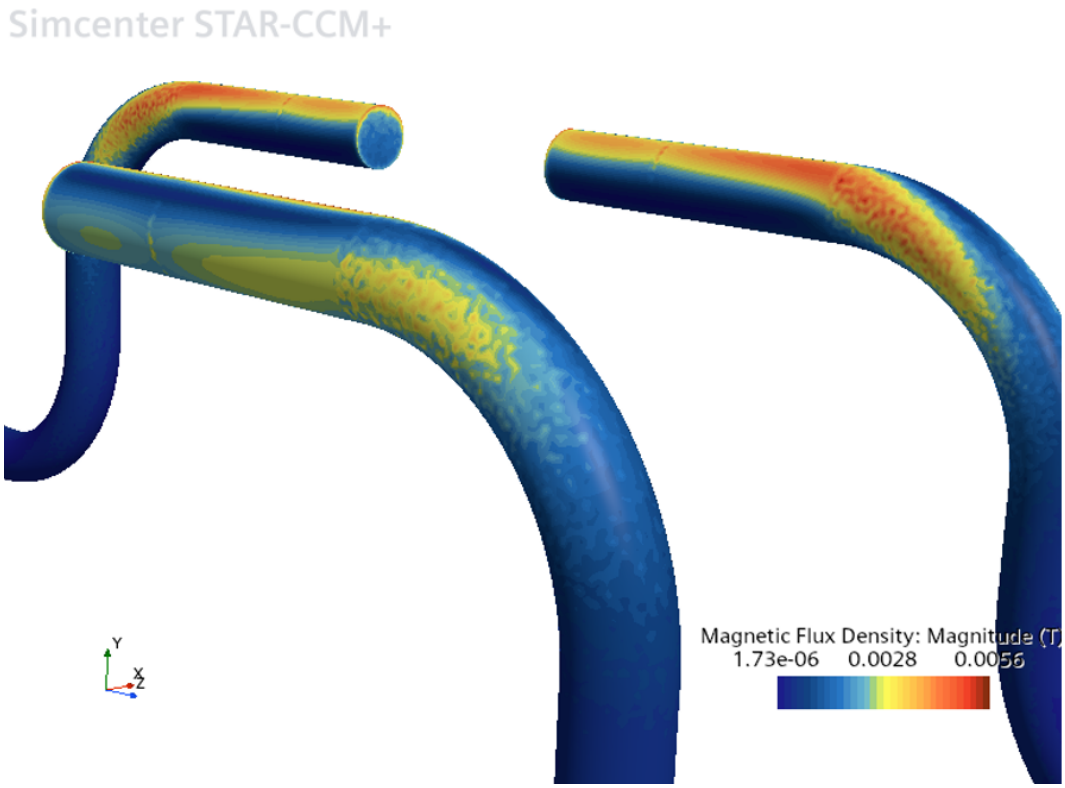

Figure 5.12: Magnetic flux at peak time step for 430 kHz operations of Heat Pipe iteration 2.

The transient run revealed maximum induced heat generation of 1.91 W per heat pipe for both the side and middle variants. When multiplied over the entire transformer, this results in 30.56 W of additional heat generation, nearly equivalent to an additional coil winding.

Table 5.8: Heat Pipe Iteration 2 Magnetic Performance Summary

Component	Peak Heat Generation (W)
S-shaped Side HP	1.91
S-shaped Middle HP	1.91
Total Transformer (x8 side HPs, x8 middle HPs)	30.56

In order to better analyze heat pipe losses in this configuration, the simulation was rerun for different transformer operational frequencies. For each run, the wall thickness of the heat pipe model was updated to match the respective skin depth at that frequency. Results of this study can be seen in Figure 5.13, and show a linear trend between the two parameters.

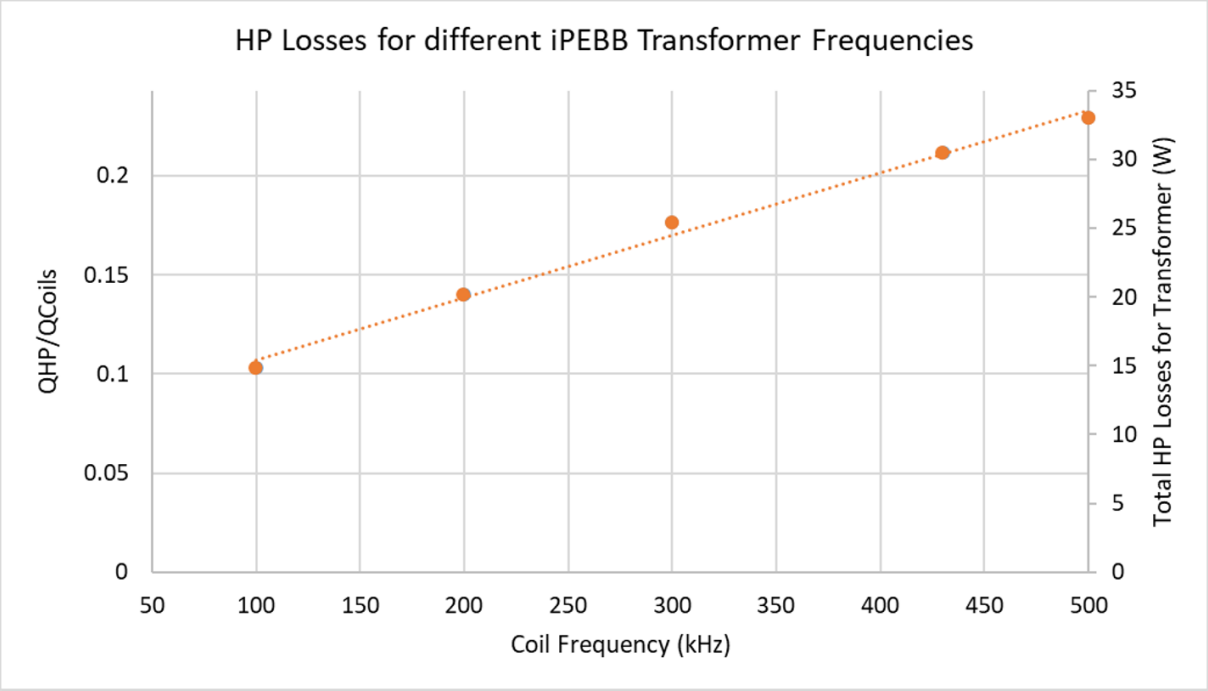

Figure 5.13: Heat pipe (HP) heat losses for S-shaped configuration at different iPEBB operational frequencies. Left axis shows the ratio of induced HP losses to coil losses.

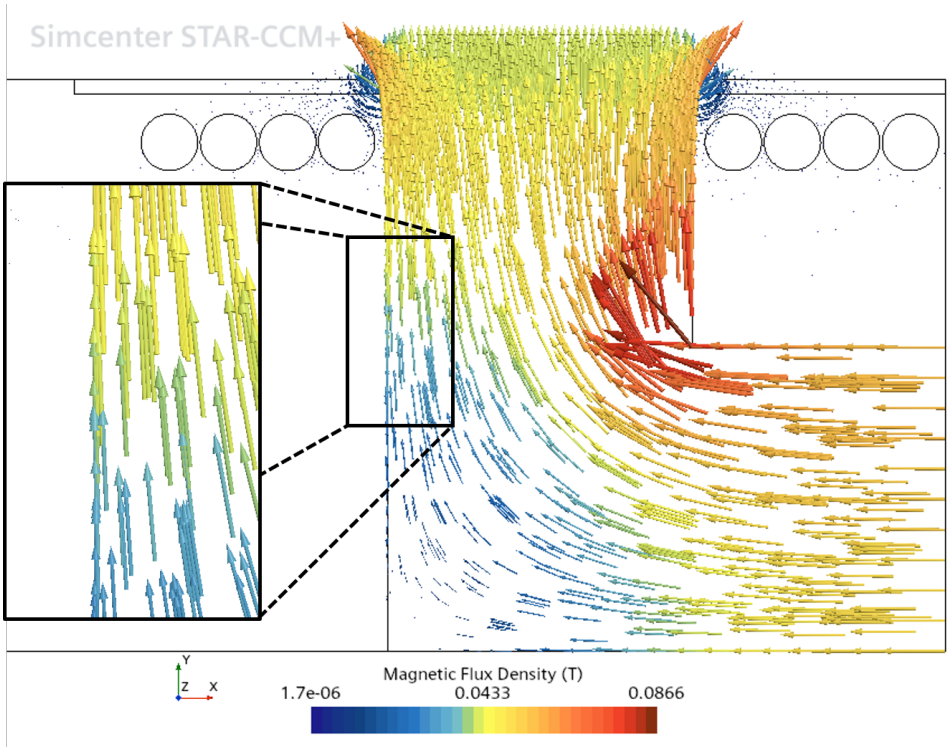

Figure 5.14: Core magnetic flux field for a given time step from the quarter transformer model. Field is nearly vertical at the core wall.

5.5 Heat Pipe Iteration 3

5.5.1 Design Changes

The next design explored adjusting the orientation of the heat pipes to better align with the direction of the local magnetic field, with the aim of reducing heat pipe magnetic flux and generated losses. The magnetic field follows the loop created by the two transformer core halves, with any flux leakage into the surrounding air running parallel to the outer core surface. The proposed geometry, as seen in Figure 5.15, replaced the 2-bend, S-shaped heat pipes with a 1-bend, L-shaped configuration that mostly parallels the core side surfaces. These shorter, 75 mm heat pipes replaced the previous 100 mm models while retaining the same diameter of 5 mm. The geometry of the core meant that the middle heat pipes had to be shifted to outside the central core gap, requiring larger ceramic heat spreaders. This resulted in an increase in heat spreader volume and subsequent weight, raising the total mass estimate of iteration 3 to 0.77 kg. The side mounted heat pipes were able to remain in roughly the same location as iteration 2, with the ceramic heat spreaders modified slightly to retain a similar footprint.

This configuration offers the advantage of reducing the number of heat pipe bends required and allowing for the usage of shorter variants, both of which increase the heat capacity of the heat pipes. A side-by-side comparison of the two heat pipe options for the middle region can be seen in Figure 5.16.

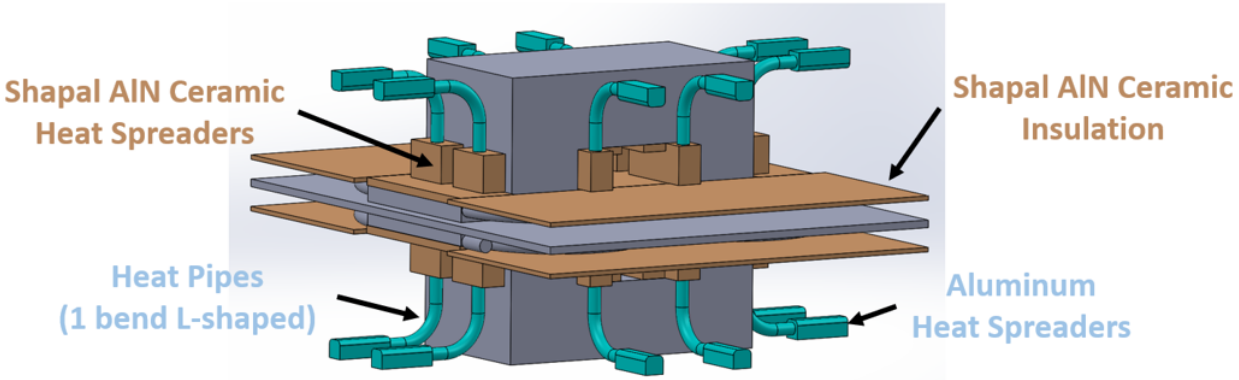

(a) Isometric view with key additions indicated.

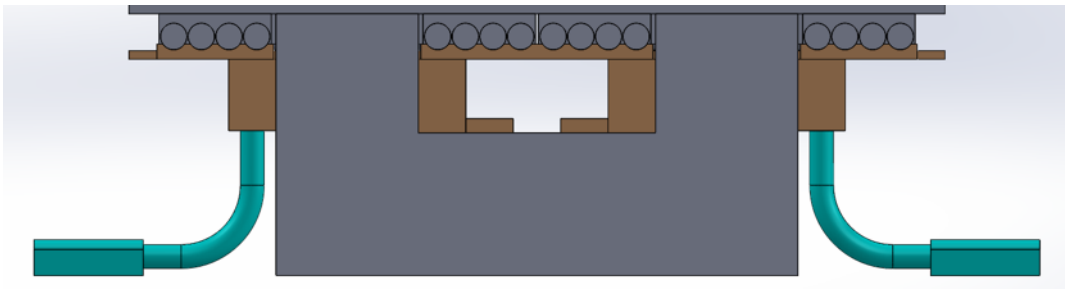

(b) Cross-section view of the transformer cooling setup.

Figure 5.15: iPEBB transformer with Heat Pipe cooling Iteration 3.

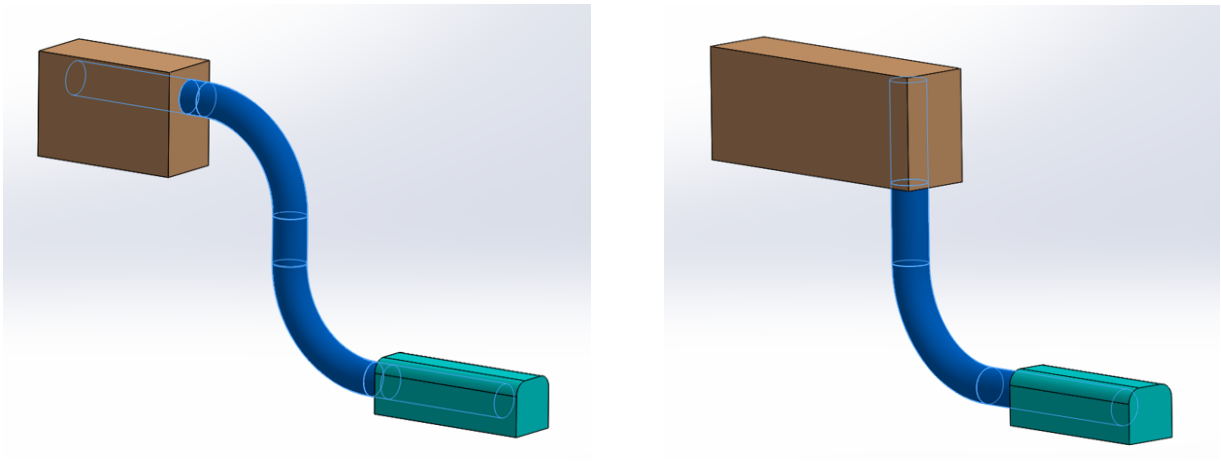

(a) S-shaped 2-bend heat pipe from iteration 2. (b) L-shaped 1-bend heat pipe from iteration 3.

Figure 5.16: Comparison of S-shaped and L-shaped middle heat pipes.

5.5.2 Thermal Simulation, Results and Analysis

Replacing the aluminum spreaders with a ceramic of lower thermal conductivity was expected to slightly increase hot spot temperatures across the core; however, the largest impact was caused by the repositioning of the middle heat pipes outside of the core gap. As seen in Figure 5.17, the removal of the middle heat pipes from their previously close location next to the core surface significantly raised the temperatures at that interface, reducing the effectiveness of the added heat sink. As a result, hot spot temperatures increased, with those of the core reaching just above the 100°C limit. In addition to the reduced thermal performance, the stretching of the middle ceramic spreaders also raised the weight of this configuration to 0.77 kg, the heaviest of the currently explored designs.

Table 5.9: Heat Pipe Iteration 3 Thermal Performance Summary

	Temperature (°C)	
Scenario	Core Maximum	Coil Maximum
Open Circuit	95.0	49.3
Short Circuit	40.8	82.6
Combined Loads	102.3	95.8
Total Added Weight		0.77 kg (1.71 lb)

5.5.3 Electromagnetic Analysis

The high frequency analysis of the heat pipe configuration followed the same setup and approach of iteration 2, with the updated model shown in Figure 5.18. This iteration's heat pipe positioning and orientation was selected with the goal of minimizing magnetic flux through the heat pipes while still retaining effective cooling.

At 430 kHz, this run revealed maximum induced heat generations well below those of iteration 2, with the side heat pipes seeing the largest decrease from 1.91 W to 0.37 W

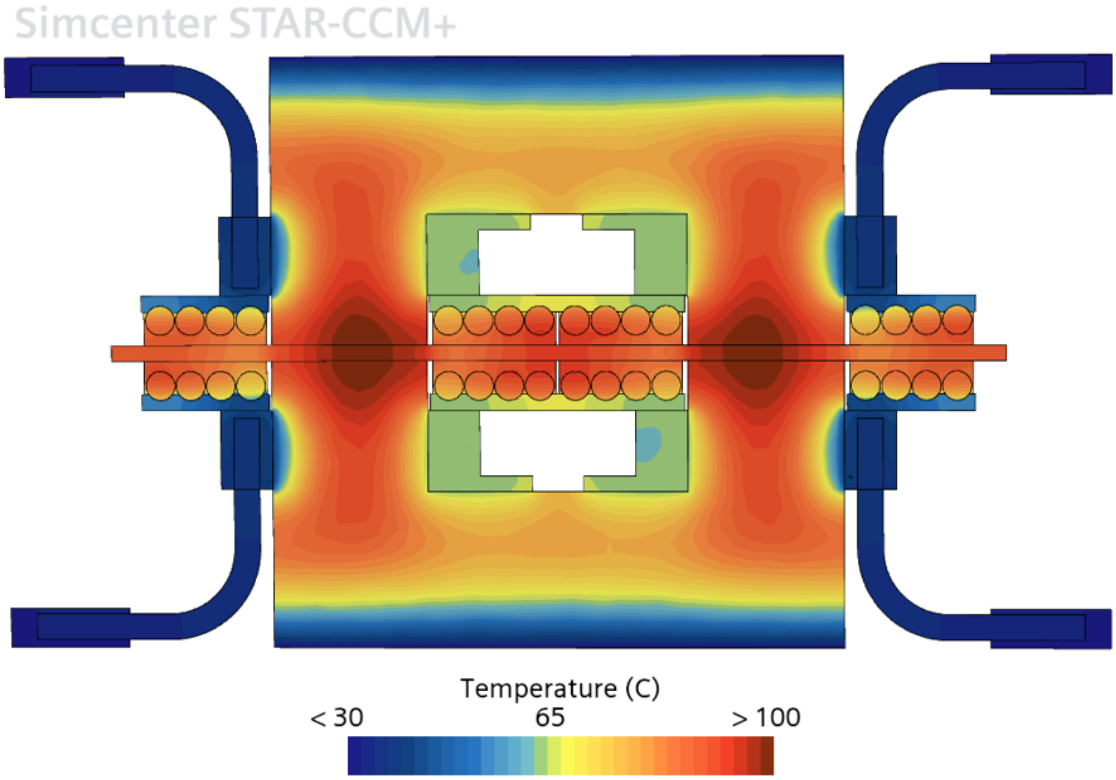

Figure 5.17: Cross-section temperatures for the Heat Pipe iteration 3, combined loads scenario.

per heat pipe. Although lower than in iteration 2, the middle L-shaped heat pipes still experienced approximately 0.80 W per heat pipe, giving a configuration transformer total of 9.36 W.

Table 5.10: Heat Pipe Iteration 3 Magnetic Performance Summary

Component	Peak Heat Generation (W)
L-shaped Side HP	0.37
L-shaped Middle HP	0.80
Total Transformer (x8 side HPs, x8 middle HPs)	9.36

Just as for the S-shaped heat pipe configuration, this simulation was rerun at different transformer operational frequencies. Again, the wall thickness of the heat pipe model was updated to match the respective skin depth at each frequency. Results for the dual L-shaped heat pipes can be seen in Figure 5.20, and again show a linear trend between the two parameters.

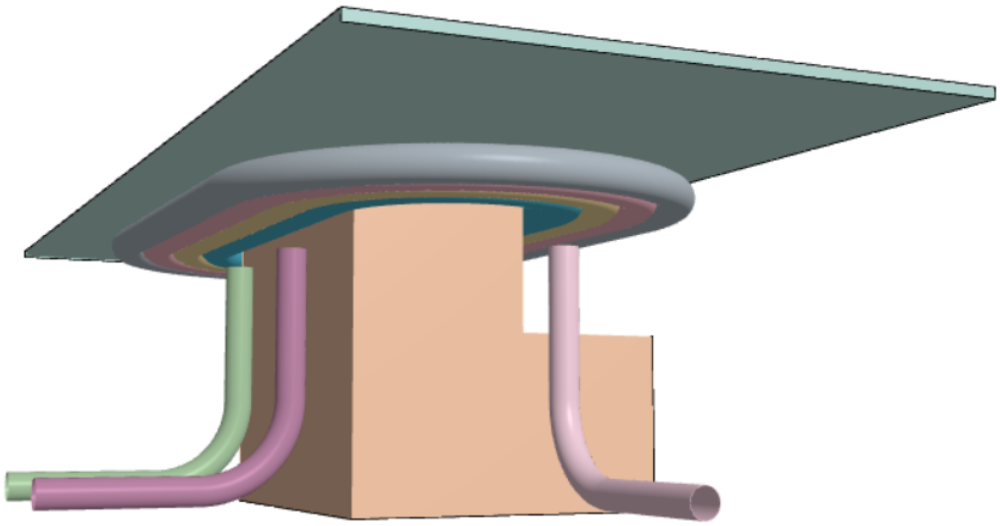

Figure 5.18: Quarter model of transformer Heat Pipe iteration 3 high frequency analysis.

Figure 5.19: Magnetic flux at peak time step for 430 kHz operations of Heat Pipe iteration 3.

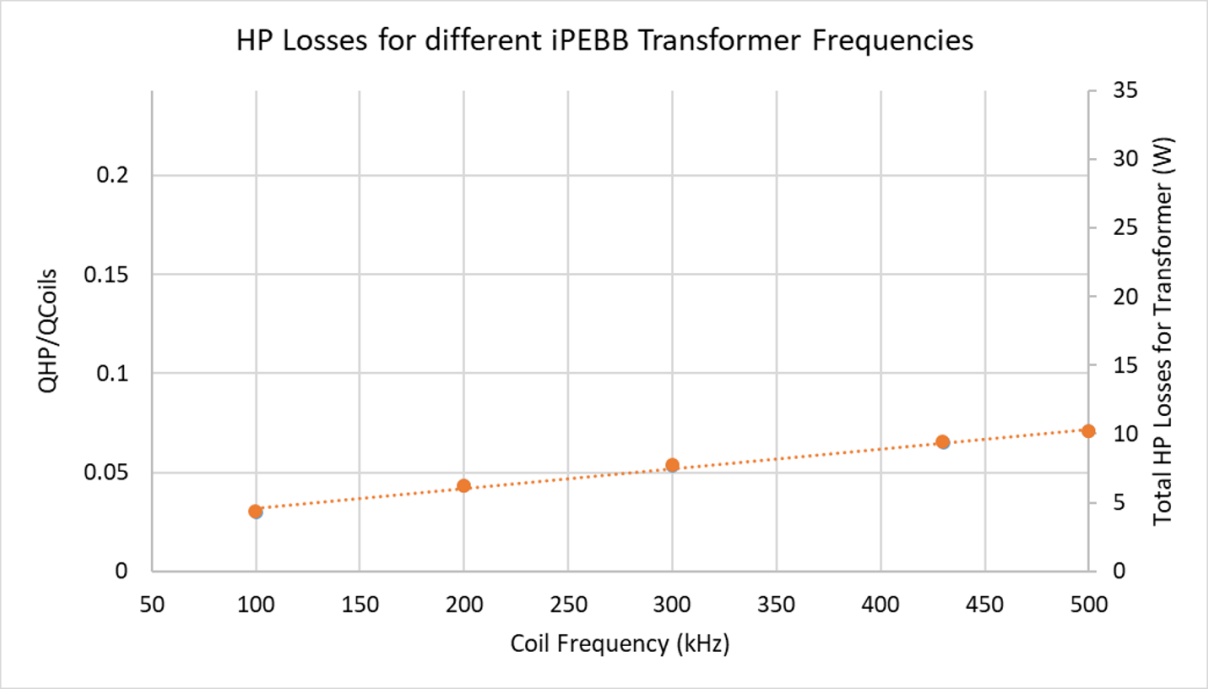

Figure 5.20: Heat pipe (HP) heat losses for L-shaped configuration at different iPEBB operational frequencies. Left axis shows the ratio of induced HP losses to coil losses.

5.6 Heat Pipe Final Iteration

5.6.1 Design Changes

The goal of the final iteration was to combine the advantages of iterations 2 and 3 in order to achieve acceptable thermal performance while minimizing the induced losses within the heat pipes due to high frequency operations. Although the S-shaped heat pipes experienced higher magnetic flux, and in turn higher induced losses, iteration 3 showed that removing these from the center opening of the transformer sacrificed core hot spot temperatures to the point of noncompliance. Furthermore, the use of S-shaped heat pipes in the middle gap reduced the size and weight of ceramic spreader required compared to the L-shaped variant. Therefore, it was decided to utilize the 100 mm long, S-shaped heat pipes in the middle gap in addition to 75 mm long, L-shaped heat pipes on the outer sides of the core. Previous results showed that substituting L-shaped heat pipes for the transformer sides reduced induced losses by 81% when compared to S-shaped heat pipes in this region without severely reducing heat transfer performance.

5.6.2 Thermal Simulation, Results and Analysis

Simulation results showed that utilizing this hybrid heat pipe configuration restored the nearly symmetrical dual heat sinks on either side of the core pillars. As shown in Figure 5.22, restoring the S-shaped heat pipes in the central gap helped reduce core hot spots located near the mica sheet back below the 100°C limit in the combined loads scenario. In addition,

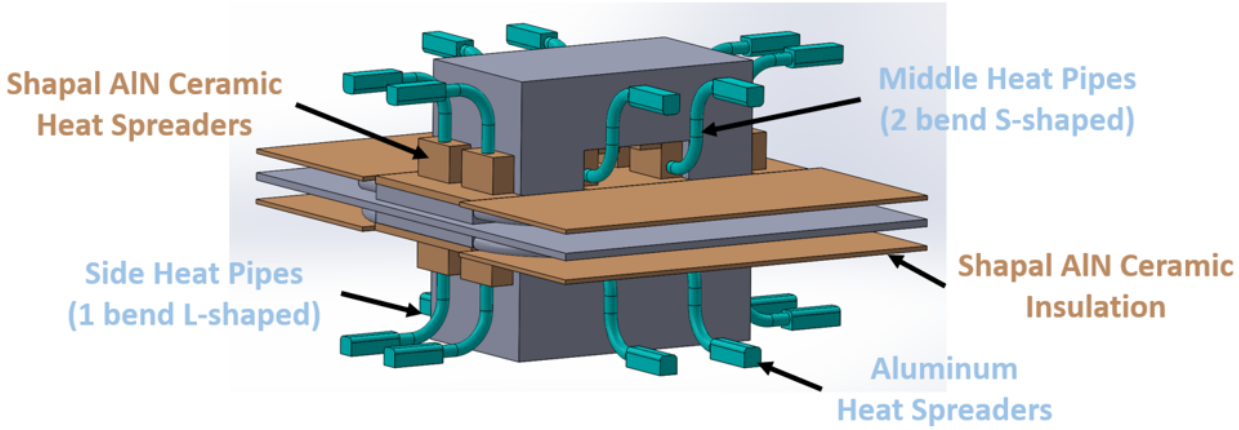

(a) Isometric view with key additions indicated.

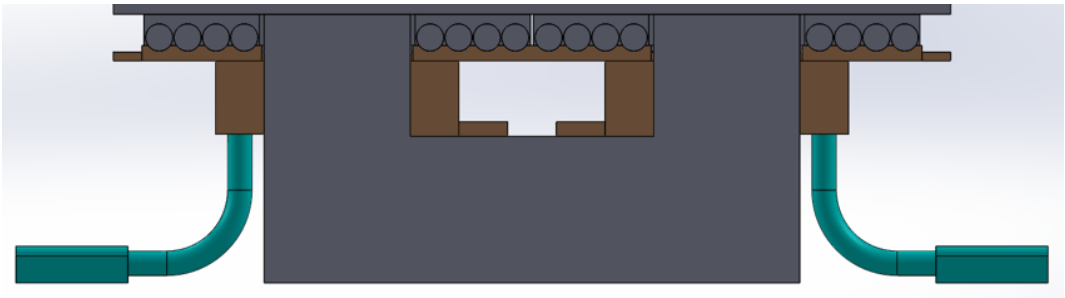

(b) Cross-section view of the transformer cooling setup.

Figure 5.21: iPEBB transformer with the final Heat Pipe Iteration.

replacing the relatively large ceramic heat spreaders of the L-shaped middle heat pipes reduced the total weight of the configuration to just 0.73 kg.

Table 5.11: Heat Pipe Final Iteration Thermal Performance Summary

Scenario	Temperature (°C)	
	Core Maximum	Coil Maximum
Open Circuit	89.7	42.2
Short Circuit	37.3	81.0
Combined Loads	94.4	88.2
Total Added Weight		0.73 kg (1.61 lb)

5.6.3 Induced Losses

With this configuration being a hybrid of iterations 2 and 3, the relevant results from the previous electromagnetic studies were reused for the heat pipe positions and orientations chosen.

The standalone thermal model was then rerun with these estimated heat pipe induced losses added. All were modeled as volumetric heat sources and were localized on the sections

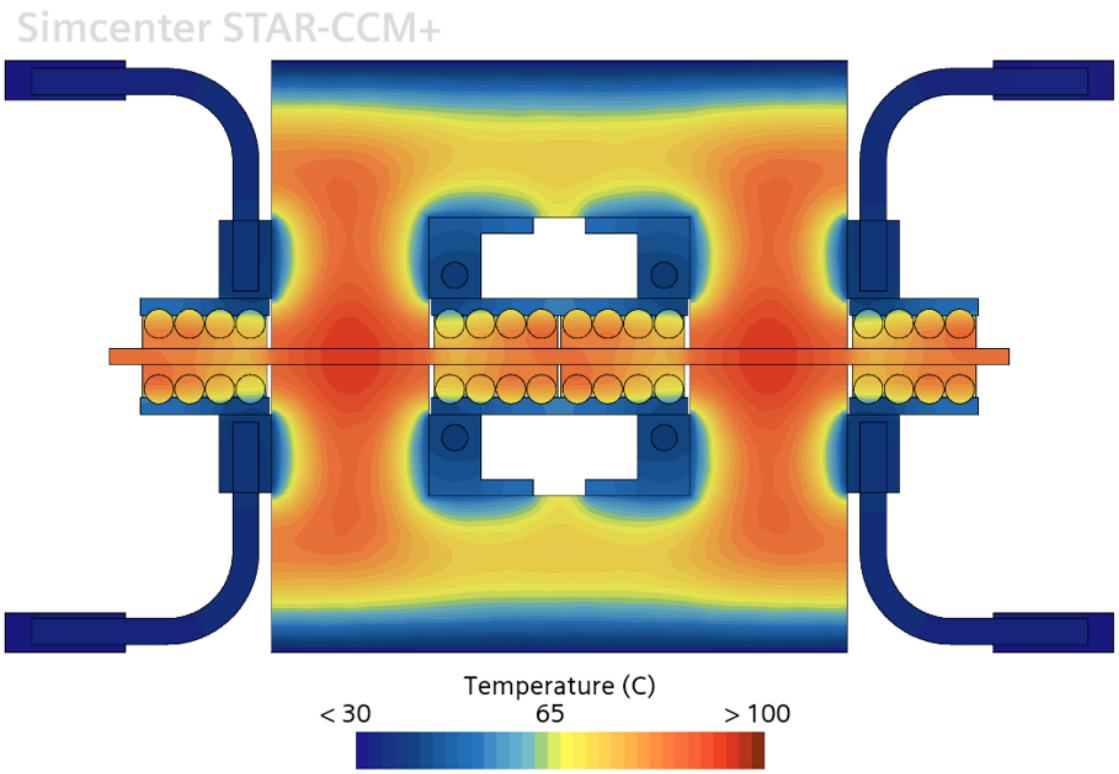

Figure 5.22: Cross-section temperatures for the Heat Pipe Final Iteration, combined loads scenario.

Table 5.12: Heat Pipe Final Iteration Magnetic Performance Summary

Component	Peak Heat Generation (W)
L-shaped Side HP	0.37
S-shaped Middle HP	1.91
Total Transformer (x8 side HPs, x8 middle HPs)	18.24

of heat pipe that saw the majority of the induced losses. These aligned roughly with the areas of heat pipe with high magnetic flux density seen in Figures 5.12 and 5.19. Heat flow values through each heat pipe are recorded for this final run in Table 5.13, alongside adjusted values Q_{max} which consider the roughly 5% reduction in heat transfer capability per 90° bend on each heat pipe as well as a 30% safety factor [42]. Even after applying these factors, the maximum heat loads do not exceed the heat pipe capacities calculated in Appendix E, which take into account pipe geometry and approximate operating temperature.

Heat pipes operate as near isothermal conductors, with the rate of vaporization and condensation of the working fluid naturally adjusting to maintain a constant temperature difference from hot end to cool end. This mean that, as long as the heat transferred does not exceed the maximum capacity, temperatures at either end of the heat pipe should remain unchanged for varying amounts of heat flow. In the case of the iPEBB transformer, this

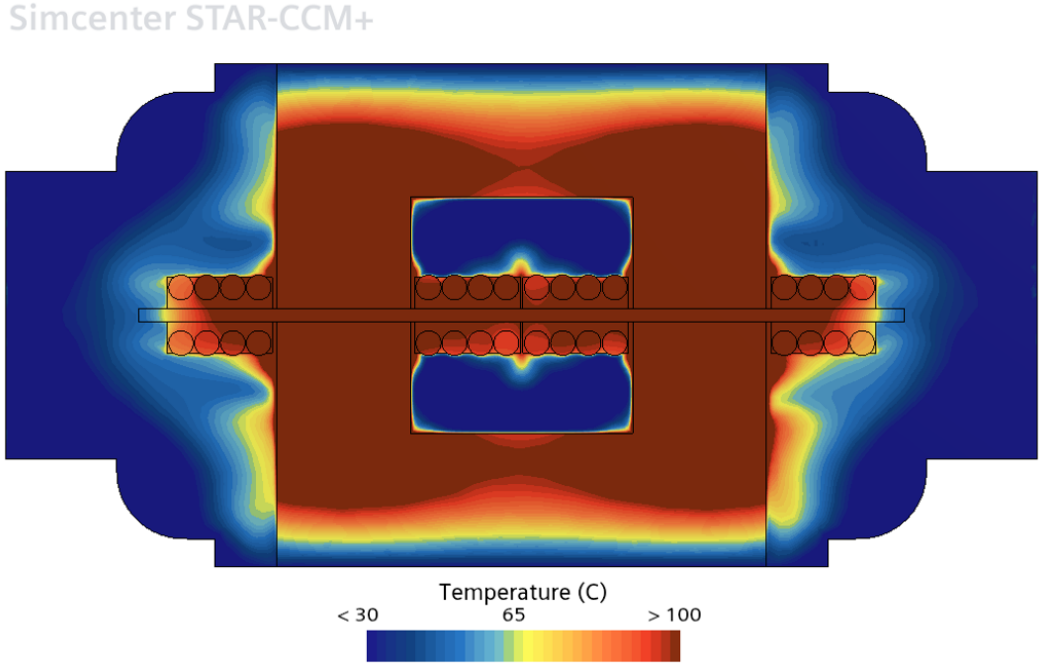

(a) Airflow Reference.

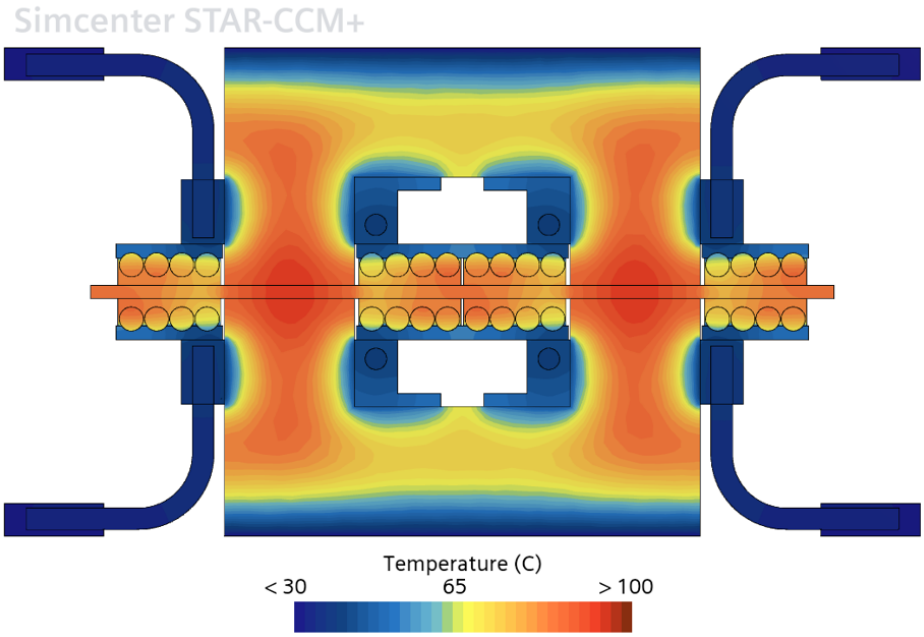

(b) Heat pipe final design.

Figure 5.23: Comparison of transformer temperatures under a) airflow cooling, and b) heat pipe final design cooling. Results shown are for the combined loads scenario and are normalized to the same range.

indicates that the thermal simulation results in Table 5.11 and Figure 5.22 hold even when considering the induced loads on each heat pipe.

Table 5.13: Final Iteration Heat Flow at 430 kHz AC Operations (with adjusted Q_{max} including 30% safety factor and bends)

	Component	(W) Q_{sim}	Q_{max}	Q_{max}/Capacity
Side HPs Capacity: 59 W	HP 1	21.3	28.8	0.488
	HP 2	21.2	28.6	0.484
	HP 3	21.6	29.2	0.495
	HP 4	21.5	29.1	0.493
	HP 5	21.6	29.2	0.495
	HP 6	21.5	29.1	0.493
	HP 7	21.2	28.6	0.485
	HP 8	21.3	28.8	0.488
Middle HPs Capacity: 44 W	HP 9	30.0	42.1	0.956
	HP 10	30.6	42.8	0.973
	HP 11	30.2	42.3	0.962
	HP 12	30.4	42.6	0.969
	HP 13	30.2	42.3	0.962
	HP 14	30.6	42.8	0.973
	HP 15	30.4	42.6	0.969
	HP 16	30.0	42.1	0.957

5.6.4 Coil Sensitivity Study

A sweep of the litz radial thermal conductivity value was performed in order to address the uncertainty from the litz experiments in Chapter 4 as well as test the robustness of the heat pipe configuration in cooling the coils. Results from varying the litz radial thermal conductivity component from 0.15 - 4.45 W/m-K in the combined loads scenario are shown in Figure 5.24. The results show that, across this wide range of possible radial thermal conductivity values, positive margin still exists between the coil maximum temperature and the design limit of 155°C. For our expected value of 1.31 W/m-K, over 60°C of margin is expected.

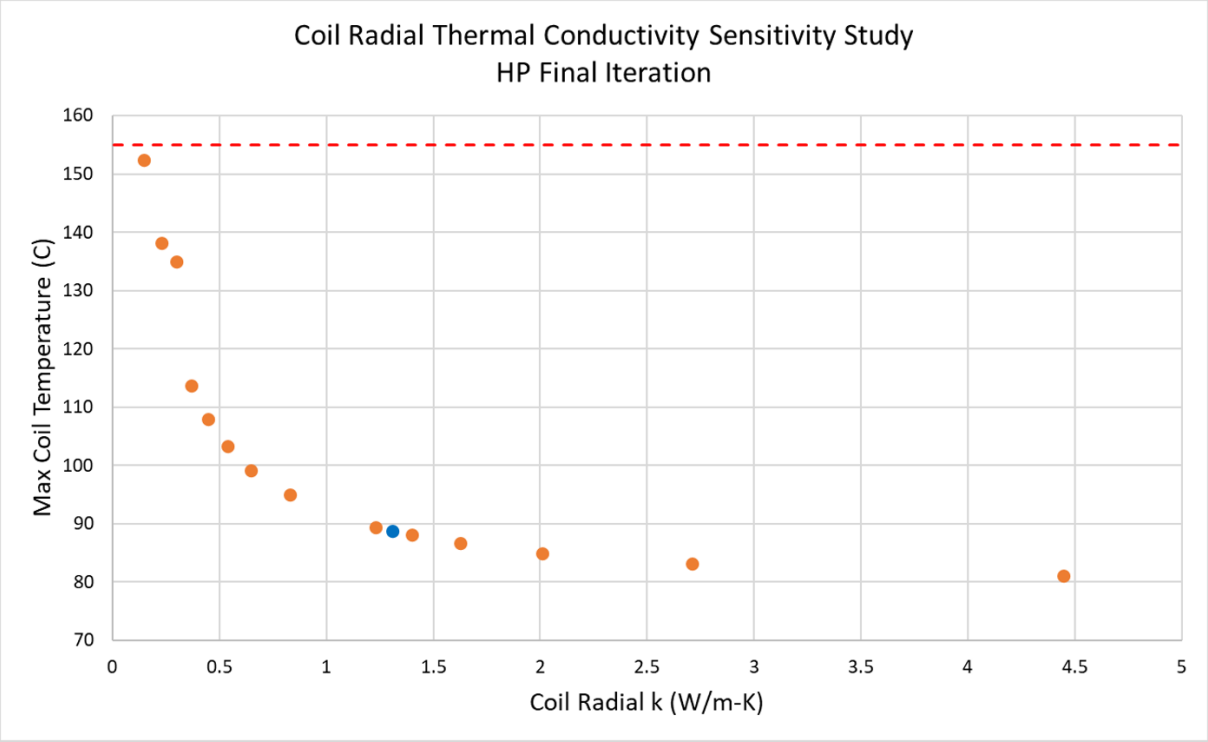

Figure 5.24: Maximum coil temperature for varied litz radial thermal conductivity values under the combined loads scenario (with heat pipe (HP) induced losses at 430 kHz). The red dashed line is the maximum allowed coil temperature (155°C), and the baseline result for a radial thermal conductivity value of 1.31 W/m-K is shown in blue.

Chapter 6

Final Design Half-iPEBB Simulation

6.1 Design and Thermal Model

A half-iPEBB thermal model was built in StarCCM+ using the common substrate and cold plate designs outlined in Chapter 2. Due to the symmetry of the iPEBB, a half model with an applied symmetry boundary condition allowed for the simulation of the whole iPEBB at a fraction of the computational cost. This model added the 100 W of heat generation per MOSFET in addition to the previously studied losses of the transformer. In addition to the cold plate, the final heat pipe cooling configuration from Chapter 5.6 was also included. A view of this model can be seen in Figure 6.1.

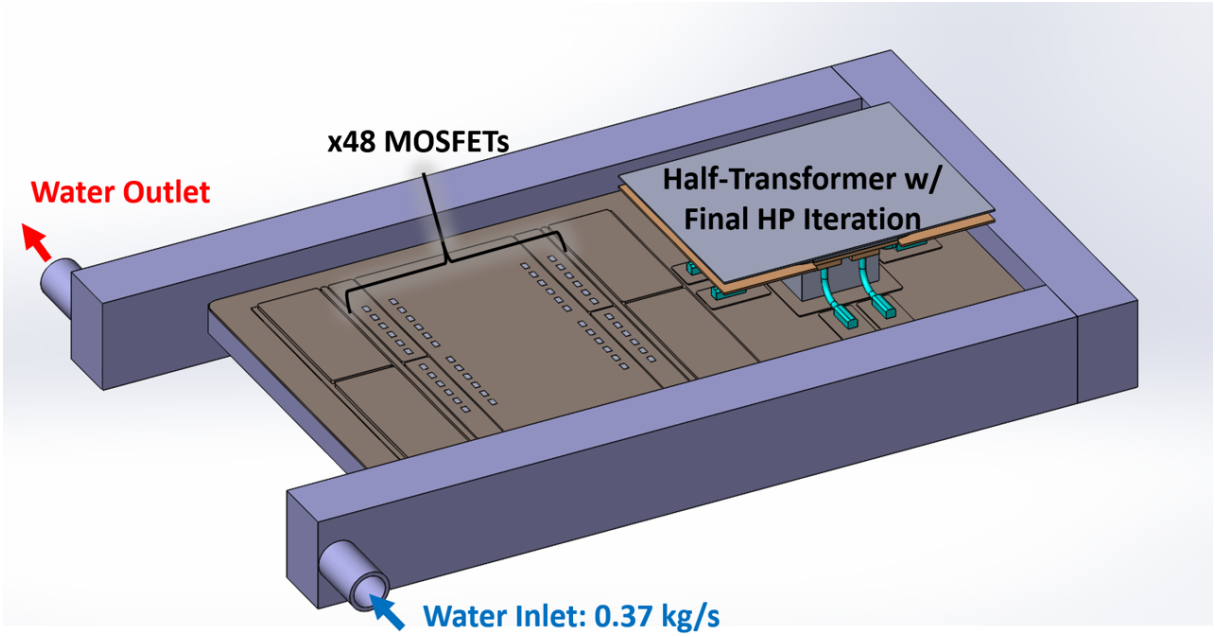

Figure 6.1: Half-iPEBB model with final transformer heat pipe design integrated.

In addition to the usage of ceramic heat spreaders, modifications were made to the common substrate to further prevent the creation of any electrical paths to ground from the transformer from the addition of heat pipes. As highlighted in Figure 6.2, the top

layer of copper under the transformer was sectioned in a similar approach to what was implemented on the MOSFET side of the iPEBB. This step serves as an extra precaution to ensure electrical insulation between any two heat pipe leg, as each copper island is currently directly mounted to a dielectric OBDC layer. The details regarding the exact design can be modified; however, the proposed configuration offers weight savings of 0.44 kg between both common substrates, offsetting the added weight of the heat pipe/ceramic solution to only have a net weight of 0.29 kg.

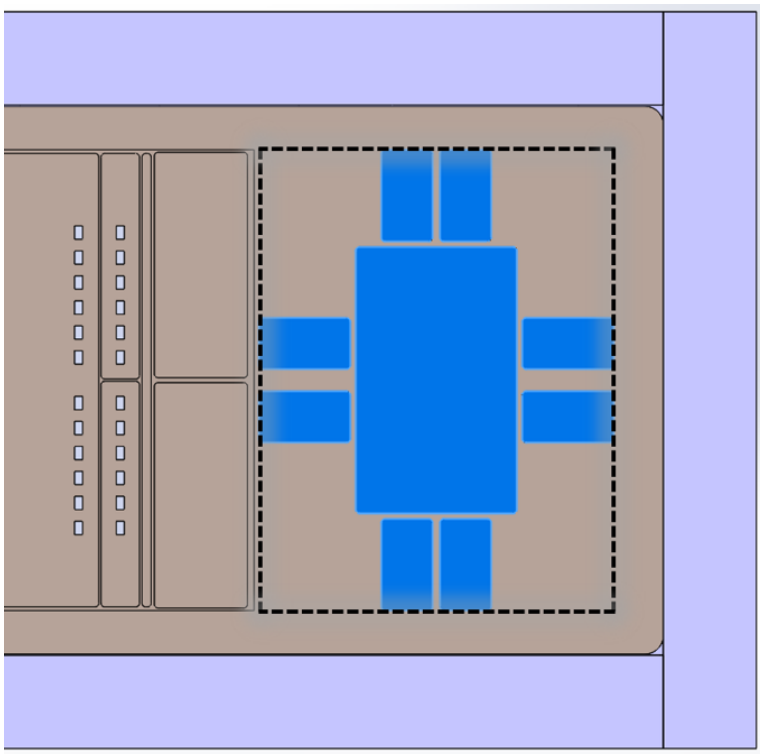

Figure 6.2: Proposed sectioning of top copper layer of the common substrate region where transformer is located. Sectioned areas (blue) are cut from the original square body, as shown by the black outline.

As in the standalone transformer models, the half-iPEBB model was built without any airflow present, removing convection cooling for the transformer and MOSFETs and forcing all heat to be removed by the proposed cooling hardware. Fluid flow through the cold plate was modeled using the expected baseline inlet water temperature of 22°C and mass flow rate of 0.370 kg/s [10]. This replaces the previously set boundary condition of a 30°C constant surface at the top layer of the common substrate.

Several new interfaces were modeled using an area-independent thermal resistance applied to their respective faces. For the MOSFETs, the effect of the sintered connection to the common substrate was captured using estimated properties of a 22% porous silver sample, with a thermal conductivity of k_{sinter} = 151.6 W/m-K and interface thickness of L_{sinter} = 48 μm [43].

$$R_{sinter}A = \frac{L_{sinter}}{k_{sinter}} = \frac{(4.80 * 10^{-5})\ m}{151.6\ W/mK} = 3.17 * 10^{-7}\ Km^2/W \tag{6.1}$$

The thin layers of OBDC sheets and the thermal interface material PGS were also modeled using an area-independent thermal resistance, rather than having their geometry physically represented. Using an effective interface resistance captured the thermal resistance through the layer without the need to mesh the thin surfaces, which would have added a large number of cells to the overall model. The capturing of heat spreading within these layers is also insignificant due to their poor thermal conductivites and extremely thin thicknesses. Using the known thicknesses (L_{OBDC}, L_{PGS}) and thermal conductivities (k_{OBDC}, k_{PGS}) of these layers gives the following values [4] [11].

$$R_{OBDC}A = \frac{L_{OBDC}}{k_{OBDC}} = \frac{(3.50 * 10^{-5})\ m}{0.7\ W/mK} = 5.00 * 10^{-5}\ Km^2/W \tag{6.2}$$

$$R_{PGS}A = \frac{L_{PGS}}{k_{PGS}} = \frac{(1.96 * 10^{-4})\ m}{1.38\ W/mK} = 1.42 * 10^{-4}\ Km^2/W \tag{6.3}$$

6.2 Thermal Results and Analysis

In addition to the baseline inlet water temperature of 22°C, the scenario where chilled water is utilized instead of deionized water was ran. Using a chilled loop would provide a cooler inlet water temperature of 7°C, however, would require the iPEBB to be fully electrically isolated, which is still being studied. Results from the two cases are listed in Table 6.1. In both cases, the temperature change seen between cold plate inlet and outlet ports was 3.3°C and the simulated pressure drop across the cold plate was 675.5 Pa.

Table 6.1: Half-iPEBB Final Heat Pipe Design Thermal Performance Summary

Cold Plate Inlet Water Temperature (°C)	Maximum Temperature (°C)		
	Core	Coils	MOSFETs
22.0	99.7	93.2	144.6
7.0	84.7	78.2	129.6
Net Added Weight			0.29 kg (0.63 lb)

Thermal steady-state results for 22°C inlet deionized water flow are shown in Figures 6.3a, 6.3b, and 6.4. Hot spot temperatures for the half-iPEBB model are approximately 5°C higher than the standalone model, which can possibly be attributed to the reduced heat spreading of the now trimmed common substrate top layer. Temperature gradients within and across the transformer are consistent, however, and reveal identical hot spot locations that still fall below the 100°C core and 155°C coil limits. Looking at the MOSFETs confirms heat overlap between subsequent MOSFET switches; however, temperature estimates confirm the effectiveness of the heat spreading provided by the common substrate design. Maximum MOSFET temperatures remain below the 150°C limit.

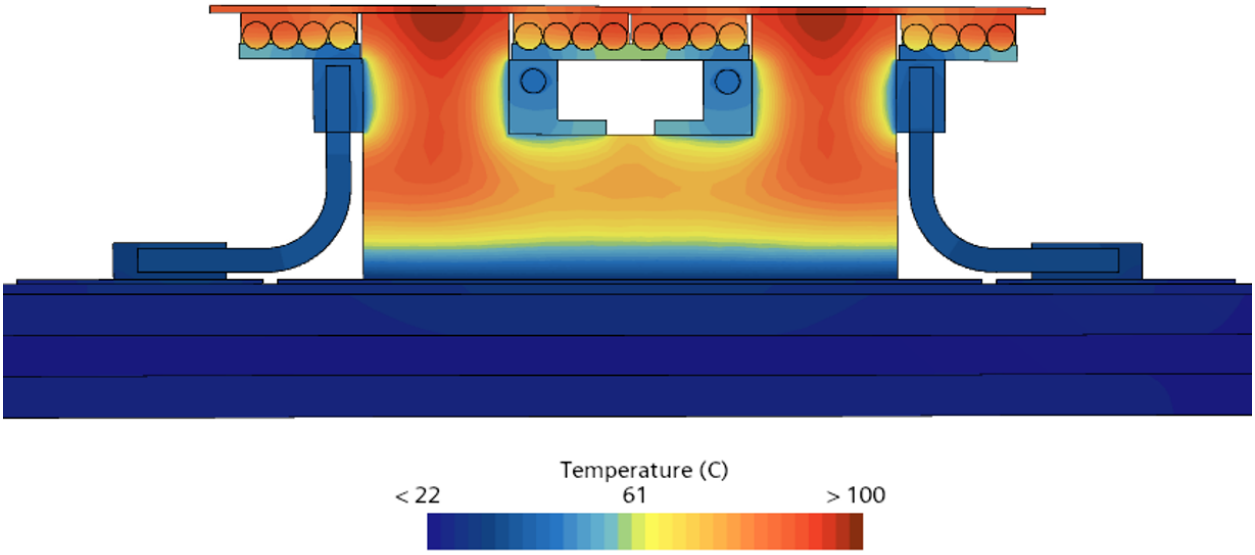

(a) Transformer cross-section temperatures.

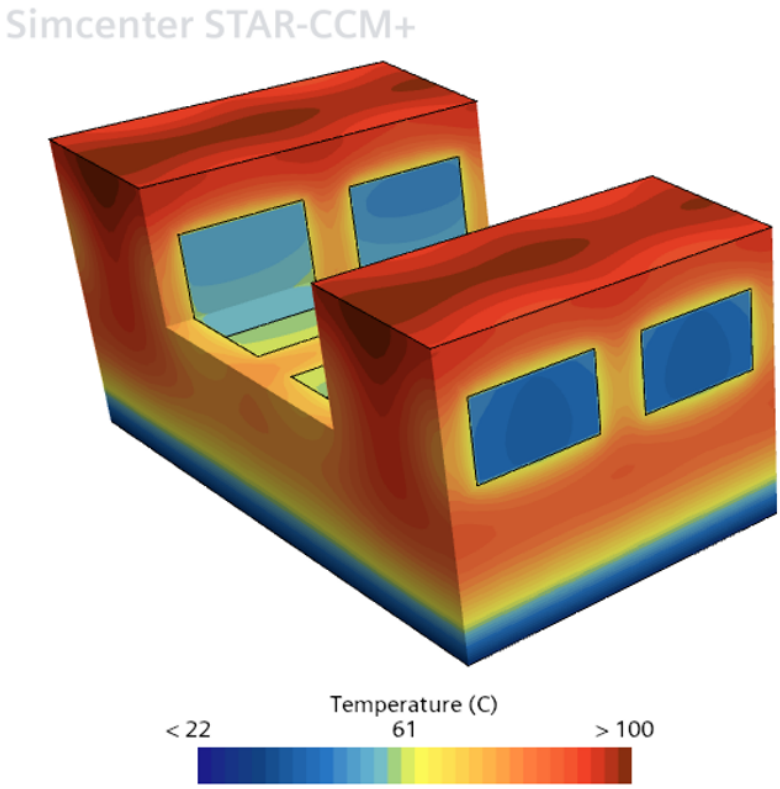

(b) Core surface temperatures.

Figure 6.3: Transformer temperatures for the half-iPEBB, final heat pipe model with the combined loads scenario. Results are at steady state and with an inlet water temperature of 22°C.

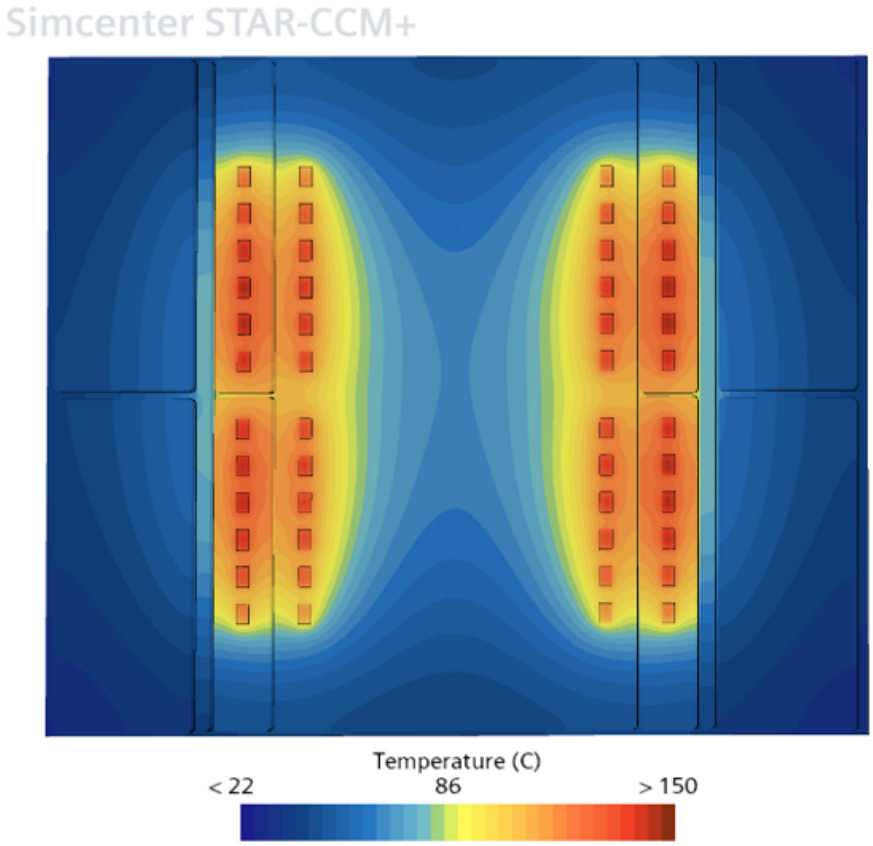

(a) MOSFET surface temperatures.

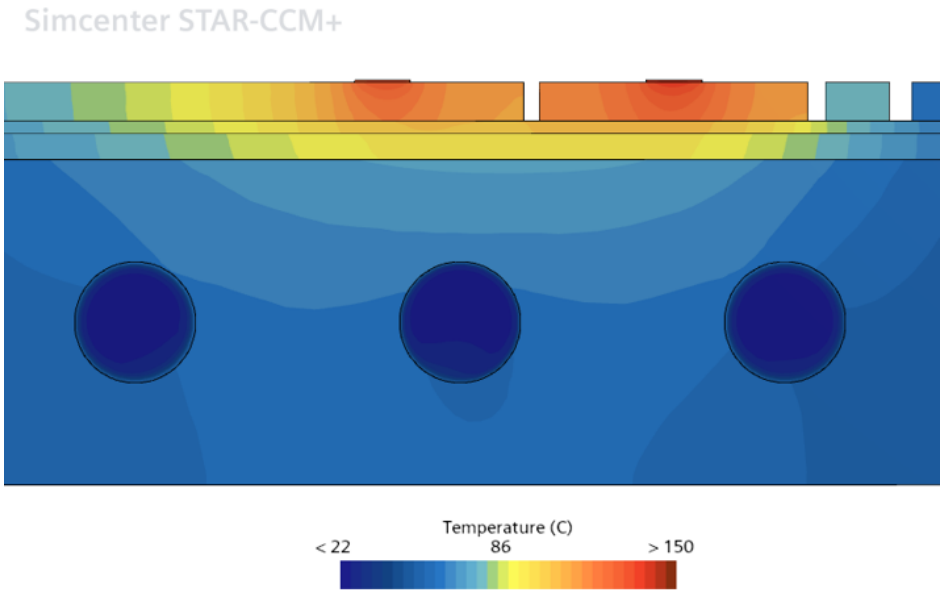

(b) MOSFET/half iPEBB cross section temperatures.

Figure 6.4: MOSFET temperatures for the half-iPEBB model, combined loads scenario. Results are at steady state and with an inlet water temperature of 22°C.

Chapter 7

Conclusions and Future Work

In this thesis, the usage of heat pipes to provide supplementary cooling to a high frequency transformer was studied and analyzed. First, experiments and analytical solutions were employed to better estimate the thermal conductivity values of two crucial heat generating components, the ferrite core and litz coils. Next, thermal models of the transformer were built in StarCCM+ and used to simulate worst-case loss scenarios under various cooling solutions. Airflow cooling was modeled based on available test data. Following a correlation of experimental and simulation results, the airflow model was used to provide baseline temperature results for the iPEBB transformer. Multiple heat pipe configurations were then modeled and used to provide a supplementary path for heat to flow from the hot spot regions of the transformer to the cooled common substrate. Electromagnetic simulations were used to model the impact of high frequency coil operations on the proposed heat pipe configurations. The final heat pipe configuration was then integrated into an iPEBB-level simulation with the cold plate fluid modeled. Results showed that the final heat pipe configuration was capable of maintaining transformer component temperatures below their acceptable limits, while not producing induced heat pipe losses exceeding their design heat load capacities.

The final design utilizes 16 heat pipes embedded in aluminum nitride ceramic heat spreaders on one end, which are directly mounted to the "legs" of the transformer core, and to aluminum heat spreaders on the other end, mounted to the common substrate surface. AlN ceramic fixtures are used to provide direct contact between these heat spreaders and the litz wire coils. The high voltage insulation of the transformer coils, minimization of high-frequency induced heat generation in the copper-walled heat pipes, and prevention of any additional loops of electric current flow between the transformer and ground were all considered and mitigated for in the design process.

Thermal simulations of the final design integrated with the iPEBB model predicted temperature hot spots of 99.7°C for the transformer core, 93.2°C for the transformer coils, and 144.6°for the MOSFET switches when cooled by a flow rate of 0.37 kg/s of deionized water at 22°C through the current cold plate design. All of these maximum temperatures fall within the temperature limits. For the MOSFETs, this includes a safety factor of 30°C. These results were attained for an iPEBB with a constant 9.6 kW of MOSFET losses across 96 switches, 480 W of transformer core losses, and 144 W of coil winding heat generation. The positioning of 2-bend, S-shaped heat pipes within the middle core gap and 1-bend, L-shaped heat pipes at the outer side surfaces resulted in within-limit heat flow values through

each component. Magnetically, simulations predicted an additional 18.24 W of heat generation across the 16 heat pipes due to the nearby magnetic flux leakage. Accounting for all transformer heat loads in addition to induced loads and a 30% safety factor, this results in a maximum load of 42.8 W through any heat pipe, which falls within capacity of the selected heat pipe size. Due to the isothermal behavior of heat pipes when operating under its maximum heat capacity, these induced losses did not affect the maximum temperatures predicted within the transformer. The proposed hardware was predicted to weigh 0.73 kg; however, with reductions to the current copper common substrate footprint, the net weight addition to the iPEBB was reduced to 0.29 kg.

These results, although promising, require further analysis for implementation in the iPEBB. Notably, experimental measurements of the induced heat pipe losses and resulting temperatures must be gathered at the target design frequency in order to validate simulation predictions. Various conservative assumptions were made throughout the modeling process in order to reduce the risk of the final results; however, with more accurate material properties, the design can likely be optimized for further weight and temperature reductions. The use of Shapal HiM Soft Machinable AlN ceramic was crucial to the design of the proposed solution; however, it must be noted that this is currently a custom-made material, and may prove expensive for usage across thousands of iPEBBs as needed by the Navy.

Ultimately, future design changes for the iPEBB transformer will require a redesign and analysis of the cooling solution regardless of approach; however, the findings of this paper can show the thermal feasibility for the usage of heat pipes in cooling high frequency electronics.

Future redesigns of the transformer could explore the impregnation of the litz coils with an epoxy filler to increase the heat transfer capability of the wires compared to the currently air-filled samples. Based on current results, however, this would add unnecessary weight via epoxy as the current coil temperature predictions are approximately 50°C below the limit. Another common solution is the potting of coils in an epoxy mixture for insulation and heat spreading purposes, however the low thermal conductivity and high density when compared to AlN ceramic makes this approach impractical given the weight it would require.

Shortening the core to reduce the distance to the common substrate would also help with the reduction of core hot spot temperatures. This change would also place the coils closer to the common substrate, reducing the need for heat pipes and opening up coil potting as another possible solution.

As for the heat pipes, there are various steps that can be taken to reduce the impacts of high frequency operations. Based off similar heat pipe experiments and modeling by Wrobel [24], switching the copper-walled heat pipes to titanium-walled variants could reduce the effects of the magnetic field by an order of magnitude. In the future, a possible solution could be the usage of ceramic-walled heat pipes, which could render the impacts of induced losses negligible. Research of this technology is ongoing, with heat pipe manufacturer ACT receiving a multi-million dollar grant in late 2023 from the U.S. Department of Energy for the development of this exact concept for usage in transformer cooling [44].

The usage of heat pipes proposed in this paper succeeds in cooling the iPEBB transformer while addressing high frequency concerns posed by the coil operations with minimal added weight. Heat pipe cooling for transformers has the potential to remove the current thermal limitations for power electronics designs, opening up new capabilities for Naval iPEBBs, electric vehicle charging, and more.

References

[1] L. Petersen, C. Schegan, T. S. . Ericsen, *et al.*, "Power Electronic Power Distribution Systems (PEPDS) - Plan," *ESRDC Website, www.esrdc.com*, 2022.

[2] N. Rajagopal, "Design of 1.7 kV SiC MOSFET Switching Cells for Integrated Power Electronics Building Block (iPEBB)," Master's thesis, Virginia Polytechnic Institute and State University, Blacksburg, VA, 2021.

[3] S. Sharfeldden, "Design of a 405/430 kHz, 100 kW Transformer with Medium Voltage Insulation Sheets," Master's thesis, Virginia Polytechnic Institute and State University, Blacksburg, VA, 2023.

[4] C. DiMarino, "ONR Power Electronics Power Distribution System (PEPDS) Risk Reduction Program Review," Virginia Tech Center for Power Electronics Systems (CPES), Oct. 2023.

[5] D. Hernandez, "Thermal Analysis of Indirect Liquid Cooling for the Navy integrated Power Electronics Building Block," Bachelor's thesis, Massachusetts Institute of Technology, Cambridge, MA, 2023.

[6] N. Rajagopal, "Navy Integrated Power Electronics Building Block (Navy iPEBB)," Virginia Tech Center for Power Electronics Systems (CPES), Nov. 2020.

[7] *Soft Ferrites and Accessories Data Handbook*, Ferroxcube, 2013. [Online]. Available: https://www.ferroxcube.com/en-global/download/download/11 (visited on 05/07/2023).

[8] *Cooner Wire Catalog*, Cooner Wire. [Online]. Available: https://www.coonerwire.com/cooner_catalog_rev9-8.pdf (visited on 02/06/2024).

[9] I. A. Reyes, "Design and Modeling of the Navy Integrated Power and Energy Corridor Cooling System," Master's thesis, Massachusetts Institute of Technology, Cambridge, MA, 2022.

[10] A. Chatterjee, "Design and Modeling of Shipwide Navy Integrated Power and Energy Corridor Cooling System," Master's thesis, Massachusetts Institute of Technology, Cambridge, MA, 2023.

[11] J. G. Padilla, "Characterizing the Thermal Behavior of Pyrolytic Graphite Sheets (PGS) at Low Interface Pressures," Master's thesis, Massachusetts Institute of Technology, Cambridge, MA, 2023.

[12] K. Daware. "Cooling Methods of a Transformer," Electrical Easy. (), [Online]. Available: https://www.electricaleasy.com/2014/06/cooling-methods-of-transformer.html (visited on 02/29/2024).

[13] Q. Chen, R. Raju, D. Dong, and M. Agamy, "High Frequency Transformer Insulation in Medium Voltage SiC enabled Air-cooled Solid-State Transformers," in *2018 IEEE Energy Conversion Congress and Exposition (ECCE)*, 2018, pp. 2436–2443. DOI: 10.1109/ECCE.2018.8557849.

[14] H. Wang, Z. Guo, S. M. Tayebi, X. Zhao, Q. Huang, R. Yu, Q. Yang, Y. Li, and A. Q. Huang, "Thermal Design Consideration of Medium Voltage High Frequency Transformers," in *2020 IEEE Applied Power Electronics Conference and Exposition (APEC)*, 2020, pp. 2721–2726. DOI: 10.1109/APEC39645.2020.9124264.

[15] S. Sharfeldden, R. Raju, and C. DiMarino, "Insulation Design for a Compact, Medium-Voltage Transformer," in *2022 IEEE Energy Conversion Congress and Exposition (ECCE)*, 2022, pp. 1–6. DOI: 10.1109/ECCE50734.2022.9947979.

[16] "Litz Wire," Elektrisola Group. (), [Online]. Available: https://www.elektrisola.com/en-us/Litz-Wire/Info (visited on 02/22/2024).

[17] X. Liu, D. Gerada, Z. Xu, M. Corfield, C. Gerada, and H. Yu, "Effective Thermal Conductivity Calculation and Measurement of Litz Wire Based on the Porous Metal Materials Structure," *IEEE Transactions on Industrial Electronics*, vol. 67, no. 4, pp. 2667–2677, 2019. DOI: 10.1109/TIE.2019.2910031.

[18] X. Yi, T. Yang, J. Xiao, N. Miljkovic, W. P. King, and K. S. Haran, "Equivalent Thermal Conductivity Prediction of Form-Wound Windings with Litz Wire Including Transposition Effects," *IEEE Transactions on Industry Applications*, vol. 57, no. 2, pp. 1440–1449, 2021. DOI: 10.1109/TIA.2021.3053500.

[19] Q. Dong and X. Fu, "Prediction of Thermal Conductivity of Litz Winding by Least Square Method and GA-BP Neural Network Based on Numerical Simulations," *Energies*, vol. 16, no. 21, 2023, ISSN: 1996-1073. DOI: 10.3390/en16217295. [Online]. Available: https://www.mdpi.com/1996-1073/16/21/7295.

[20] A. A. Woodworth, A. Smith, W. Sixel, R. Edwards, R. Jansen, S. McCormick, M. Robbie, G. Szpak, P. Naghipour, and E.-S. Shin, "Thermal Analysis of Potted Litz Wire for High-Power-Density Aerospace Electric Machines," in *2019 AIAA/IEEE Electric Aircraft Technologies Symposium (EATS)*, 2019, pp. 1–13. DOI: 10.2514/6.2019-4509.

[21] "Heat Pipes 101," Advanced Cooling Technologies. (), [Online]. Available: https://www.1-act.com/thermal-solutions/passive/heat-pipes/heat-pipes-101/ (visited on 05/28/2024).

[22] K. N. Shukla, "Heat Pipe for Aerospace Applications—An Overview," in *Journal of Electronics Cooling and Thermal Control*, 2015, pp. 1–14. DOI: 10.4236/jectc.2015.51001.

[23] I. G. Hansen and M. S. Chester, "Heat Pipe Cooling of Power Processing Magnetics," in *International Conference on Electric Propulsion*, 1979. [Online]. Available: https://ntrs.nasa.gov/citations/198000030805.

[24] R. Wrobel, "Analysis of Power Loss in Heat Pipes for Integrated Thermal Management of Next Generation Electrical Machines," *Thermal Science and Engineering Progress*, vol. 47, p. 102 358, 2024, ISSN: 2451-9049. DOI: https://doi.org/10.1016/j.tsep.2023.102358. [Online]. Available: https://www.sciencedirect.com/science/article/pii/S2451904923007114.

[25] "ASTM E1225-20 Standard Test Method for Thermal Conductivity of Solids Using the Guarded Comparative-Longitudinal Heat Flow Technique," ASTM International, West Conshohocken, PA, ASTM Standard, Sep. 2020. DOI: 10.1520/1225-20.

[26] *304 Stainless Steel*, MatWeb. [Online]. Available: https://www.matweb.com/search/datasheet.aspx?MatGUID=abc4415b0f8b490387e3c922237098da (visited on 08/10/2023).

[27] *Thermal Conductivity vs Mean Temperature - Ceramic Fiber*, UniTherm. [Online]. Available: https://shop.unitherm.com/Ceramic-Fiber-Blanket-1-x24-x25-p/cf6-1-24x25.htm (visited on 05/15/2023).

[28] *Copper*, MatWeb. [Online]. Available: https://matweb.com/search/DataSheet.aspx?MatGUID=9aebe83845c04c1db5126fada6f76f7e&ckck=1 (visited on 02/24/2024).

[29] *Air - Thermal Conductivity vs. Temperature and Pressure*, Engineering Toolbox. [Online]. Available: https://www.engineeringtoolbox.com/air-properties-viscosity-conductivity-heat-capacity-d_1509.html (visited on 01/10/2024).

[30] *Plastics - Thermal Conductivity Coefficients*, Engineering Toolbox. [Online]. Available: https://www.engineeringtoolbox.com/thermal-conductivity-plastics-d_1786.html (visited on 01/16/2024).

[31] "ASTM D5470-17 Standard Test Method for Thermal Transmission Properties of Thermally Conductive Electrical Insulation Materials," ASTM International, West Conshohocken, PA, ASTM Standard, Nov. 2017. DOI: 10.1520/D5470-17.

[32] *Aluminum 6061-t6*, MatWeb. [Online]. Available: https://www.matweb.com/search/DataSheet.aspx?MatGUID=b8d536e0b9b54bd7b69e4124d8f1d20a&ckck=1 (visited on 02/24/2024).

[33] *Shapal Hi M Soft*, Precision Ceramics. [Online]. Available: https://precision-ceramics.com/materials/shapal/ (visited on 01/10/2024).

[34] *XTM50 High Performance Thermal Paste Kit*, Corsair. [Online]. Available: https://www.corsair.com/us/en/p/pc-components-accessories/ct-9010002-ww/xtm50-high-performance-thermal-paste-kit-ct-9010002-ww (visited on 05/24/2024).

[35] B. Ridder, *Propagation of Uncertainty*, version 1.3.0.0, May 24, 2024. [Online]. Available: https://www.mathworks.com/matlabcentral/fileexchange/17901-propagation-of-uncertainty.

[36] *Mica*, S and R Optic. [Online]. Available: https://www.sr-optic.com/Materials/Mica/ (visited on 02/24/2024).

[37] G. Spinelli, R. Kotsilkova, E. Ivanov, V. Georgiev, C. Naddeo, and V. Romano, "Thermal and Dielectric Properties of 3d Printed Parts Based on Polylactic Acid Filled with Carbon Nanostructures," *Macromolecular Symposia*, vol. 405, no. 1, 2022, ISSN: 1022-1360. DOI: 10.1002/masy.202100244.

[38] *Thermally Conductive Epoxy Adhesives*, MasterBond. [Online]. Available: https://www.masterbond.com/properties/thermally-conductive-epoxy-adhesives (visited on 05/24/2024).

[39] J. Stewart, J. Motwani, J. Yu, I. Cvetkovic, and R. Burgos, "Improved Power Density of a 6 kV, 1 MW Power Electronics Building Block Through Insulation Coordination," in *2022 IEEE 23rd Workshop on Control and Modeling for Power Electronics (COMPEL)*, 2022, pp. 1–7. DOI: 10.1109/COMPEL53829.2022.9829968.

[40] "Heat Pipe Design and Modeling Techniques," Advanced Cooling Technologies. (), [Online]. Available: https://www.youtube.com/watch?v=Shisfff7ulM (visited on 09/22/2023).

[41] R. Wrobel and A. Hussein, "A Feasibility Study of Additively Manufactured Heat Guides for Enhanced Heat Transfer in Electrical Machines," *IEEE Transactions on Industry Applications*, vol. 56, no. 1, pp. 205–215, 2020. DOI: 10.1109/TIA.2019.2949258.

[42] "Bending Heat Pipes, How it Affects Vapor Chambers and Heat Pipes," Celsia. (), [Online]. Available: https://celsiainc.com/heat-sink-blog/bending-heat-pipes/ (visited on 07/24/2024).

[43] J. Ordonez-Miranda, M. Hermens, I. Nikitin, *et al.*, "Measurement and Modeling of the Effective Thermal Conductivity of Sintered Silver Pastes," *International Journal of Thermal Sciences*, vol. 108, pp. 185–194, 2016, ISSN: 1290-0729. DOI: https://doi.org/10.1016/j.ijthermalsci.2016.05.014. [Online]. Available: https://www.sciencedirect.com/science/article/pii/S1290072915302805.

[44] "ACT wins $5.5m for five heat pipe projects," EE News Power Europe. (Oct. 13, 2023), [Online]. Available: https://www.eenewseurope.com/en/act-wins-5-5m-for-five-heat-pipe-projects/ (visited on 12/01/2023).

[45] B. Hughey. "Uncertainty Analysis," MIT 2.671 Measurement and Instrumentation. (Mar. 2023), [Online]. Available: https://wikis.mit.edu/confluence/display/2DOT671/Uncertainty+Analysis (visited on 10/17/2023).

[46] *PLA Filament*, Polyfluor Plastics. [Online]. Available: https://www.polyfluor.nl/assets/files/datasheet-pla-filament-uk.pdf (visited on 06/08/2024).

[47] R. Martin, E. Neary, J. Rinaldo, and O. Woodman, *Introductory Pysics: Building Models to Describe Our World*. LibreTexts, Aug. 2019. DOI: 10.24908/BPWM9859.

Appendix A

Ferrite Thermal Conductivity Experiment Uncertainty Calculations

As previously mentioned, the thermal conductivity of the test specimen can be calculated using the following equation.

$$k_s = \frac{k_m}{2}\left(\frac{T_2 - T_1}{z_2 - z_1} + \frac{T_6 - T_5}{z_6 - z_5}\right)\frac{z_4 - z_3}{T_4 - T_3} \tag{3.5}$$

It is assumed that the directly measured variables (T_i, z_i), where i represents each numbered thermocouple, are statistically independent from one another and have associated uncertainties (u_T, u_z). Propagation of uncertainty is used to determine the uncertainty for a single experimental run following the guidance outlined in [45].

$$u_{onerun} = \sqrt{\sum_{i=1}^{6}\left[\left(\frac{\partial k_s}{\partial T_i}u_T\right)^2 + \left(\frac{\partial k_s}{\partial z_i}u_z\right)^2\right]} \tag{A.1}$$

In order to account for the completion of multiple runs per sample, a final propagation of uncertainty must be performed. The resulting uncertainty is dependent on two components: u_{avg} which accounts for the averaging process and u_{indiv} which, like in A.1, accounts for the uncertainty values of each respective run.

$$u_{avg} = \frac{t_\nu * \sigma}{N} \tag{A.2}$$

$$u_{indiv} = \sqrt{\sum_{j=1}^{N}\left(\frac{1}{N}u_{onerun,j}\right)^2} \tag{A.3}$$

where N is the number of experimental runs, σ is the standard deviation of N runs, and t_ν is the t-factor corresponding to N-1 degrees of freedom. A t-factor table can be found in Table A.1. Equation A.4 gives the total uncertainty for an averaged k_s over N runs.

$$u_{tot} = \sqrt{\left(u_{avg}\right)^2 + \left(u_{indiv}\right)^2} \tag{A.4}$$

Table A.1: t-factor table for ν = 1-15 [45]

ν	t_ν
1	12.706
2	4.303
3	3.182
4	2.776
5	2.571
6	2.447
7	2.365
8	2.306
9	2.262
10	2.228
11	2.201
12	3.179
13	2.160
14	2.145
15	2.131

Appendix B

Litz Thermal Conductivity Experiment Uncertainty Code

```
%% litz runs
clear; clc

% all runs heater config: 2 @ 15V, 1 @ 14V
T_rec = [139.65 135.74 17.58 13.67; ...   % run 1, 5/22
         139.65 135.74 16.6 13.67; ...   % run 2, 5/23
         137.7 133.79 16.6 13.67; ...   % run 3, 5/24
         136.72 132.81 16.6 13.67; ...   % run 4, 5/27
         135.74 131.84 16.6 13.67];   % run 5, 5/28

[n_runs, ~] = size(T_rec);

%% code
syms ka kc kp Aa Ac Ap Aavg Dlitz Lc Lp T1 T2 T3 T4 z1 z2 z3 z4
vars = [ka kc kp Aa Ac Ap Aavg Dlitz Lc Lp T1 T2 T3 T4 z1 z2 z3
    z4];
Rc = Lc/kc/Ac;
Rp = Lp/kp/Ap;
qt = abs(ka*(T2-T1)/(z2-z1));
qb = abs(ka*(T4-T3)/(z4-z3));
qavg = 1/2*(qt+qb);
Ttop = T2-qt*Aa*(0.0762-z2)/ka/Aa;
Tbot = T3+qb*Aa*(z3-0.0762-0.0095885)/ka/Aa;
deltaTgap = Ttop-Tbot;
Rl = 4*(deltaTgap/qavg/Aa - 2*Rc - 1/2*Rp);
klitz = Dlitz/Rl/Aavg;

uncs = [0 0 0 0 0 0 0 0 0 0 2 2 2 2 0.0005 0.0005 0.0005
   0.0005];
```

```
answers = zeros(n_runs,2);

for i = 1:n_runs
    if T_rec(i,1) == 0
        break
    else
        vals = [167 92 5 0.00290322 0.00174589 0.000378709
           0.000311546 0.005588 0.002 0.0001143 T_rec(i,1)
           T_rec(i,2) T_rec(i,3) T_rec(i,4) 0.0254 0.06985
           0.0921385 0.1556385];
        [answer, uncertainty, pctUnc] = PropError(klitz,vars,
           vals,uncs);
        fprintf("Run %.0f\n",i);
        fprintf("klitz = %.2f +- %.2f W/m-K\n",[answer,
           uncertainty]);
        fprintf("percent uncertainty = %.2f \n",pctUnc);
        fprintf("\n");

        answers(i,1) = answer;
        answers(i,2) = uncertainty;
    end
end

%% PropError.m function
function [val,unc,pctUnc] = PropError(f,varlist,vals,errs)
%(c) Brad Ridder 2007. Feel free to use this under the BSD
   guidelines. If you wish to add to this program, just leave
   my name and add yours to it.
% Brad Ridder (2024). Propagation of Uncertainty (https://www.
   mathworks.com/matlabcentral/fileexchange/17901-propagation-
   of-uncertainty), MATLAB Central File Exchange. Retrieved May
    24, 2024.
n = numel(varlist);
sig = vpa(ones(1,n));
for i = 1:n
    sig(i) = diff(f,varlist(i),1);
end
error1 =sqrt((sum((subs(sig,varlist,vals).^2).*(errs.^2))));
error = double(error1);
val = double(subs(f,varlist,vals));
unc = error;
pctUnc = unc/val*100;
```

Appendix C

Heat Pipe Initial Sizing Calculations

In order to get a first order estimate of the heat loads each heat pipe would have to transport, a rough concept shown in Figure C.1 is used. In this cross-section view, two heat pipes are shown attached to aluminum rectangular heat spreaders mounted to either side of one core leg. This concept assumes that each heat pipe will be mirrored in the direction into the page, giving a total of four per core leg, or 8 per core half. Red arrows show the rough direction of heat flow in this setup.

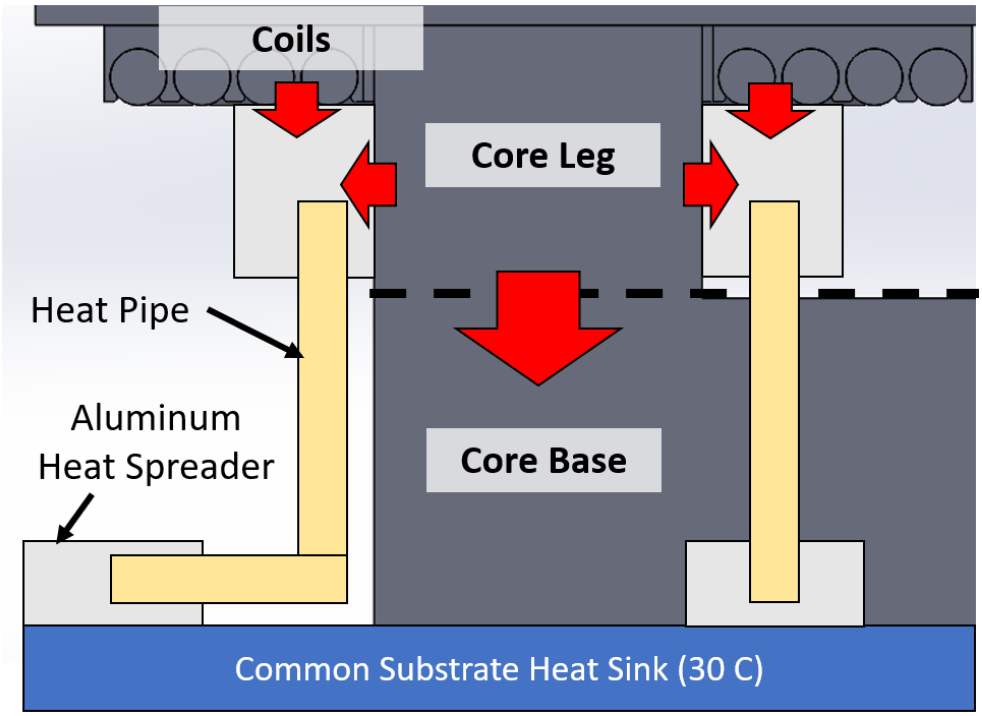

Figure C.1: Simplified heat flow diagram for heat pipe concept.

First, we will assume uniform distribution of the worst-case core losses in Table 5.2, giving each core leg losses of $Q_{core\ leg} = 37.5$ W. Each of the four winding assemblies dissipates $Q_{winding} = 36$ W. To simplify the calculations, first we will omit the winding losses and estimate the thermal resistance network for heat generated in the core leg, with the leg

being modeled as a lumped node. Taking into account the path through the core base in addition to the heat pipe-aluminum block alternative results in the effective resistance network shown in Figure C.2.

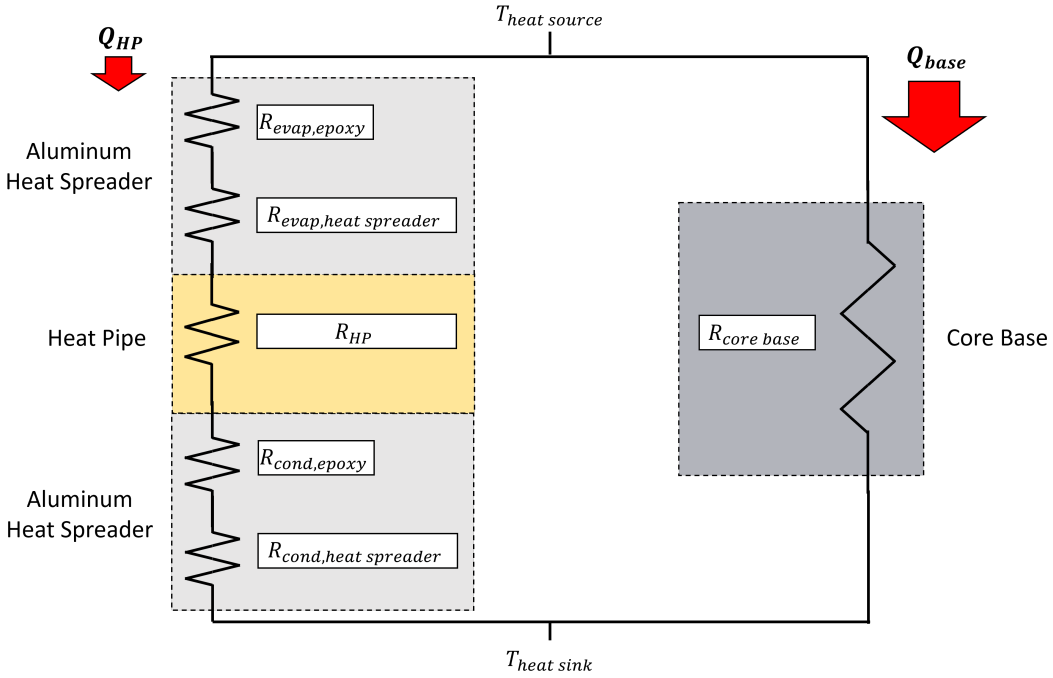

Figure C.2: Simplified thermal resistance network for heat generated in the core leg.

The math for the heat pipe follows the analytical model outlined by Advanced Cooling Technologies (ACT), and visualized in Figure C.3 [40]. First the area-independent thermal resistance of the outer copper casing, solder interface, and wick material can be estimated using typical values provided from the distributor. These components are then consolidated into one effective thermal resistance representing a unit area of the heat pipe support envelope. Assuming an effective envelope thickness of 0.04 in. (1.02 mm) results in the envelope thermal conductivity given by Equation C.4.

$$R_{solder}A = \frac{L_{solder}}{k_{solder}} = \frac{1.02 * 10^{-4}\ m}{19\ W/mK} = 5.35 * 10^{-6}\ Km^2/W \tag{C.1}$$

$$R_{copper}A = \frac{L_{copper}}{k_{copper}} = \frac{3.05 * 10^{-4}\ m}{380\ W/mK} = 8.02 * 10^{-7}\ Km^2/W \tag{C.2}$$

$$R_{wick,evap,cond}A = 3.20 * 10^{-5}\ Km^2/W \tag{C.3}$$

$$k_{eff,env} = \frac{L_{eff}}{R_{solder}A + R_{copper}A + R_{wick,evap,cond}A} = \frac{1.02\ mm}{3.81 * 10^{-5}\ Km^2/W} = 26.7\ W/mK \tag{C.4}$$

Based off the transformer core's geometry, a 100 mm total heat pipe length was chosen, with 20 mm of each end being embedded in the heat spreaders on either end. Using these

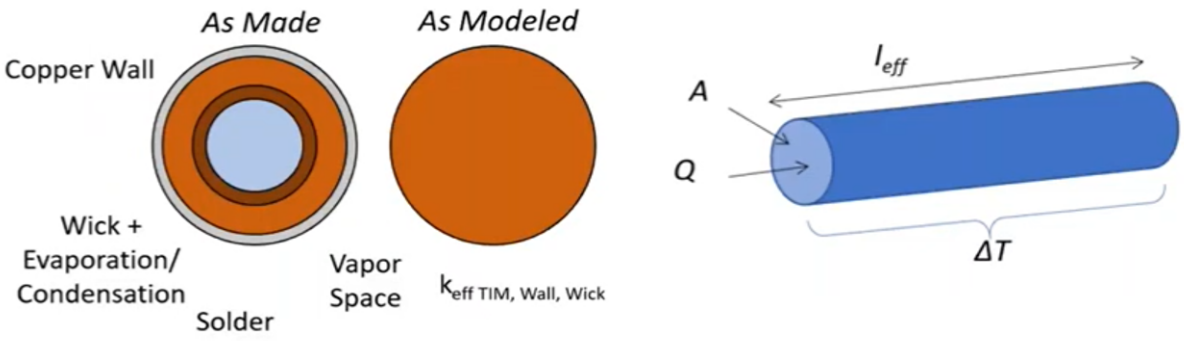

Figure C.3: Visualization of ACT analytical heat pipe thermal model with the support envelope (left) and vapor region (right) shown with key dimensions noted [40].

lengths with our modeled effective envelope thickness and thermal conductivity, we find a thermal resistance from the outer heat pipe surface to the inner surface of $R_{eff,env} = 0.48$ W/mK.

To model the heat pipe vapor region, we use the expected effective heat pipe length $l_{eff} = l_{total} - \frac{l_{evap}+l_{cond}}{2} = 80$ mm. A temperature difference of ΔT = 5°C is assumed along the length of the heat pipe as a conservative capturing of the nearly isothermal behavior they typically produce. An equation provided by ACT for the heat pipe vapor region is given by Equation C.5; however, the dependence on the amount of heat flow $Q_{expected}$ makes this an implicit expression that will require iteration to solve. An arbitrary value was initially set. Once solved, the thermal resistance of the vapor region modeled as a cylindrical tube is given by $R_{eff,vapor} = \frac{l_{eff}}{k_{eff,vapor}A}$.

$$k_{eff,vapor} = \frac{Q_{expected}L_{eff,HP}}{A\Delta T} \tag{C.5}$$

Combined, the heat pipe can now be modeled using the envelope and vapor components in series.

$$R_{HP} = 2R_{eff,env} + R_{eff,vapor} \tag{C.6}$$

For each aluminum heat spreader, rough estimates can be made for the cross-sectional area and thickness of the material between the heat pipe and the heat source/sink. Using a basic rectangular slab shape results in the following expressions for thermal resistance. We also account for a layer of thermal epoxy at these heat spreader interfaces.

$$R_{evap,heat\ spreader} = R_{cond,heat\ spreader} = \frac{L_{heat\ spreader}}{k_{al}A} = \frac{2\ mm}{(167\ W/mK)(160\ mm^2)} = 0.07\ K/W \tag{C.7}$$

$$R_{evap,epoxy} = R_{cond,epoxy} = \frac{L_{bondline}}{k_{ep}A} = \frac{1.5 * 10^{-5}\ m}{(2.1\ W/mK)(160\ mm^2)} = 0.045\ K/W \tag{C.8}$$

Heat flow through the core is estimated as conduction through the core base with ferrite modeled conservatively with a thermal conductivity $k_{ferrite} = 3.5$ W/mK.

$$R_{core\ base} = \frac{L_{core\ base}}{k_{ferrite} A} = \frac{30\ mm}{(3.5\ W/mK)(1950\ mm^2)} = 4.40\ K/W \tag{C.9}$$

With the thermal network set up, we can solve for the heat flow through each heat pipe and iterate back through Equation C.4. This results in a core-loss-only heat flow of 8.51 W per heat pipe when accounting for the 4 in parallel on each core leg. Assuming the 37.5 W of heat losses from an individual winding are evenly distributed between the four heat pipes, we arrive at an updated estimate of 17.9 W. Finally, we add a 40% safety factor as well as a 5% margin for each of the two expected 90° bends, for a total buffer of 50%. This leaves us with the final estimate for heat through the heat pipe Q_{HP}.

$$Q_{HP} = 26.8\ W \tag{C.10}$$

Plugging in our chosen heat pipe parameters to an online calculator provided by ACT, whose results are shown in Figure C.4, shows that a 5 mm diameter HP can comfortably withstand the expected loads at the estimated heat pipe operating temperature. This size diameter also provides margin for future design iterations that may increase heat flow.

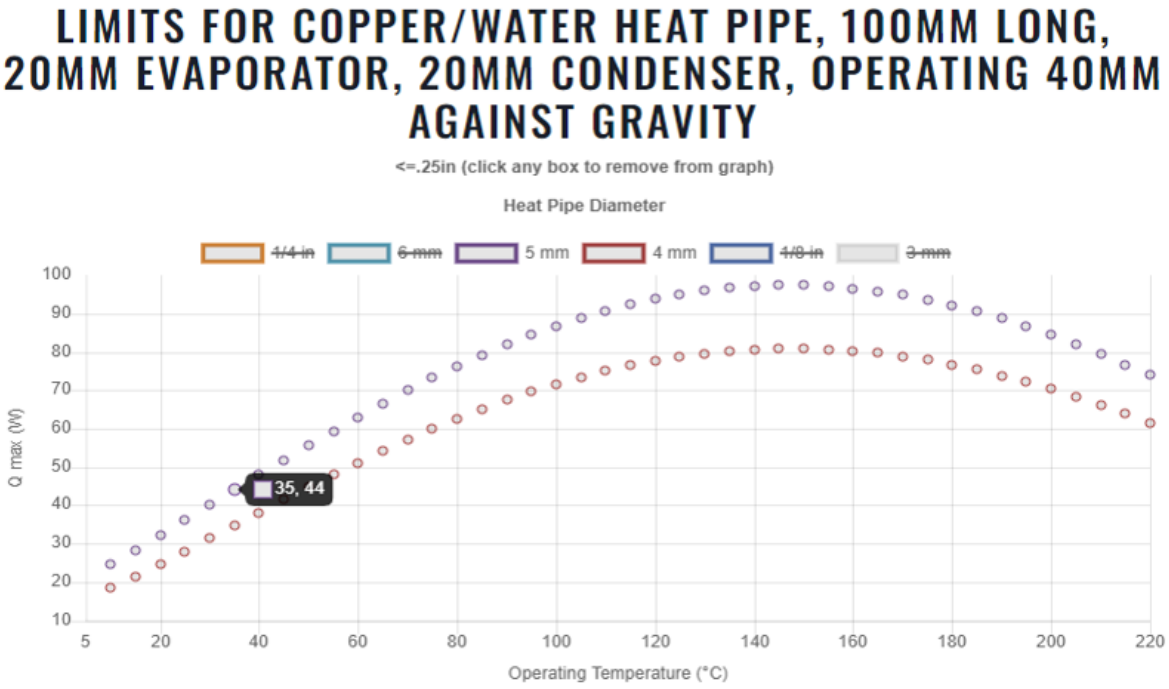

Figure C.4: Maximum heat load capacity for a 100mm-long copper-water heat pipe with the expected dimensions of the iPEBB transformer configurations [21].

Appendix D

Transformer Cooling Solutions Weight Breakdown

Table D.1: Weight Breakdown for Heat Pipe Iteration 1

Component	Total Volume (cm^3)	Density (g/cm^3)	Total Weight (kg)	(lb)
Aluminum Heat Spreaders	82.64	2.7 [32]	0.22	0.49
AlN Ceramic Insulation	143.62	2.88 [33]	0.41	0.91
PLA Wireholder	41.80	1.25 [46]	0.05	0.12
Heat Pipes*	n/a	n/a	0.06	0.14
Total Added Weight			0.75	1.66

*Scaled from known value for a 200 mm long variant

Table D.2: Weight Breakdown for Heat Pipe Iteration 2

Component	Total Volume (cm^3)	Density (g/cm^3)	Total Weight (kg)	(lb)
AlN Ceramic Heat Spreaders	56.08	2.88 [33]	0.16	0.36
Aluminum Heat Spreaders	18.56	2.7 [32]	0.05	0.11
AlN Ceramic Insulation	143.62	2.88 [33]	0.41	0.91
PLA Wireholder	41.80	1.25 [46]	0.05	0.12
Heat Pipes*	n/a	n/a	0.06	0.14
Total Added Weight			0.74	1.63

*Scaled from known value for a 200 mm long variant

Table D.3: Weight Breakdown for Heat Pipe Iteration 3

Component	Total Volume (cm^3)	Density (g/cm^3)	Total Weight (kg)	(lb)
AlN Ceramic Heat Spreaders	75.76	2.88 [33]	0.22	0.48
Aluminum Heat Spreaders	15.84	2.7 [32]	0.04	0.09
AlN Ceramic Insulation	143.62	2.88 [33]	0.41	0.91
PLA Wireholder	41.80	1.25 [46]	0.05	0.12
Heat Pipes*	n/a	n/a	0.05	0.11
Total Added Weight			0.77	1.71

*Scaled from known value for a 200 mm long variant

Table D.4: Weight Breakdown for the Final Heat Pipe Solution, Including Changes to iPEBB Common Substrate

Component	Total Volume (cm^3)	Density (g/cm^3)	Total Weight (kg)	(lb)
AlN Ceramic Heat Spreaders	56.24	2.88 [33]	0.16	0.36
Aluminum Heat Spreaders	17.2	2.7 [32]	0.05	0.10
AlN Ceramic Insulation	143.62	2.88 [33]	0.41	0.91
PLA Wireholder	41.80	1.25 [46]	0.05	0.12
Heat Pipes*	n/a	n/a	0.06	0.12
Common Substrate Copper Removed	49.54	8.96 [28]	0.44	0.98
Added Weight			0.73	1.61
Removed Weight			0.44	0.98
Net Weight Gain			0.29	0.63

*Scaled from known value for a 200 mm long variant

Appendix E

Final Heat Pipe Design Capacities

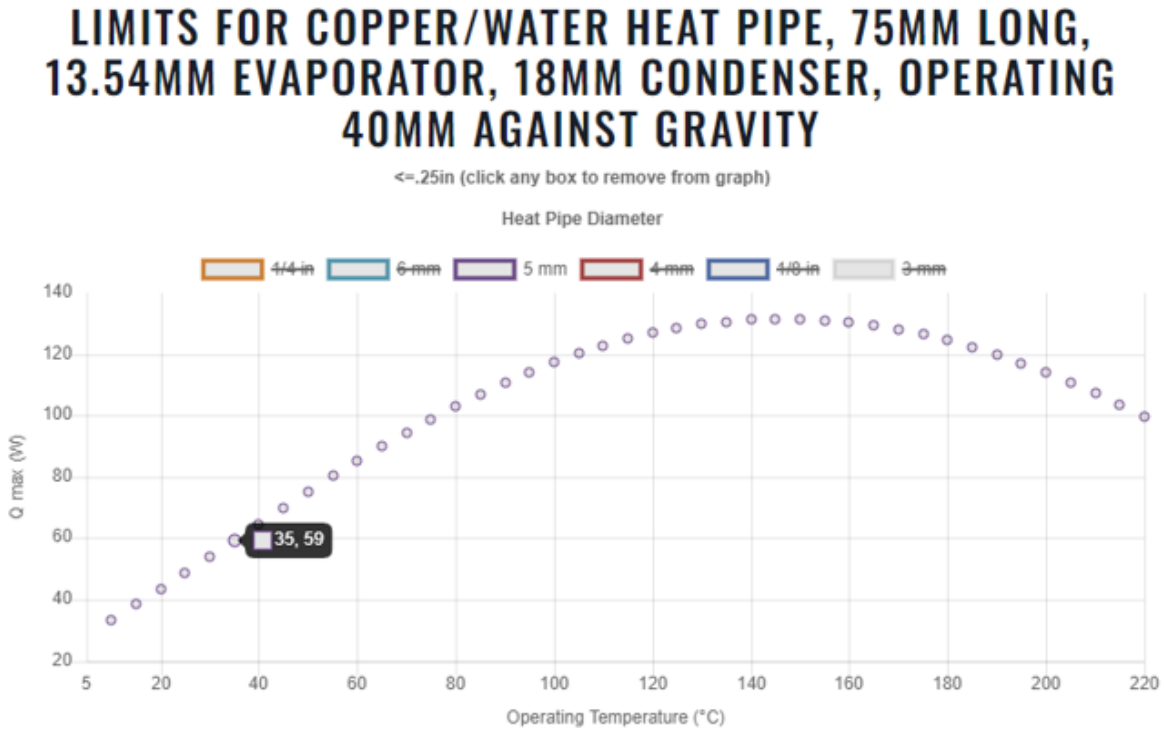

Figure E.1: Heat capacity limits for the 75mm long, 1-bend L-shaped heat pipe selected for the iPEBB transformer. Results at the expected temperature range highlighted [21].

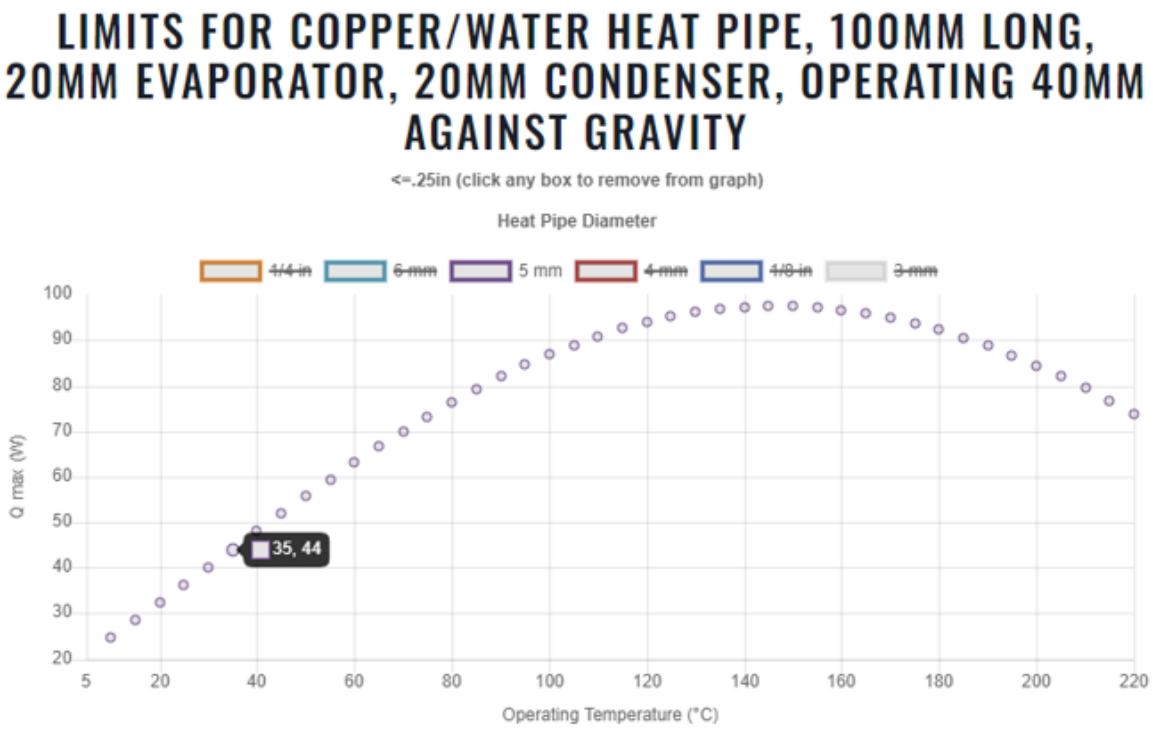

Figure E.2: Heat capacity limits for the 100mm long, 2-bend S-shaped heat pipe selected for the iPEBB transformer. Results at the expected temperature range highlighted [21].

Appendix F

Electromagnetic Simulation Validation

In order to validate the accuracy of the excitation coil modeling in StarCCM+, a test case using two symmetric Helmholtz coils was created. Two coils of radius $R = 300$ mm were placed parallel from each other at a distance R. A constant current of $I = 0.1$ A was ran through both bodies, which sit in a large region of air. The analytical solution of this setup is known, and given by Equation F.1 [47].

$$B^{total}(x) = \frac{\mu_0 I}{2} \frac{R^2}{(R^2 + (x + R/2)^2)^{3/2}} + \frac{\mu_0 I}{2} \frac{R^2}{(R^2 + (x - R/2)^2)^{3/2}} \tag{F.1}$$

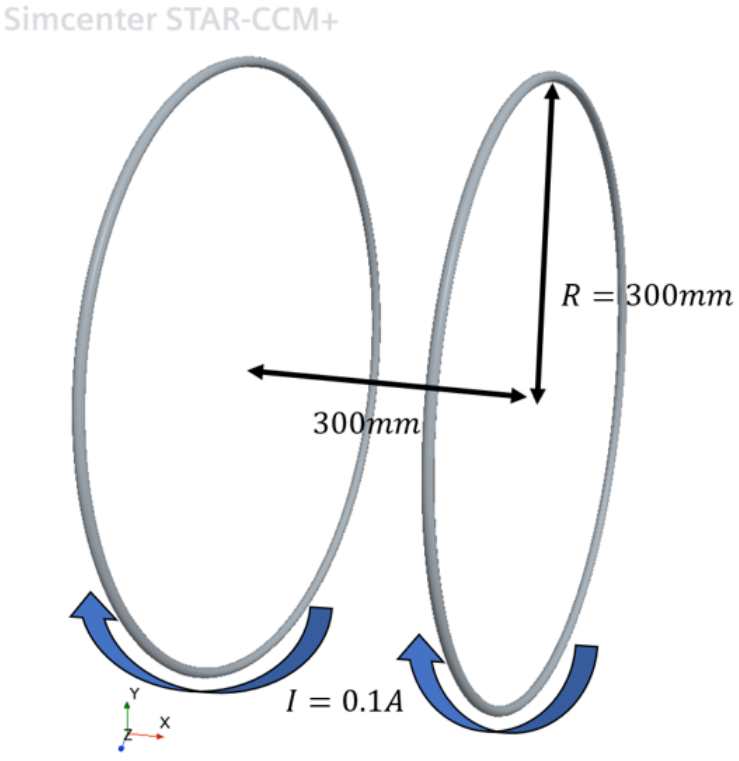

Figure F.1: Dual Helmholtz coil model setup.

Results from the simulation run were in agreement with the analytical curve, confirming the accuracy of the modeling approach.

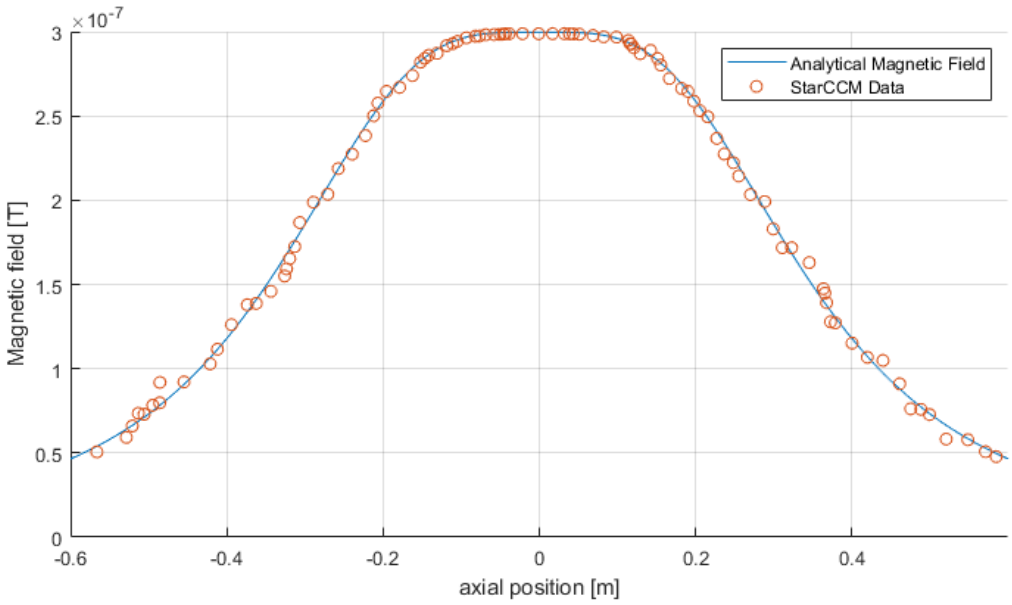

Figure F.2: Analytical vs simulated magnetic field along the axis of symmetry for the dual Helmholtz coil model.

When modeling the heat pipes, the geometry was modified to make the heat pipe thickness equal to the skin thickness of copper at each coil frequency tested. Adjusting the copper-wall thickness better captures the behavior of copper at these frequencies, with the lower skin penetration of magnetic fields at high frequencies resulting in the localization of electric current and heat generation in the skin depth region. However, the memory requirements of the model when meshing these thin surfaces exceeded available hardware capabilities. As a result, a mesh study was conducted to compare mesh discretization error in the heat pipe model.

First, a model for 50 kHz coil operations was run, with a heat pipe thickness given by the skin depth of 0.292 mm. Meshes using 1 and 2 layers of cells along the heat pipe thickness were run. The memory requirements of a 3 layer model exceeded resources, and as a result additional mesh layers were not tested. Results showed that reducing the number of mesh layers from 2 to 1 only resulted in a heat generation difference of 2.3%, while reducing the cell count by 46%.

Table F.1: Heat Pipe (HP) Mesh Comparison for Coil Frequency of 50 kHz

		HP Losses (W)	
HP Mesh Layers	Cell Count	Quarter Transformer	Full Transformer
1	7,437,249	2.67	10.68
2	13,820,545	2.61	10.44

To test the affect of higher mesh numbers, a model was created and simulated for 20 kHz

coil operations, with a heat pipe thickness given by the skin depth of 0.461 mm. Meshes using 2 and 3 layers of cells along the heat pipe thickness were ran. Results were similar to those for the 50 kHz model and showed a heat generation difference of 3.6% while reducing the cell count by 47%.

Table F.2: Heat Pipe (HP) Mesh Comparison for Coil Frequency of 20 kHz

		HP Losses (W)	
HP Mesh Layers	Cell Count	Quarter Transformer	Full Transformer
2	7,444,628	1.66	6.64
3	14,129,181	1.60	6.40

Due to the small difference in results, it was decided that the discretization error of the lower fidelity mesh was acceptable. The large reduction in mesh size allows for the running of models at higher frequencies above 100 kHz, which failed to run when attempting to model more than 1 mesh layer. Furthermore, the decrease in heat generation seen with increasing mesh layers implies that modeling only 1 mesh layer overestimates heat pipe losses, adding to the conservative setup of the thermal model.